ELECTROCONVECTION OF TWO-DIMENSIONAL LIQUID CRYSTAL FILMS

SAMUEL S. MAO

ELECTROCONVECTION IN TWO-DIMENSIONAL LIQUID CRYSTAL FILMS

SAMUEL S. MAO

A THESIS SUBMITTED IN PARTIAL
FULFILLMENT OF THE REQUIREMENTS
FOR
THE DEGREE OF
MASTER OF SCIENCE

DEPARTMENT OF PHYSICS AND PHYSICAL OCEANOGRAPHY
MEMORIAL UNIVERSITY OF NEWFOUNDLAND
MAY 1996

ST. JOHN'S CANADA

Abstract

We have studied electrically driven convection in freely suspended films of smectic A liquid crystal. The layered molecular structure of the smectic A mesophase makes the film behave like a two-dimensional isotropic fluid, and well-controlled hydrodynamic flow has been achieved in films as thin as two molecular layers in thickness. When a d.c. voltage applied across the film exceeds a certain critical value V_c, a one-dimensional pattern of convective vortices develops. The critical pattern wavelength appears to be independent of film thickness, and the critical voltage is linear in film thickness for thin films. Measurements of the pattern amplitude indicate a supercritical bifurcation at convection onset, and the amplitude grows as a 1/2-power law with respect to the normalized control parameter ε. The correlation length of the pattern varies as $\varepsilon^{-1/2}$, and the pattern's relaxation time varies as ε^{-1}. These results are in agreement with predictions from a Ginzburg-Landau amplitude equation. Measurements of the flow velocity show that the amplitude of the pattern is suppressed at the lateral boundaries. The range of wave numbers for stable convection has been obtained experimentally. Close to onset we find the width of the stable band is proportional to ε, consistent with predictions of the theory of boundary-induced wavelength selection. In addition to convection experiments, a set of electrohydrodynamic equations is presented for understanding the two-dimensional electroconvection. Theoretical analysis indicates the normalized control parameter to be $V^2/V_c^2 - 1$, in agreement with the experimental observations. A hydrodynamic model is also proposed to describe the flow observed near the sidewalls below the onset of convection. The flow in this model is caused by the electrohydrodynamic shear-stress interaction which originates from an interfacial charge density distribution at the lateral boundary.

Acknowledgements

It is a great pleasure to express my sincere appreciation to my supervisor, Dr. John R. de Bruyn, for his valuable advice and generous assistance at all stages of this work. I am indebted to our collaborator, Dr. Stephen W. Morris, for many stimulating discussions, both in his basement laboratory in Toronto and on the beach in California. A visit to Dr. Guenter Ahlers' lab at Santa Barbara, Dr. Mory Gharib and Dr. Alex Weigand's lab at Pasadena broadened my perspectives. I have also enjoyed and benefitted from fruitful discussions with Dr. Agnes Buka, Dr. Frank Feng, Dr. Jun Liu, Dr. Qi Ouyang, Dr. Werner Pesch, Dr. Eric Weeks, Dr. Wenbin Zhang, and many others. Last but certainly not least, I would like to extend my gratitude to Professor Shanzhe Ke and Professor Ali B. Cambel, for their enthusiasm and encouragement throughout my research.

Contents

Acknowledgements i

Table of Contents ii

1 Introduction 1

1.1 Patterns out of Equilibrium 2

1.2 The Liquid Crystal Phases 5

1.3 Rayleigh-Bénard Convection 9

1.4 The Ginzburg-Landau Model 13

1.4.1 The Amplitude Equation 13

1.4.2 Relaxation Time and Correlation Length 14

1.4.3 The Range of Stability 15

1.5 Electroconvective Instability 18

2 Theory 22

2.1 Hydrodynamic Equations for Isotropic Fluids in a Nonuniform Electric Field 23

2.2 Mechanism of Two-Dimensional Electroconvection 26

2.3 The Dimensionless Control Parameter 31

3 Experiments 34

3.1 Experimental Setup 35

3.2 Film Thickness Determination 40

3.2.1 Measuring Reflected Intensity 40

3.2.2 Measuring Reflected Colours 43
3.3 Flow Visualization 48

4 Experimental Results **50**
4.1 Onset of Convection 51
4.1.1 The Onset Voltage 51
4.1.2 The Onset Wavelength 54
4.1.3 The Amplitude close to Onset 55
4.2 Convection above Onset 62
4.2.1 Measurements of Convection Wavelength 62
4.2.2 Measurements of Convection Amplitude 65
4.2.3 Evolution Towards a Stable State 69
4.3 Selection of Pattern Wavelength 72
4.3.1 Experiments with Varying ε 72
4.3.2 Experiments with Varying Γ 77
4.4 Discussions 82
4.4.1 Critical Behaviour 82
4.4.2 Wavelength Selection 83

5 Conclusion **87**
5.1 Conclusion 88
5.2 Future Work 91

A Boundary Vortex Problem **96**
A.1 The Electrohydrodynamic Shear-Stress Interaction 97
A.2 Solution of the Boundary Vortex Model 103

B Measuring Colour **109**
B.1 Colorimetry 110
B.2 Computer Program for Colorimetry 116

Bibliography **122**

Chapter 1

Introduction

"Virtually every structure in the natural world is the result of a long sequence of successive symmetry breaking instabilities due to nonlinear processes under nonequilibrium conditions." — Nicolis and Prigogine [142]

1.1 Patterns out of Equilibrium

Nature displays order in many different contexts — snow flakes, cloud streets, sand ripples, and the morphology of plants and animals are examples. In well-controlled laboratory experiments, regular ordered structures have been produced in a variety of nonequilibrium systems, such as convecting gases [26, 132], flowing films [21, 93, 120, 198], chemical reactors [74, 145, 146, 166, 214], magnetic colloids [190, 200, 205, 206], and solid-liquid [76, 92, 96, 103, 192], nematic-isotropic [16, 36, 177] or nematic-smectic interfaces [35]. Even bacterial colonies [18, 19, 33, 34] can exhibit fascinating self-organized patterns.

Patterns are ordered structures which appear beautiful, but also mysterious. Understanding the origin of spatio-temporal patterns, as well as the mechanisms by which they evolve, has been a major theme of the active field of *nonlinear science* [111]. Pattern-forming phenomena are of interest in many fields, ranging from physics, chemistry to material sciences and biology, and the study of pattern formation is particularly interdisciplinary [210] which may stimulate the growth of new ideas and therefore potential new technologies.

It is a common scenario that a new organized pattern arises in a complex system in response to some external stress. Under the influence of the external stress, such a system may undergo a series of *symmetry-breaking bifurcations* [53, 85], analogous to phase transitions in an equilibrium thermodynamic system [81]. For small stress, the system remains in a homogeneous state that may be described simply in terms of a dissipative flux or gradient. As the stress exceeds a certain critical value, the system bifurcates towards a new stable state in which some of the original symmetries are broken. Usually, such a symmetry-breaking bifurcation, loosely called a pattern-forming instability, gives rise to new length scales not existing in the original symmetric phase and leads to spatial or spatial-temporal patterns, called *dissipative structures* [141]. At a high level of stress, after repeated bifurcations, the

system will exhibit complicated behavior which is often described in terms of *chaos* [24, 41, 67, 167] or *turbulence* [130, 179, 184].

Although patterns arise in systems governed by very different microscopic laws, similarities among patterns in diverse systems suggest that a theory of pattern formation should be general. The intense interest in pattern formation outside equilibrium has been inspired by the development of theories that tend to simplify and unify problems seemingly unrelated at the microscopic level. While the appropriate microscopic equations of motion for most pattern forming systems are either not known or too complicated to analyze, phenomenological order parameter models [138], such as the Ginzburg-Landau model [199], the Swift-Hohenberg model [153, 188], the reaction-diffusion model [75, 135], and the Kuramoto-Sivashinsky model [112, 180], yield simple *amplitude equations* which accurately describe the large scale modulation of weakly nonlinear patterns. In analogy to the theory of thermodynamic phase transitions [156], the degree to which patterns are described by amplitude equations of universal form reflects a degree of *universality* in pattern-forming phenomena [56]. Although it is not clear yet how far this concept can be extended, a universal theory of pattern formation outside equilibrium has been one of the goals of nonlinear science.

A large part of the progress in understanding nonequilibrium pattern formation has resulted from detailed studies of *Rayleigh-Bénard convection* [23, 143], in which a layer of fluid is heated from below. Once a critical thermal gradient or temperature difference across the layer is exceeded, a regular pattern of convective rolls develops. Interesting variants of Rayleigh-Bénard convection involve thermal convection in binary fluids [61, 94], thermal convection and electroconvection in nematic liquid crystals [64, 109], electroconvection in dielectric fluids [113], as well as surface tension driven convection [104, 105, 169], magnetically driven convection [30, 157], and convection in porous media [90, 174].

The subject of this thesis is electrically driven convection in a freely suspended film of smectic A liquid crystal. The layered structure of the smectic phase makes the film behave like a two-dimensional isotropic liquid, so the film is particularly suitable for the study of two-dimensional hydrodynamics. In most other systems, it is experimentally difficult to isolate the primary two-dimensional flow from flow in the third dimension, although efforts have been made such as by introducing rotation [89], a magnetic field [182], or by using freely suspended nematic films [71, 72]. Hydrodynamic experiments employing soap films [52, 78, 102, 207] have also been carried out more recently.

Our objective is to explore the *one-dimensional* pattern-forming phenomena exhibited in a highly *two-dimensional* convective system. In particular, we will focus on the behaviour of the system at and near the bifurcation to convection.

In the remainder of this chapter, we introduce liquid crystal materials with a focus on the smectic phases. Then, convection in the Rayleigh-Bénard system is discussed, followed by an introduction to the Ginzburg-Landau amplitude equation. The last section of this chapter provides a description of the general features of different types of electrically driven convective instability.

1.2 The Liquid Crystal Phases

Many organic molecules form mesophases called *liquid crystals* [49, 59, 155], which combine the properties of crystalline solids and isotropic liquids. They were discovered about one century ago and have found many technological applications [11], such as the widely-used liquid crystal displays and sensors. Liquid crystal molecules are geometrically anisotropic. The material used in our experiments is composed of highly anisotropic rod-like molecules, which can form nematic and smectic liquid crystal phases.

Nematic liquid crystals (Figure 1.1) are characterized by long range orientational order of the molecules, but translational order is absent. They differ from isotropic liquids in that the molecules tend to align parallel to each other. They are optically uniaxial and strongly birefringent.

Smectic liquid crystals are layered systems with a well-defined interlayer spacing and as such have partial (one-dimensional) translational order. There exist a variety of smectic phases characterized by different molecular arrangements within the smectic layers, the two simplest of which are smectic A and smectic C phases. In a smectic A phase molecules within each layer are oriented normal to the layer plane, but have no positional order (Figure 1.1). The thickness of the smectic layers is on the order of a molecular length. Like the nematics, smectic A liquid crystals are optically uniaxial with the axis perpendicular to the layers. Smectic C can be regarded as a tilted form of smectic A, that is, the long axis of the molecules points at an angle to the smectic layer normal (Figure 1.1). As a result, smectic C liquid crystals are optically biaxial. The layers in smectic A and smectic C mesophases are flexible and readily distorted, but only deformations that tend to preserve the interlayer spacing are possible [150].

The direction of preferred orientation of the liquid crystal molecules is characterized by the *director*, a "semi-vector" $\mathbf{n}$ satisfying $\mathbf{n} = -\mathbf{n}$. For both

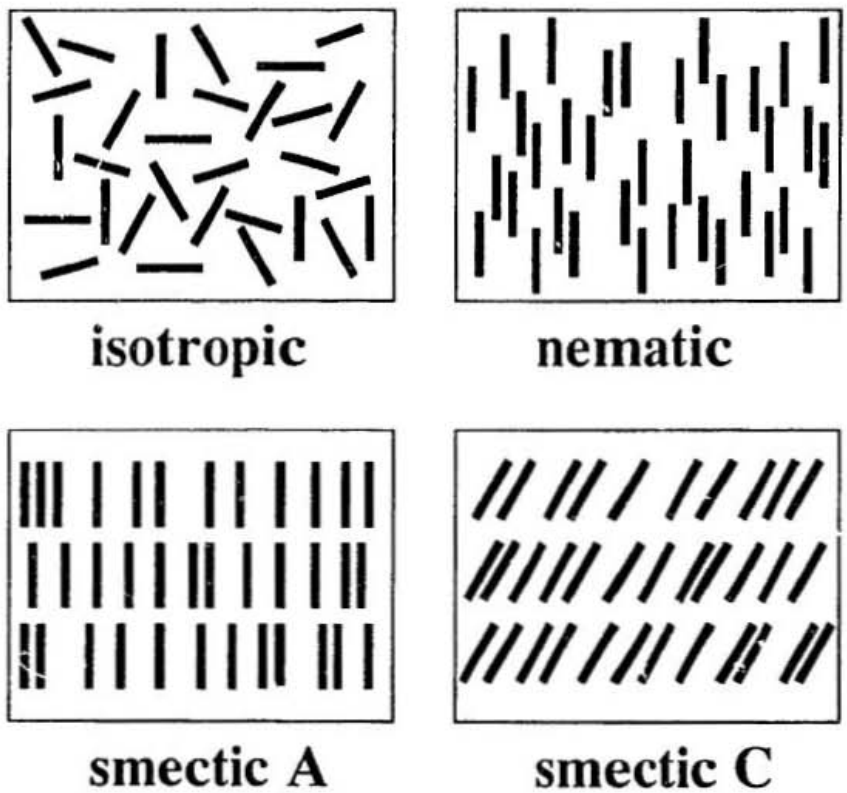

Figure 1.1: Schematic illustration of molecular order in the isotropic, nematic, smectic A and smectic C phases.

the nematic and smectic A phases, the director coincides with the direction of the optical axis, which is normal to the layer plane in the smectic A case. However, for smectic C liquid crystals, the director is inclined to the molecular layers.

For thermotropic liquid crystal materials that pass through more than one mesophase between the solid and isotropic liquid phases, the sequence of phases with increasing temperature is typically: solid → smectic C → smectic A → nematic → isotropic liquid. This sequence is consistent with the general observation that increasing temperature results in a progressive loss of molecular order.

The anisotropic nature of the molecular structure of liquid crystals results in anisotropy of the dielectric permittivity ϵ, electric conductivity σ, optical refractivity n, as well as the viscoelastic and other physical properties. Under the influence of an applied electric or magnetic field, various processes, including electrohydrodynamic instabilities [49, 59, 107], may take place in which a change in the orientation of the molecules is involved. The anisotropy of the electrical properties of liquid crystals is the origin of such reorientation, whereas the dynamics of the processes also depends on the viscoelastic properties of the material [68, 118].

In the smectic A liquid crystal used in our experiments, molecules can move freely in the plane of the smectic layers [32, 84]. Each molecular layer behaves as a two-dimensional isotropic liquid while, in the direction normal to the layers, flow is generally difficult. At temperatures close to the smectic A – nematic phase transition, permeation effects may cause flow perpendicular to the smectic layers [25, 117, 158]. However, this type of flow is completely negligible in the temperature range of our experiments.

Smectic liquid crystals can easily form freely suspended films spanning a solid frame [151, 212], similar to soap films [136, 170]. The molecular layers

in a freely suspended film are oriented parallel to the surface of the film by surface tension, and a change in the number of molecular layers is necessarily discontinuous [32, 150]. Discovered at the beginning of the 20th century [77], freely suspended smectic films received renewed interest in the 1970s, when the technique of preparing the films was developed by the liquid crystal group at Harvard [212]. Since then, numerous theoretical and experimental investigations have been performed [12, 13, 50, 79, 91, 101, 110, 151, 152, 165, 178, 183, 185, 186] in order to understand the extraordinary structures of smectic liquid crystals as well as the underlying physics in reduced dimensionality.

In our experiments, freely suspended films have been made with thickness as small as two molecular layers. Observed under a beam of reflected white light, such a two-layer film resembles a so-called *Newton black film* [140], which have been made by various surfactants [17, 70, 86] spanned on a frame [31, 151]. A smectic film in our experiments is subjected to an electric field in the plane of the film. The resulting electrohydrodynamic instability, which will be discussed later, gives rise to a *one-dimensional* pattern of *two-dimensional* vortices. In our experiments, hydrodynamic flow has been observed in a system so closely two-dimensional that the third dimension contains only two molecular layers. Our observations in extremely thin, uniform films do not indicate any change in thickness under the influence of the applied field or the convective flow, even when the flow proceeds to the unsteady regime. In addition, the reorientation of the liquid crystal molecules are not observed to accompany the convective flow when the film is viewed between crossed polarizers, and this is in agreement with the report of Morris et al. [133]

1.3 Rayleigh-Bénard Convection

The Rayleigh-Bénard system is probably the simplest example of an isotropic pattern forming system that is accessible to both experimental and theoretical investigations. The primary experimental results on convective motion were established by Bénard around the turn of this century [20]. In an attempt to interpret his observations, Lord Rayleigh performed the first theoretical analysis of the origin of the convective motion in 1916 [163]. Although it is now known that Rayleigh's analysis does not actually apply to Bénard's original system — in which surface tension effects were dominant — their work has stimulated the long lasting interest in what is now called Rayleigh-Bénard convection.

The classical Rayleigh-Bénard system consists of a thin horizontal fluid layer heated from below [4]. The fluid layer is confined between two infinite rigid parallel plates separated by a distance d, as shown in Figure 1.2. Due to the effect of thermal expansion, the fluid near the bottom plate is less dense than that near the top. This unstable vertical density profile drives the sustained convective motion.

The dependence of the convective motion on material properties and experimental conditions can be characterized by two dimensionless numbers [39]: the Rayleigh number Ra, which is proportional to the temperature difference ΔT between the top and bottom plates, and the Prandtl number Pr, which gives the relative importance of thermal and viscous diffusion:

$$Ra = \frac{\alpha g d^3 \Delta T}{\kappa \nu}, \tag{1.1}$$

$$Pr = \frac{\nu}{\kappa}. \tag{1.2}$$

Here α, κ, and ν denote the coefficient of thermal expansion, the thermal diffusivity, and the kinematic viscosity of the fluid respectively, and g is the acceleration due to gravity.

Due to the influence of viscosity, which always acts to oppose the motion of the fluid, and to the influence of heat diffusion, which tends to dissipate the temperature gradient that drives the flow, the onset of convection does not take place at an arbitrarily small value of Ra (or of ΔT). The motionless steady state, in which heat is transported across the vertical fluid layer by conduction, remains stable until the Rayleigh number reaches a certain critical value Ra_c, at which the buoyancy of the fluid is able to overcome the dissipative effects of viscosity and thermal diffusion. At this point convective flow sets in in the form of a periodic pattern of vortices characterized by a specific wavelength λ_c or wave number k_c, as illustrated in Figure 1.2.

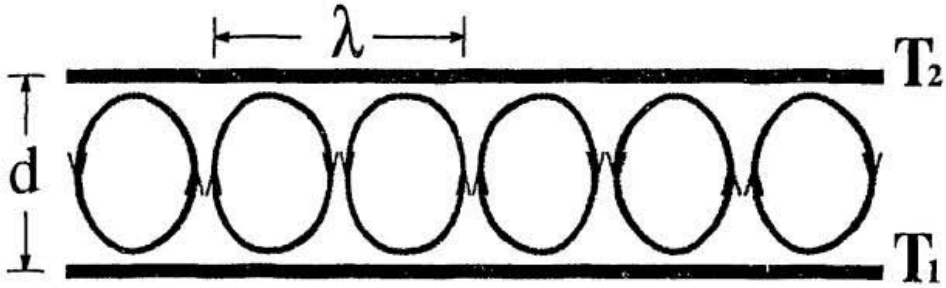

Figure 1.2: Rayleigh-Bénard convection. A temperature difference ($T_1 > T_2$) is maintained between the top and bottom plates.

For Rayleigh numbers greater than Ra_c, the convective state exists over a continuous band of wave numbers. This band is determined by the marginal stability curve shown in Figure 1.3, below which the motionless steady state is stable against fluctuations. The marginal curve can be obtained from a linear stability analysis of the microscopic equations, first performed by Rayleigh and discussed in detail by Chandrasekhar [48].

These one-dimensional periodic states do not remain stable over the entire

range of wave numbers bounded by the marginal curve. Based on very general stability considerations, Eckhaus [66] showed that the possible range of wave numbers for stable convective motion is restricted to a narrower band (Figure 1.3),

$$k_E - k_c = \frac{1}{\sqrt{3}}(k_m - k_c). \tag{1.3}$$

where k_c denotes the critical wave number of the linear theory, and k_E and k_m correspond to wave numbers at the Eckhaus and the marginal stability boundaries for the same Rayleigh number. A narrower range of allowed wave numbers is also implied by the weakly nonlinear theory based on perturbation expansion of the complete convection equations, which was initiated by Gor'kov [82], Malkus et al. [122] and developed by Schlüter et al. [171].

For $Ra \gg Ra_c$, the two-dimensional flow may give way to steady three-dimensional convection, and eventually to chaotic or turbulent convection [3, 46, 176, 208]. The nature of a variety of possible instabilities with different symmetries has been documented by Busse and coworkers [37, 38, 40], who numerically investigated the stability of a family of straight parallel rolls with respect to general three-dimensional perturbations. Their study has proven highly valuable in characterizing experimental observations, and it makes Rayleigh-Bénard convection "the best characterized nonlinear pattern forming system" [56].

While most theoretical results on Rayleigh-Bénard convection have been obtained for an ideal system of infinite geometry, appropriate boundary conditions must be applied in a real system, which is typically a finite convection cell with rigid sidewalls [57, 63]. For a two-dimensional system with rectangular symmetry, the lateral extent is usually described by introducing the aspect ratio Γ, defined as the ratio of the length of the system l to its height d. Rigid sidewalls tend to suppress the fluid flow via viscous effects, and this has been confirmed by experiments [201] in which the amplitude of the flow velocity was seen to vanish at the sidewalls. Such a boundary condition shifts the convection threshold [6], and results in an even further restricted

band of stable wave numbers [56].

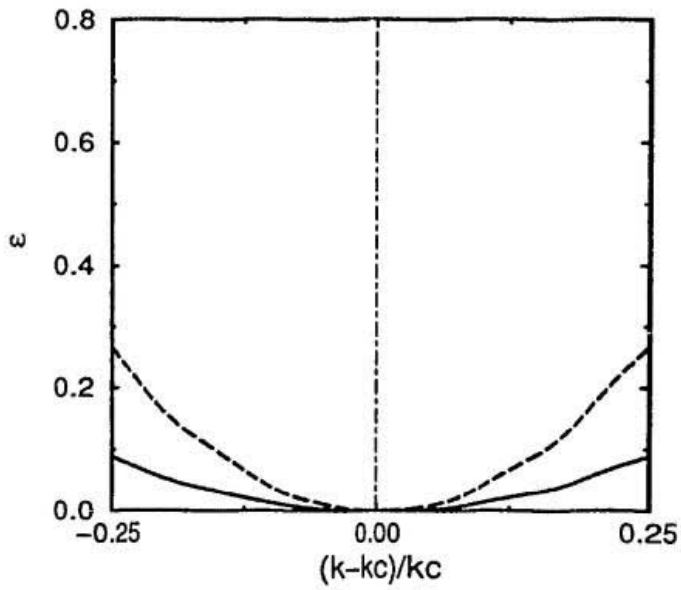

Figure 1.3: The marginal stability boundary (solid curve) and the Eckhaus boundary (dashed curve) for the one-dimensional Ginzburg-Landau equation. The parameters of the equation are chosen to correspond to Rayleigh-Bénard convection.

1.4 The Ginzburg-Landau Model

The Ginzburg-Landau model, which was first introduced to describe phase transitions in superconductors [80], provides a starting point for understanding many aspects of pattern formation in convective systems.

1.4.1 The Amplitude Equation

The one dimensional Ginzburg-Landau amplitude equation has the form [4]

$$\tau_0 \frac{\partial A}{\partial t} = \xi_0^2 \frac{\partial^2 A}{\partial x^2} + \varepsilon A - g|A|^2 A, \tag{1.4}$$

where ε is normalized control parameter which is defined by $\varepsilon \equiv (Ra - Ra_c)/Ra_c$ for thermal convection, and which measures the distance from the threshold of convection. The parameters τ_0 and ξ_0 represent the characteristic time and length scales of the variations of the pattern respectively, and g is the nonlinear coupling constant of the system. The complex amplitude $A(x,t)$ is related to the velocity field for a convective system and may be conveniently written as

$$A(x,t) = A_0(x,t)e^{i\phi(x,t)}, \tag{1.5}$$

in which the time evolution of the modulus $A_0(x,t)$ (amplitude intensity) and the phase $\phi(x,t)$ (wavelength modulation) can be expressed as [124]

$$\tau_0 \frac{\partial A_0}{\partial t} = \left[\varepsilon - \xi_0^2 (\frac{\partial \phi}{\partial x})^2\right] A_0 + \xi_0^2 \frac{\partial^2 A_0}{\partial x^2} - g A_0^3, \tag{1.6}$$

$$\tau_0 \frac{\partial \phi}{\partial t} = \xi_0^2 \left(\frac{\partial^2 \phi}{\partial x^2} + \frac{2}{A_0}\frac{\partial A_0}{\partial x}\frac{\partial \phi}{\partial x}\right). \tag{1.7}$$

These equations show that, for a spatially uniform system, the relaxation of the phase is mostly diffusive, and the evolution of the modulus is mainly controlled by a balance between εA_0 and gA_0^3. Very close to onset, if both

the spatial and temporal modulations of the pattern are small, the equation for the amplitude A_0 takes a simpler form:

$$\tau_0 \frac{dA_0}{dt} = \varepsilon A_0 - g A_0^3. \tag{1.8}$$

This is often referred to as Landau equation [4].

The trivial steady state solution $A_0 = 0$ of the Landau equation corresponds to the motionless steady state that is stable for $\varepsilon < 0$, but unstable for $\varepsilon > 0$. For $\varepsilon > 0$, the convection regime is represented by a nontrivial solution

$$|A_0| = \sqrt{\varepsilon / g}. \tag{1.9}$$

From the point of view of a dynamical systems approach [85], such a continuous change of the qualitative structure of solutions when a control parameter is varied is called a *forward* or *supercritical* bifurcation, analogous to a second order transition in equilibrium systems, and in contrast to the *backward* or *subcritical* bifurcation which is the analogue of a first order phase transition.

1.4.2 Relaxation Time and Correlation Length

In addition to the stationary solution of the Landau equation described above, the general time-dependent solution can also be obtained with appropriate initial conditions. Assuming the amplitude is initially $A_0(t = 0) = A_i$, integration of the Landau equation (1.8) gives

$$A_0(t) = \left(\frac{\varepsilon A_i^2 e^{\frac{2t}{\tau}}}{\left(\varepsilon - g A_i^2\right) + g A_i^2 e^{\frac{2t}{\tau}}} \right)^{1/2}. \tag{1.10}$$

In this expression, $\tau = \tau_0 \varepsilon^{-1}$ represents the relaxation time of the system, and its value diverges as ε approaches zero.

On the other hand, to look at spatial modulations of the pattern, one has to consider stationary solutions to the Ginzburg-Landau equation, for which $\partial A_0/\partial t = 0$. Equation (1.6) then becomes

$$\xi_0^2 \frac{d^2 A_0}{dx^2} = -\varepsilon A_0 + g A_0^3. \tag{1.11}$$

With the boundary conditions $A_0(x = 0) = 0$ and $A_0(x \to \infty) = \sqrt{\varepsilon/g}$ (from Eq. (1.9)), solution of Eq. (1.11) shows that the time-independent stationary state has an envelope of the form

$$A_0(x) = \sqrt{\frac{\varepsilon}{g}} \tanh\left(\frac{x}{\sqrt{2}\xi}\right), \tag{1.12}$$

where $\xi = \xi_0 \varepsilon^{-1/2}$ is the correlation length, which diverges as ε vanishes. In Chapter 4, we present experimental measurements of both ξ and τ for our system.

1.4.3 The Range of Stability

In general, the range of stability of the solutions of the one-dimensional Ginzburg-Landau equation can be found by substituting a disturbance of the form [4]

$$A(x,t) = a_0 e^{\omega t + i(k-k_c)x}, \tag{1.13}$$

where ω represents the growth rate of a mode with wave number k, and k_c is the critical wave number. For an infinite system where boundary conditions do not play a role, the marginal curve (on which $\omega = 0$) can be obtained from the Ginzburg-Landau equation,

$$\varepsilon_m = (k - k_c)^2 \xi_0^2. \tag{1.14}$$

Patterns with wave number k will grow if $\varepsilon > \varepsilon_m$, but decay if $\varepsilon < \varepsilon_m$. For $\varepsilon > \varepsilon_m$, the Ginzburg-Landau equation has steady-state spatially uniform

solutions $A_0 = [(\varepsilon - \varepsilon_m)/g]^{1/2}$. However, these steady-state solutions [4] are only stable in a narrower region $\varepsilon > \varepsilon_E$, with

$$\varepsilon_E = 3(k - k_c)^2 \xi_0^2. \tag{1.15}$$

This quadratic boundary marks the Eckhaus instability at which patterns become linearly unstable with respect to slow spatial modulations of the periodic structure. Therefore, stable pattern at a given ε should be observable only over the wave number range

$$|k - k_c| < \sqrt{\frac{\varepsilon}{3\xi_0^2}}. \tag{1.16}$$

In Figure 1.3, the marginal and the Eckhaus stability boundaries for Rayleigh-Bénard convection ($\xi_0 = 0.38d$ and $\lambda_c = 2.0d$) are plotted.

While a laterally infinite system is attractive from a theoretical point of view since it simplifies the calculations, lateral boundaries confine the fluid in any laboratory experiment. Theoretical analysis based on one-dimensional convection models [54, 55, 108, 154, 193], as well as numerical work based on the full hydrodynamic equations [8, 129] of Rayleigh-Bénard convection, predicts an even more restricted band of stable wave numbers due to the presence of rigid boundaries, as compared to the Eckhaus boundary for infinite systems. However, no convection experiment has been carried out [125] that unambiguously verifies this prediction. In our experiments, we have measured the stability boundary for one-dimensional convection patterns. We see evidence for this boundary induced wavelength selection mechanism. This mechanism will be discussed in more detail in Chapter 4.

Starting from full nonlinear convection equations for Rayleigh-Bénard convection, Segel [173] and Newell et al. [139] independently derived an amplitude equation that is identical to the Ginzburg-Landau equation in the one-dimensional case. For electroconvection in nematic liquid crystals, similar amplitude equations have also been obtained from the complete system

of electrohydrodynamic equations by the Bayreuth group [27, 98, 99, 106]. For our two-dimensional electrically driven convective system, close to onset, the experimental results, discussed in Chapter 4, are consistent with what would be expected from the Ginzburg-Landau equation, although the connection between the amplitude equation and the governing electrohydrodynamic equations has not been worked out.

1.5 Electroconvective Instability

Rayleigh-Bénard convection is driven by the buoyant force due to gravity. In contrast, convection driven by an electric force due to an applied electric field is called electrohydrodynamic convection, or *electroconvection*. The experimental control parameters of electroconvection are often easily accessible [56], and the observation of electroconvection patterns was first described by Avsec et al. [10]. Since then, electroconvection systems have been widely used for studies of pattern formation and the transition to turbulence [56]. Under the action of an electric field, there are basically two types of electrohydrodynamic instability which have been understood to some extent. These are electroconvection in isotropic dielectric fluids subject to ion injection, and electroconvection in nematic liquid crystals with negative dielectric anisotropy.

Electroconvection in isotropic dielectric fluids [9, 73, 113] is driven by the nonuniform distribution of space charge which originates from ion injection at one or both of the parallel plane electrodes which enclose the liquid. The transport mechanism [47, 123, 149] is different from that in the Rayleigh-Bénard problem, since charge carriers move by diffusion and migration under the action of the electric field, while heat is transferred solely by diffusion. Convective motion in a dielectric liquid subjected to ion injection may organize itself into two-dimensional rolls or hexagonal patterns, and the amplitudes of the current and the flow velocity exhibit hysteresis [9] as the control parameter is varied through the onset of convection. This hysteresis indicates that the convection onset in this case is subcritical, in contrast to the supercritical bifurcation observed in Rayleigh-Bénard convection.

At least partly because of three-dimensional nonlinear coupling between the space charge and the velocity field via Maxwell interactions, electroconvection in isotropic dielectric fluids has received far less attention than Rayleigh-Bénard convection, where the linear Boussinesq approximation [97]

is often assumed. The electrohydrodynamic instability in nematic liquid crystals, on the other hand, has attracted growing interest. It is probably the simplest anisotropic pattern forming system. One of the most significant experimental results on this system is the verification of the Eckhaus stability boundary [121, 137, 161] predicted by the Ginzburg-Landau equation.

The setup for observing electroconvection in nematics consists of a thin nematic layer sandwiched between two plane electrodes, with the director oriented parallel to the electrode surface [109]. The instability[1] depends on the anisotropic nature of the material and the finite conductivity of nematics is essential [45, 88, 147]. As the applied voltage reaches a certain threshold, a roll pattern with a periodic distortion of the nematic alignment appears. These rolls were first observed by Williams [203] and Kapustin et al. [100], and are now commonly referred to as Williams domains. At higher voltages, the Williams domains become disordered, with defects created and annihilated continuously [137, 162].

The unique structure and flow properties of the freely suspended smectic film make it an attractive system for the study of two-dimensional hydrodynamics. The layer structure of the smectic A phase constrains the flow to remain in the plane of the film. The first experiments on flow in freely suspended smectic films were carried out by Morris et al. in 1990 [131, 133]. By applying an electric field in the plane of the film, they observed one-dimensional convective patterns in the form of a series of two-dimensional

[1] In the presence of an electric field and a small distortion of the director, the conductivity anisotropy ($\sigma_\parallel > \sigma_\perp$) produces charge separation such that space charges are focused at locations where the director bends. For nematics with negative dielectric anisotropy ($\epsilon_\parallel < \epsilon_\perp$), liquid crystal molecules tend to align themselves normal to the applied electric field. Therefore, a dielectric torque that enhances the initial director distortion may result due to the transverse field created by space charge distribution. On the other hand, the accumulated space charges are subjected to a bulk electric force which drives a velocity field and thus exerts a strong hydrodynamic torque on the liquid crystal molecules. This is reinforced by the dielectric torque and eventually, via viscous coupling, the fluid motion amplifies the spatial variation of the director, yielding more charge separation and more fluid motion, and producing a growing instability.

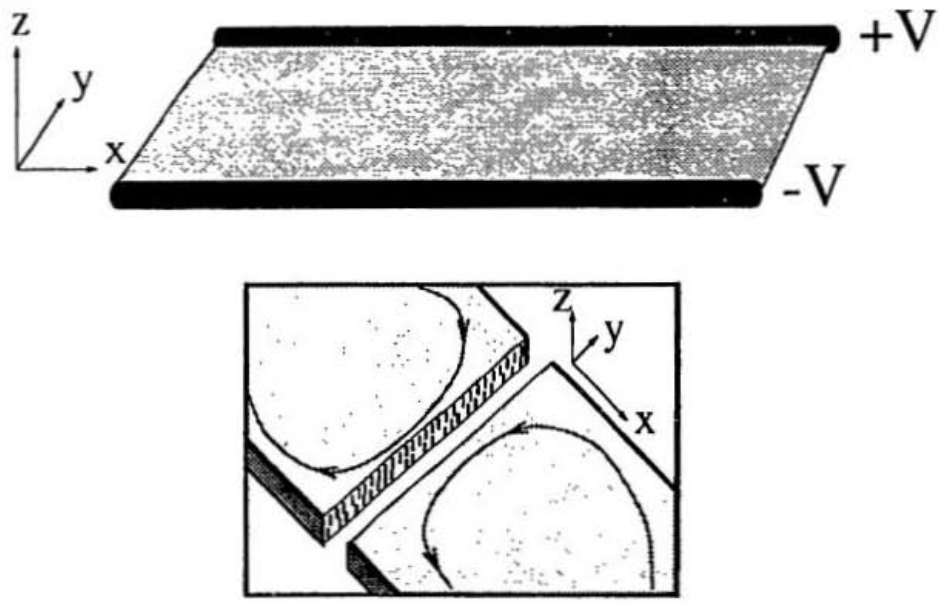

Figure 1.4: Schematics of electroconvection in two dimensions. Upper graph: a two-dimensional film is suspended between two electrodes which are maintained at an applied voltage $\pm V$. Lower graph: illustration of the profile of a converting smectic film with two molecular layers in thickness.

vortices. Just above the onset of convection, their velocity measurements indicated that the convection was well described by a single Fourier mode, whereas several modes were present further above onset. Measurements of the electric current through the film showed an enhanced charge transport due to convection, and no hysteresis was observed at onset. Their visual observations, as well as the current result, suggested that the onset of convection was a forward or supercritical bifurcation, as in Rayleigh-Bénard convection.

The basic setup of our experiments is similar to that of Morris et al. [133] and is shown in Figure 1.4. A smectic film is suspended by two linear coplanar wire electrodes through which a d.c. electric field is applied in the plane of the film. The onset behaviour and the nonlinear convection state have been investigated in our experiments. In particular, the correlation length ξ and the relaxation time τ are determined for our system, and the stability boundary for convection above onset has been measured.

The remainder of the thesis is organized as follows: Chapter II presents a theoretical model for two-dimensional electroconvection. A set of electrohydrodynamic equations is derived and the microscopic convection mechanism is analyzed. Chapter III is a general description of the experimental setup and measurement procedures. Chapter IV presents experimental measurements of the onset of convection, convection above onset, and the stability boundary for convective patterns. It also contains an analysis of the main findings of our experiments — the critical behavior and the wavelength selection — in terms of Ginzburg-Landau theory. Chapter V is a conclusion and brief discussion of possible future work. In Appendix A a hydrodynamic model is proposed to describe the observation of flow vortices at the lateral boundaries below the convective onset. Finally, Appendix B discusses colour measurement, which was used in determining the thickness of the freely suspended smectic film.

Chapter 2

Theory

Overview

In this chapter, we develop a theoretical framework for a two-dimensional isotropic fluid exposed in a nonuniform electric field. In section 2.1, we write down the electrohydrodynamic equations for a three-dimensional isotropic fluid in a nonuniform electric field. In section 2.2, we develop a linearized system for two-dimensional electroconvection and analyze the convection mechanism. In section 2.3, we show that the correct normalized control parameter for our system is $\varepsilon = V^2/V_c^2 - 1$.

2.1 Hydrodynamic Equations for Isotropic Fluids in a Nonuniform Electric Field

Consider a three-dimensional isotropic fluid with a small conductivity in a nonuniform electric field. Conservation of mass may be expressed as [37, 114]

$$\frac{\partial \rho_m}{\partial t} + \nabla \cdot (\rho_m \mathbf{v}) = 0, \tag{2.1}$$

where $\mathbf{v}$ is flow velocity, and ρ_m the mass density. For an incompressible fluid, Eq. (2.1) reduces to

$$\nabla \cdot \mathbf{v} = 0. \tag{2.2}$$

Assuming that the only external force acting on the fluid is due to the electric field, the momentum equation can be written as

$$\rho_m \frac{\partial \mathbf{v}}{\partial t} + \rho_m \mathbf{v} \cdot \nabla \mathbf{v} = -\nabla p + \mu \nabla^2 \mathbf{v} + \mathbf{F}_e, \tag{2.3}$$

where p denotes the pressure and μ the viscosity. In general, for a nonuniform electric field $\mathbf{E}$, the electric force $\mathbf{F}_e$ may be expressed as [115]

$$\mathbf{F}_e = \rho_e \mathbf{E} + \frac{1}{2}\nabla \left[\rho_m \left(\frac{\partial \epsilon}{\partial \rho_m} \right) E^2 \right] - \frac{1}{2} E^2 \nabla \epsilon, \tag{2.4}$$

where ρ_e is the space charge density in fluid, and ϵ the dielectric permittivity of the fluid. The first term on the right hand side of Eq. (2.4) originates from the interaction between free charges in the fluid and the electric field, while the other two terms arise due to polarization in the nonuniform field.

We assume that ϵ is a function only of the mass density ρ_m, that is, $\epsilon = \epsilon(\rho_m)$ and

$$\nabla \epsilon = \left(\frac{\partial \epsilon}{\partial \rho_m} \right) \nabla \rho_m. \tag{2.5}$$

We further consider a linear dependence of ϵ on ρ_m,

$$\epsilon = \epsilon_0 (1 + \gamma \rho_m), \tag{2.6}$$

which is an approximation to the Clausius-Mossotti relation if γ is small [25, 29, 95]. Here ϵ_0 denotes the permittivity of free space, and γ is a positive constant depending on the material. Therefore, the electric force $\mathbf{F}_e$ has the simpler form

$$\mathbf{F}_e = \rho_e \mathbf{E} + \frac{1}{2}\rho_m \left(\frac{\partial \epsilon}{\partial \rho_m}\right) \nabla E^2. \tag{2.7}$$

For a weakly conducting fluid, magnetic fields are negligible, and Maxwell's equations for a quasi-static electric field become [69, 95]

$$\nabla \times \mathbf{E} = 0, \tag{2.8}$$

$$\nabla \cdot (\epsilon \mathbf{E}) = \rho_e. \tag{2.9}$$

In addition, the charge conservation equation is

$$\begin{aligned} \frac{\partial \rho_e}{\partial t} &= -\nabla \cdot \mathbf{J}, \\ &= -\nabla \cdot \mathbf{j} + \alpha \nabla^2 \rho_e, \end{aligned} \tag{2.10}$$

where $\mathbf{J}$ is the total electric current density which includes contributions due to migration and convection ($\mathbf{j}$), and due to charge diffusion with diffusion coefficient α. The electric current density due to migration and convection is assumed to have the form

$$\mathbf{j} = \sigma \mathbf{E} + \rho_e \mathbf{v}, \tag{2.11}$$

where σ is the conductivity of the liquid, assumed to be constant. In writing Eq. (2.11), it has been considered that the fluid behaves like a weak ohmic conductor, as is the case for smectic film below the onset of electroconvection [134].

Throughout the following analysis, we consider ρ_m to be constant. Collecting together the above equations we have

$$\nabla \cdot \mathbf{v} = 0, \tag{2.12}$$

$$\rho_m \frac{\partial \mathbf{v}}{\partial t} + \rho_m \mathbf{v} \cdot \nabla \mathbf{v} = -\nabla p + \mu \nabla^2 \mathbf{v} + \rho_e \mathbf{E} + \frac{1}{2} \rho_m \left(\frac{\partial \epsilon}{\partial \rho_m} \right) \nabla E^2, \quad (2.13)$$

$$\frac{\partial \rho_e}{\partial t} + \mathbf{v} \cdot \nabla \rho_e = -\nabla \cdot (\sigma \mathbf{E}) + \alpha \nabla^2 \rho_e, \quad (2.14)$$

$$\nabla \cdot (\epsilon \mathbf{E}) = \rho_e, \quad (2.15)$$

$$\nabla \times \mathbf{E} = 0, \quad (2.16)$$

with

$$\epsilon = \epsilon_0 (1 + \gamma \rho_m). \quad (2.17)$$

Given appropriate initial and boundary conditions, the electrohydrodynamic problem posed above reduces to solving the system of equations (2.12 - 2.17).

2.2 Mechanism of Two-Dimensional Electroconvection

A smectic liquid crystal film behaves as a two-dimensional isotropic liquid. The equations for electroconvection in the film can be approximated as the two-dimensional version of the governing equations for a three-dimensional isotropic, incompressible fluid derived above. In the following, we will confine ourselves to a purely two-dimensional system, with $\mathbf{v} = (v_x, v_y)$, $\nabla = (\partial/\partial x, \partial/\partial y)$, and with $\varrho_e = \varrho_e(x, y)$ and $\mathbf{E} = (E_x, E_y)$, denoting the charge density and the components of the electric field in the plane of the film respectively. In a rigorous analysis, the two-dimensional limit of Eqs. (2.12 - 2.17) must be taken with some care, since the electromagnetic part of the problem remains three-dimensional [58], and the transport coefficients of the fluid may not be well-behaved in purely two-dimensional system [119]. We neglect such details here.

Consider a smectic film (Figure 1.4), infinitely long in the x-direction and infinitely thin in the z-direction, spanned by two ideal parallel wire electrodes separated by a distance d in the y-direction. The two-dimensional versions of Eqs. (2.13) and (2.14) are

$$\rho_m \frac{\partial \mathbf{v}}{\partial t} + \rho_m \mathbf{v} \cdot \nabla \mathbf{v} = -\nabla p + \mu \nabla^2 \mathbf{v} + \varrho_e \mathbf{E} + \frac{1}{2} \gamma \epsilon_0 \rho_m \nabla E^2, \quad (2.18)$$

$$\frac{\partial \varrho_e}{\partial t} + \mathbf{v} \cdot \nabla \varrho_e = -\frac{\sigma}{\epsilon} \varrho_e + \alpha \nabla^2 \varrho_e, \quad (2.19)$$

in which p is the isotropic pressure for two-dimensional fluid. Here we have used Eq. (2.17) to obtain the last term on the right hand side in Eq. (2.18), and Eqs. (2.14) and (2.15) have been combined to give Eq. (2.19)[1]

[1] In writing Eq. (2.19), we have made the following approximations.

For smectic A liquid crystals, Eqs. (2.14) and (2.15) can be written as

$$\frac{\partial \rho_e}{\partial t} + \mathbf{v} \cdot \nabla \rho_e = -\sigma_\perp \left(\frac{\partial E_x}{\partial x} + \frac{\partial E_y}{\partial y} \right) - \sigma_\parallel \frac{\partial E_z}{\partial z} + \alpha \nabla^2 \rho_e, \quad (2.20)$$

Equations (2.18) and (2.19) serve as a starting point for the elucidation of the mechanism for two-dimensional electroconvection. The relevant values of ϵ, μ, and α are those in the plane of the film, and σ here denotes an effective conductivity for the two-dimensional film. In the motionless base state, the electric field $\mathbf{E}^0$ and the charge density distribution ϱ_e^0 are

$$\mathbf{E}^0 = (0, E^0(y)), \tag{2.25}$$

and

$$\varrho_e^0 = \varrho_r^0(y), \tag{2.26}$$

with

$$\int_0^d E^0(y)dy = 2V^0, \tag{2.27}$$

---

and

$$\epsilon_\perp \left(\frac{\partial E_x}{\partial x} + \frac{\partial E_y}{\partial y} \right) + \epsilon_\parallel \frac{\partial E_z}{\partial z} = \rho_e. \tag{2.21}$$

Solving Eq. (2.21) for $(\partial E_x/\partial x + \partial E_y/\partial y)$ and substituting into Eq. (2.20) gives

$$\frac{\partial \rho_e}{\partial t} + \mathbf{v} \cdot \nabla \rho_e = -\frac{\sigma_\perp}{\epsilon_\perp}\rho_e + \alpha \nabla^2 \rho_e + \left(\sigma_\perp \frac{\epsilon_\parallel}{\epsilon_\perp} - \sigma_\parallel \right) \frac{\partial E_z}{\partial z}. \tag{2.22}$$

By assuming that the charge density in the plane of a two-dimensional film can be written as

$$\varrho_e(x, y) = \lim_{s \to 0} \int \rho_e dz, \tag{2.23}$$

we obtain

$$\frac{\partial \varrho_e}{\partial t} + \mathbf{v} \cdot \nabla \varrho_e = -\frac{\sigma_\perp}{\epsilon_\perp}\varrho_e + \alpha \nabla^2 \varrho_e + \left(\sigma_\perp \frac{\epsilon_\parallel}{\epsilon_\perp} - \sigma_\parallel \right) \int \frac{\partial E_z}{\partial z} dz. \tag{2.24}$$

Here $\mathbf{v} = (v_x, v_y)$ and $\nabla = (\partial/\partial x, \partial/\partial y)$. In writing this equation, we have ignored diffusion in the z-direction.

We now introduce an effective conductivity σ^* for the two-dimensional film and make the approximation that the contribution from the first and last terms of the right hand side of Eq. (2.24) can be integrated to give $(\sigma^*/\epsilon_\perp)\varrho_e$. We then obtain Eq. (2.19) in which, for simplicity, we have written σ rather than σ^*. The detailed connection between the three-dimensional electric field and the two-dimensional hydrodynamics is beyond the scope of this thesis [58].

where the two electrodes are maintained at $\pm V^0$. By setting $\mathbf{v} = 0$ in Eq. (2.18), we find that in the motionless state,

$$\nabla p^0 = \varrho_e^0 \mathbf{E}^0 + \frac{1}{2}\gamma\epsilon_0\rho_m \nabla (E^0)^2, \tag{2.28}$$

from which we see that the static pressure p^0 in the film in a nonuniform field is different from that when the applied field is uniform.

We now apply small perturbations to the motionless state. We introduce the perturbation velocity $\mathbf{v}'$, electric field $\mathbf{E}'$, charge density ϱ'_e and pressure p' such that

$$\mathbf{v} = \mathbf{v}', \tag{2.29}$$

$$\mathbf{E} = \mathbf{E}^0 + \mathbf{E}', \tag{2.30}$$

$$\varrho_e = \varrho_e^0 + \varrho_e', \tag{2.31}$$

$$p = p^0 + p'. \tag{2.32}$$

It is worth noticing that the contribution due to the nonuniform electric field in the momentum equation is the gradient of a scalar and thus can be incorporated in the pressure gradient term by defining an effective pressure $P \equiv p - \frac{1}{2}\gamma\epsilon_0\rho_m E^2$. From this definition, the perturbation for the effective pressure is $P' = p' - \gamma\epsilon_0\rho_m(\mathbf{E}^0 \cdot \mathbf{E}')$. It is also convenient to express $\mathbf{E}'$ in terms of a perturbed electric potential ϕ' defined through $\mathbf{E}' = -\nabla\phi'$.

If Eqs. (2.18) and (2.19) are linearized in the small perturbations, we obtain

$$\rho_m \frac{\partial \mathbf{v}}{\partial t} = -\nabla P' + \mu\nabla^2\mathbf{v} + \varrho_e'\mathbf{E}^0 - \varrho_e^0\nabla\phi', \tag{2.33}$$

$$\frac{\partial \varrho_e'}{\partial t} = -\mathbf{v}\cdot\nabla\varrho_e^0 - \frac{\sigma}{\epsilon}\varrho_e' + \alpha\nabla^2\varrho_e'. \tag{2.34}$$

Together with the incompressibility condition

$$\nabla \cdot \mathbf{v} = 0 \tag{2.35}$$

and Gauss' Theorem

$$\nabla^2\phi' = -\frac{\varrho_e'}{\epsilon}, \tag{2.36}$$

Eqs. (2.33 - 2.36) are a set of five equations for the five unknown functions, $v_x, v_y, \varrho_e', \phi'$, and P'. With appropriate boundary conditions[2], these equations are a complete linearized system for the two-dimensional electroconvection problem.

After some algebra similar to that used in the analysis of Rayleigh-Bénard convection [48], Eqs. (2.33) and (2.34) can be further simplified to give

$$\left(\frac{\partial}{\partial t} - \nu\nabla^2\right)\nabla^2 v_y = \frac{E^0}{\rho_m}\left(\frac{\partial^2\varrho_e'}{\partial x^2}\right) + \frac{1}{\rho_m}\frac{\partial\varrho_e^0}{\partial y}\left(\frac{\partial^2\phi'}{\partial x^2}\right), \tag{2.37}$$

$$\left(\frac{\partial}{\partial t} - \alpha\nabla^2\right)\varrho_e' = -v_y\frac{\partial\varrho_e^0}{\partial y} - \frac{\sigma}{\epsilon}\varrho_e', \tag{2.38}$$

where $\nu = \mu/\rho_m$ is the kinematic viscosity. It can be seen, from Eq. (2.37), that the spatial variation of the perturbed charge density causes convection ($\partial v_y/\partial t \neq 0$), while convection will in turn, from Eq. (2.38), modify the charge distribution ($\partial\varrho_e'/\partial t \neq 0$). On the other hand, viscosity and charge diffusion damp out the perturbations.

It is important to note that the source of the space charges in the film is not contained in the above analysis. Furthermore, while the velocity field can be exactly two-dimensional, the electric field remains three-dimensional. In fact, the z-component of the electric field is responsible for the generation of a charge distribution at the two smectic-air interfaces, and this charge distribution can interact with the in-plane components of the field to cause flow instability. The electrochemical dissociation of dopants in liquid crystal materials might also affect the charge distribution generated by the z-component of the electric field, however, details of such a influence is not yet clear.

[2]for our electroconvection system, we may choose $v_x = v_y = 0$, $\partial v_\perp/\partial x = \partial v_y/\partial y = 0$, and $\phi' = 0$ for $y = 0, d$

It is interesting to observe that the term containing effective pressure gradient $\nabla P'$ has been eliminated in the analysis. Hence the effect of polarization is not responsible for the origin of electroconvection in an incompressible fluid with constant mass density. However, as discussed before, the polarization due to a nonuniform electric field does influence the pressure distribution in the fluid, so it cannot be ignored for the discussion of static equilibrium of a dielectric fluid. It must be emphasized that the electroconvection model proposed here involves the assumption that the fluid has a constant mass density ρ_m (therefore constant ϵ), although the electric field is nonuniform. In cases that this assumption breaks down (such as when a temperature perturbation is involved), the effect of polarization may contribute to the convective motion [168, 194, 195, 196, 197] and in general, an extra term of the form $\frac{1}{2}E^2\nabla\epsilon$ will then be involved, as seen from Eq. (2.4).

2.3 The Dimensionless Control Parameter

A complete solution of Eqs. (2.37) and (2.38) is beyond the scope of this thesis, however a linear stability analysis of this problem is being carried out by Daya et al. [58]. Without a complete solution, simple dimensional analysis [14] can give some insight as to the dimensionless control parameter for two-dimensional electroconvection. For simplicity, we drop the term involving ϕ' in Eq. (2.37), and ignore the charge diffusion term in Eq. (2.38). In doing so, we have assumed that the influence on the electric field of the perturbed charge density in a liquid film of vanishing thickness is negligible, and that the coefficient of charge diffusion is small [148, 191]. Furthermore, in analogy with the base state temperature distribution for Rayleigh-Bénard convection, we make the approximation that the charge distribution ϱ_e^0 of the base state depends linearly on y, that is, $\partial\varrho_e^0/\partial y = \beta$ with β constant.

Equations (2.37) and (2.38) can then be rewritten as

$$\left(\frac{\partial}{\partial t} - \nu\nabla^2\right)\nabla^2 v_y = \frac{E^0}{\rho_m}\left(\frac{\partial^2 \varrho_e'}{\partial x^2}\right), \tag{2.39}$$

$$\left(\frac{\partial}{\partial t} + \frac{\sigma}{\epsilon}\right)\varrho_e' = -\beta v_y. \tag{2.40}$$

We introduce ϵ/σ as a characteristic time, d as a characteristic length, and use βd as a characteristic charge density. We write

$$v_y = \left(\frac{\sigma d}{\epsilon}\right)\mathcal{V}(\tilde{y})e^{i\tilde{k}\tilde{x}+\tilde{\omega}\tilde{t}}, \tag{2.41}$$

$$\varrho_e' = (\beta d)\,\mathcal{R}(\tilde{y})e^{i\tilde{k}\tilde{x}+\tilde{\omega}\tilde{t}}, \tag{2.42}$$

in which $\mathcal{V}(\tilde{y})$ and $\mathcal{R}(\tilde{y})$ are dimensionless variables related to the vertical velocity component and the charge density, $\tilde{k}$ and $\tilde{\omega}$ are the dimensionless wave number and growth rate, $\tilde{x}$ and $\tilde{y}$ are the dimensionless coordinates, and $\tilde{t}$ is the dimensionless time. Substitution of Eqs. (2.41) and (2.42) into

the Eqs. (2.39) and (2.40) yields

$$\left[\frac{\tilde{\omega}}{\epsilon\nu/\sigma d^2} - \left(D^2 - \tilde{k}^2\right)\right]\left(D^2 - \tilde{k}^2\right)\mathcal{V} = -\frac{E^0\beta\epsilon d^2}{\mu\sigma}\tilde{k}^2\mathcal{R}, \tag{2.43}$$

$$(\tilde{\omega} + 1)\,\mathcal{R} = -\mathcal{V}, \tag{2.44}$$

where D represents $d/d\tilde{y}$. In analogy to the Rayleigh-Bénard convection problem, we define an electric Prandtl number Pr^e and an electric Rayleigh number Ra^e as

$$Pr^e \equiv \frac{\epsilon\nu}{\sigma d^2}, \tag{2.45}$$

$$Ra^e \equiv \frac{E^0\beta\epsilon d^2}{\mu\sigma}. \tag{2.46}$$

These are the only two dimensionless parameters contained in the electroconvection equations. Eliminating $\mathcal{R}$ from Eq. (2.43) gives an equation for $\mathcal{V}$,

$$\left[\frac{\tilde{\omega}}{Pr^e} - \left(D^2 - \tilde{k}^2\right)\right]\left(D^2 - \tilde{k}^2\right)\mathcal{V} - Ra^e\frac{\tilde{k}^2}{\tilde{\omega}+1}\mathcal{V} = 0, \tag{2.47}$$

which has a similar form to the corresponding equation in the Rayleigh-Bénard convection problem [48, 211]. The marginal curve corresponds to $\tilde{\omega} = 0$, for which

$$\left(D^2 - \tilde{k}^2\right)^2\mathcal{V} + Ra^e\tilde{k}^2\mathcal{V} = 0, \tag{2.48}$$

which involves only the electric Rayleigh number Ra^e.

A complete solution of the electroconvection problem requires the knowledge of the base state charge density distribution ϱ_e^0, and thus of $\beta = \partial\varrho_e^0/\partial y$. We know that both the charge density distribution and the electric field in the base state originate from the voltage $\pm V$ applied to the two electrodes. From dimensional considerations and the Maxwell equations, both the characteristic charge density and the characteristic electric field intensity at base state should be proportional to V, that is, $[E^0] \propto V$ and $[\varrho_e^0] \propto V$. Therefore, from the definition of dimensionless control parameter Ra^e, we have

$$Ra^e \propto V^2. \tag{2.49}$$

The exact form of Ra^e will depend on the base state solution, which will involve the film thickness s as well as film width d.

As in the case for Rayleigh-Bénard convection, we define a normalized dimensionless control parameter Ra^e by

$$\varepsilon \equiv \frac{Ra^e - Ra_c^e}{Ra_c^e}. \tag{2.50}$$

Here Ra_c^e denotes the electric Rayleigh number at the onset of convection. Using Eq. (2.49), we thus obtain

$$\varepsilon = \frac{V^2}{V_c^2} - 1. \tag{2.51}$$

This is the form of normalized control parameter we use throughout this work. Its validity has been confirmed in experiments [134].

A complete linear stability analysis of the base state, as well as a subsequent weakly nonlinear analysis is necessary in order to get more insight into the nature of the onset and the dynamics of the two-dimensional convective patterns. Numerical simulations [43, 83] of this system would also be helpful. Such work falls beyond the scope of this thesis.

Chapter 3

Experiments

Overview

The experiments consist of applying a d.c. voltage across the plane of freely suspended smectic liquid crystal film, and studying the flow pattern which develops in the plane of the film. The experimental setup is described in section 3.1. Two techniques are employed to determine the thickness of the liquid crystal films, which typically contain two to about one hundred molecular layers. These techniques are described in detail in section 3.2. In section 3.3, the method of flow visualization used in these experiments is briefly discussed.

3.1 Experimental Setup

Experiments are performed on thin smectic films which are freely suspended between two electrodes. The film holder is shown in Figure 3.1.

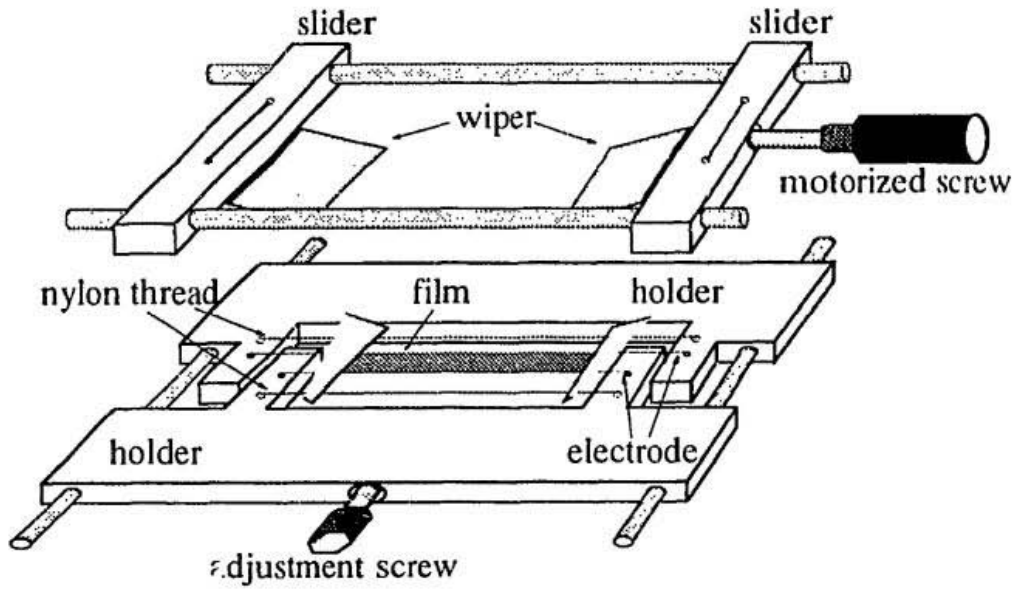

Figure 3.1: Construction of the film holder.

The long sides of the smectic liquid film are supported by two 23μm diameter tungsten wire electrodes which are under tension. The ends of the film are supported by plastic wipers 50μm in thickness and sharpened at the edges. The edges of the wipers contact the film directly, resting on the electrode wires under their own weight. Two nylon threads lie outside the electrode wires, acting to reduce the influence of the wipers' weight on the electrodes. The wipers are supported by two spring loaded plexiglass sliders. One of the sliders is fixed and the other one can be driven with a motorized

micrometer screw controlled by a Newport Model 850CD-1 motor controller. This allows variation of the film length l in the range $0 < l < 30$ mm. The electrodes and nylon threads are attached to two plexiglass holders shown in Figure 3.1. The separation of the electrodes d can be changed mechanically by moving one of these holders relative to the other. This is done by using a fine adjustment screw accessible from outside the housing that encloses the experimental cell. For the experiments reported here, d is in the range 0.5 mm$< d <$ 4.0 mm.

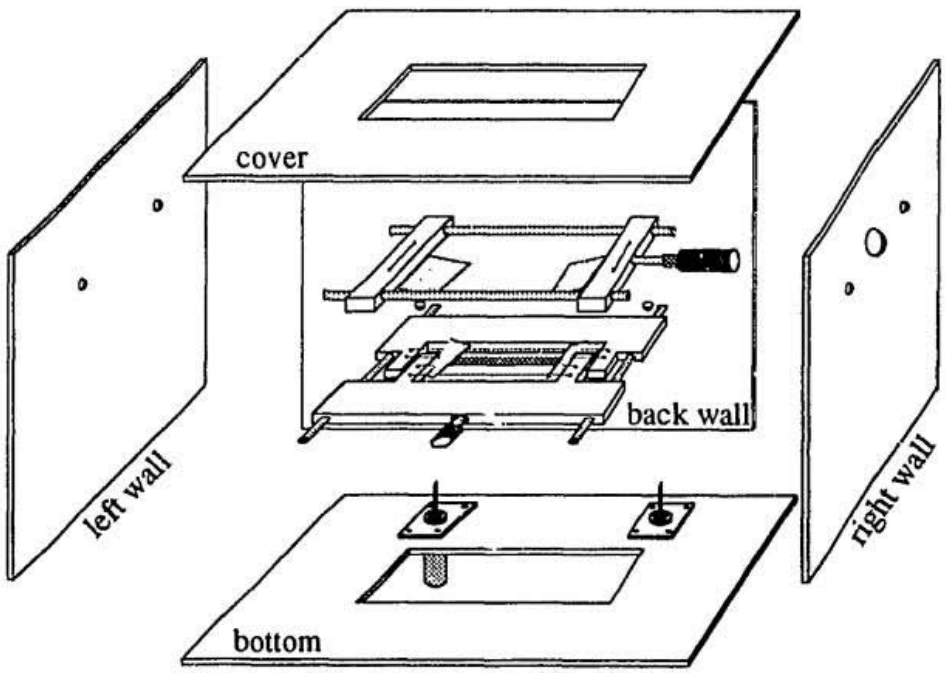

Figure 3.2: The convection cell mounted inside a shielding box with optical and electric access.

The film holder is mounted inside an aluminum box (12.5 cm x 10.0 cm

× 6.0 cm) as shown in Figure 3.2. The aluminum box provides electrical shielding. Windows in the top and bottom of the box allow optical access to the film. The box is placed in a plexiglass housing (29 cm × 29 cm × 15 cm). The temperature inside the housing is controlled to ±0.1°C over a given run by an Omega Model CN9111A temperature controller and a Cole-Parmer Model 12101-10 constant temperature water circulating system. All experiments were performed at temperatures in the range 25±1°C, well below the smectic-nematic transition at 33.5°C.

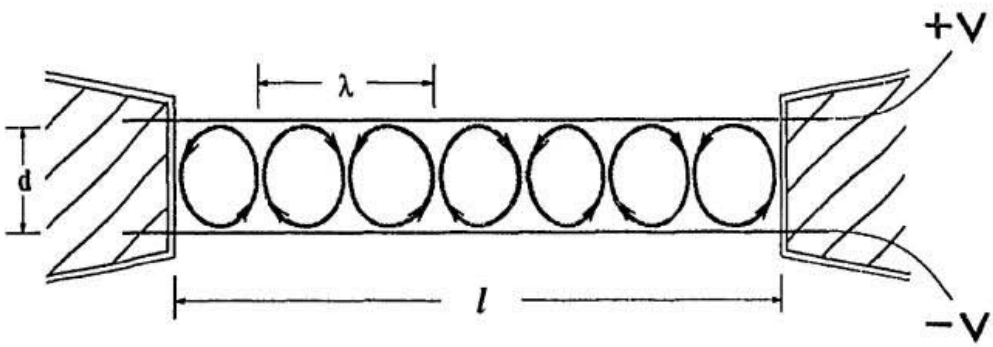

Figure 3.3: Schematic view of a convecting film. The film length l and width d, and the wavelength λ of the vortex pattern are illustrated.

The electric field that drives the electroconvection is produced by applying a constant potential difference across the two wire electrodes (Figure 3.3). Balanced potentials of $\pm V$ ($0 < V < 60$ volt) with respect to ground are generated by two Hewlett-Packard 6024A DC power supplies wired in series. The power supplies are controlled by a personal computer via a Data Translation DT2815 D/A converter board. Voltages are monitored using a Hewlett-Packard 34401A multimeter via a IEEE-488 interface board. The

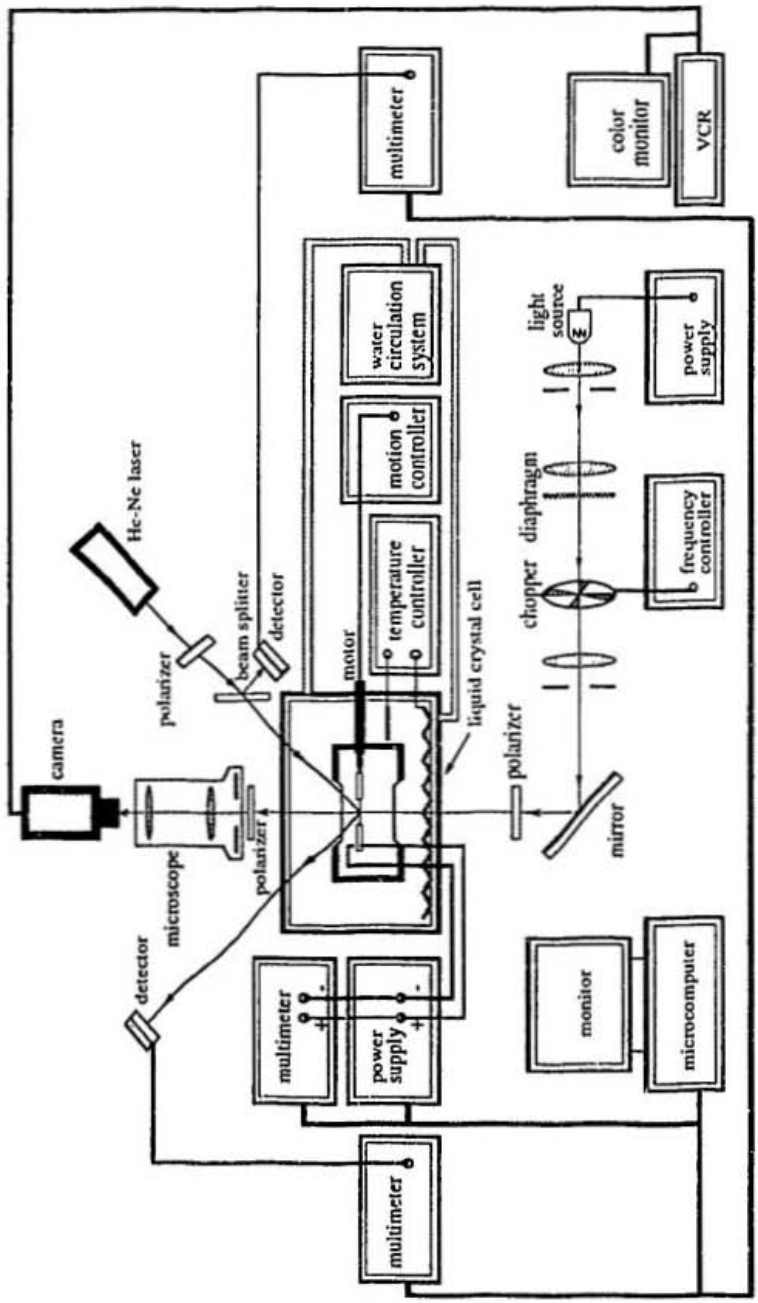

Figure 3.4: Schematic diagram of the electroconvection experiment setup.

entire experimental arrangement is shown in Figure 3.4.

The liquid crystal material used in the experiments is 4,4'-n-octylcyanobiphenyl (8CB), doped with a small amount (0.15% by weight) of tetracyanoquinodimethane (TCNQ) to control the nature of ionic impurities. 8CB is very chemically stable and has a smectic A mesophase between 21.0°C and 33.5°C. In this temperature range, the rod-like 8CB molecules associate themselves into layers with the long molecular axis normal to layer plane. The thickness of the smectic layer is 31.6Å, about 1.3 times the 8CB molecular length.

Films were made by bringing the two wipers together, placing a small amount of liquid crystal material at the place where the wipers joined, and then slowly drawing the wipers apart at an adjustable rate of several microns per second using the micropositioning motor driver. The relative wiper position with respect to an arbitrary zero can be controlled to within 1.0μm. Once the film reaches the desired length l, the motorized wiper is stopped. The film making process is monitored with a low power microscope, which is also used to monitor the film thickness and record the two-dimensional convective flow.

With some practice, uniform films can be made as thin as two molecular layers in thickness. A two-layer-thick film corresponds to the thinnest thickness for a film to be stable [151]. Such a film can last for several hours without breaking in experiments. In general, one can make an existing film thinner by a short and rapid movement of the wiper to slightly enlarge the film surface. This usually results in the creation of defects with fewer molecular layers, and these defects tend to expand over the film. A film is then made uniform by slowly drawing it further. Once a film is made uniform, its thickness can remain constant even in the presence of strong convection, or when the length of the film is slowly changed.

3.2 Film Thickness Determination

Observations indicate that the onset voltage for electroconvection depends on the thickness of the film. It is therefore important in each individual experiment to know the film thickness accurately. The film thickness is determined in two ways: by measuring the reflectivity of the film, and by measuring the colour of the film when it is illuminated by white light incident perpendicular to the film plane.

3.2.1 Measuring Reflected Intensity

Liquid crystal films in the smectic A mesophase are birefringent, with the optical axis normal to the plane of the film and therefore in the plane of an incident light beam. The reflectivity of the film depends on its thickness, so the thickness can be determined from measurement of the relative intensity of a beam of *s*-polarized monochromatic light reflected from the film plane.

The reflection coefficient of *s*-polarized (i.e., polarized perpendicular to the plane of incidence) light from a surface is given by [28]

$$R_s = \left| \frac{\cos\theta_i - (n_\perp{}^2 - \sin^2\theta_i)^{1/2}}{\cos\theta_i + (n_\perp{}^2 - \sin^2\theta_i)^{1/2}} \right|^2, \qquad (3.1)$$

where θ_i is the incidence angle and $n_\perp$ the refractive index perpendicular to the plane of incidence. For smectic A films, the optical axis is normal to the film surface, so $n_\perp$ is simply equal to n_o, the ordinary refractive index of the material.

A freely suspended smectic film is essentially a thin layer of smectic material with two free surfaces. The reflected beam received by a detector includes contributions due to reflections from both smectic-air interfaces. The intensity of *s*-polarized monochromatic light reflected from a smectic film N

molecular layers thick is given by [28]

$$I_{N\lambda} = I_{0\lambda}\frac{4R_s \sin^2(\phi/2)}{(1-R_s)^2 + 4R_s \sin^2(\phi/2)}, \tag{3.2}$$

where $I_{0\lambda}$ is the intensity of the incident light of wavelength λ, and $\phi/2$ is given by

$$\phi/2 = \frac{2\pi}{\lambda} N d_s (n_o^2 - \sin^2\theta_i)^{1/2}, \tag{3.3}$$

where d_s is the thickness of each smectic layer. The expression for $I_{N\lambda}$ implies periodicity of the reflected light intensity as a function of film thickness $s = N$ molecular layers.

The basic optical setup is shown in Figure 3.4. A Uniphase Model 1125 Helium-Neon laser (wavelength 6328Å, output power 10 mW) is used in all experiments. The laser output is unpolarized, and a polarizer in front of the laser is adjusted so that the polarization of the incident beam is perpendicular to the plane of incidence.

The polarized laser beam is directed onto the film at an angle of incidence θ_i of 45.0°±2.0° in all experiments. The intensity of the incident light is determined by a beam splitter-detector combination as illustrated in Figure 3.4. The intensity of the reflected beam is measured using an identical photodiode detector. The voltage output of the photodiode detectors is measured with Keithley Model 196 digital multimeters and transmitted by an IEEE-488 bus to the personal computer. A simple program in C was written to calculate the ratio of reflected to incident intensity $I_{N\lambda}/I_{0\lambda}$.

The 8CB used in our experiments has $d_s = 31.6$Å and $n_o = 1.516$ [65, 116]. Figure 3.5 illustrates the relative reflected intensity or reflectivity of the film $I_{N\lambda}/I_{0\lambda}$, calculated from Eq. (3.2), for films up to 200 molecular layers thick. Film thickness is determined by comparing the measured reflectivity with the calculated values. Due to the periodicity of the theoretical curve, a given reflectivity may correspond to any of a number of different film thicknesses.

However, if it is known in which period the thickness lies, high accuracy (the thickness determination is exact for films thinner than 15) can be achieved by considering the fact that the film thickness must be an integer number of molecular layers.

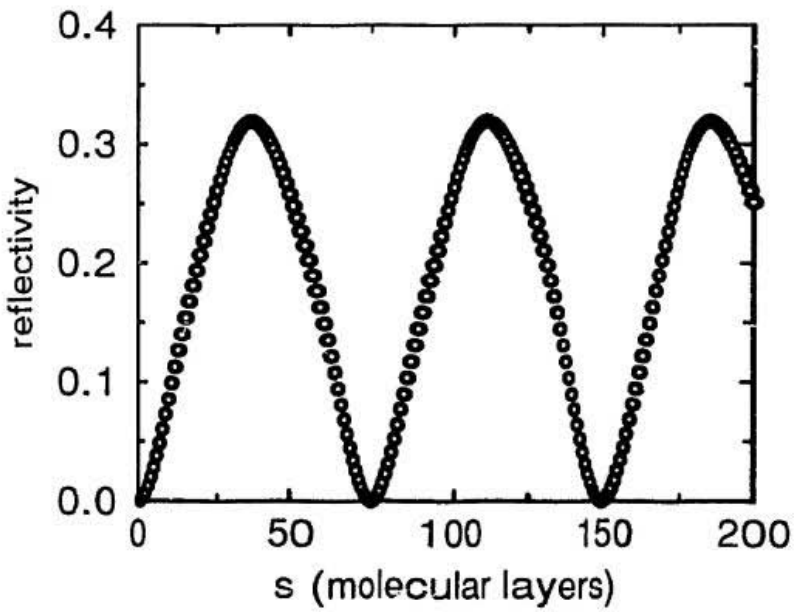

Figure 3.5: Reflectivity of an 8CB film as a function of film thickness calculated from Eq. (3.2). *s*-polarized light beam of wavelength 6328Å, at an incident angle 45.0°.

3.2.2 Measuring Reflected Colours

Since the thickness of our smectic films is comparable to the wavelength of visible light, they, like soap films, show brilliant interference colours when viewed under reflected white light. The thickness of a smectic film can therefore be determined by measuring the apparent reflected colour produced by incident white light.

The reflected intensity for s-polarized light of single wavelength λ and incidence angle θ_i from a smectic A film, with index of refraction n_o and consisting of N molecular layers each of thickness d_s, is given by Eq. (3.2). For s-polarized incident white light with a continuous spectral intensity distribution, the reflected intensity $I_{N\lambda}$ for each monochromatic component can also be determined from this expression. Once the reflected spectral intensity distribution is known, the reflected colour can be determined [51].

A General Electric Model 778D mini illuminator with a polarizer in front is used in all experiments. It is mounted inside a Riechert Model 580 stereo microscope and produces a s-polarized white beam incident normal to the smectic film plane (the incidence angle is therefore zero). A camera port on the microscope is fitted with either a 35mm Nikon SLR camera, or a Sony SSC-C354 CCD colour video camera connected to a Panasonic AG-1960 multiplex VHS recorder and a Hitachi CT1396VM colour video monitor. The microscope is also used for the flow visualization described in the following section.

A description of how colour is measured is presented in Appendix B. The spectral intensity distribution $I_{0\lambda}$ of the incident white light from the above illuminator is assumed to be that of the standard source A of the Commission Internationale de l'Eclairage (CIE) [51]. Using this incident intensity distribution, the spectral intensity distribution $I_{N\lambda}$ of the light reflected from a smectic film N molecular layers in thickness was determined using Eq. (3.2) at each wavelength λ.

As described in Appendix B, the spectral distribution of the reflected light $I_{N\lambda}$ is transformed into corresponding tristimulus values X, Y, and Z using the CIE colour matching functions $\bar{x}_\lambda$, $\bar{y}_\lambda$, and $\bar{z}_\lambda$ which are tabulated in Table B.1),

$$\begin{aligned} X &= \int_0^\infty I_{N\lambda}\bar{x}_\lambda d\lambda, \\ Y &= \int_0^\infty I_{N\lambda}\bar{y}_\lambda d\lambda, \\ Z &= \int_0^\infty I_{N\lambda}\bar{z}_\lambda d\lambda. \end{aligned} \tag{3.4}$$

These tristimulus values are then used to compute the chromaticity coordinates x and y (and the relative brightness $X + Y + Z$) for specifying a colour,

$$x = \frac{X}{X+Y+Z}, \tag{3.5}$$

$$y = \frac{Y}{X+Y+Z}. \tag{3.6}$$

The locus of the calculated chromaticity coordinates for light reflected from smectic 8CB films, for varying film thickness, is shown on the standard CIE chromaticity diagram in Figure 3.6. For films thinner than about 25 molecular layers, the calculation indicates that films appear dark gray, becoming brighter as the thickness is increased. The film then passes through a sequence of colours as the thickness increased further, appearing yellow, then orange, red, purple, blue, yellow, orange, red, blue, green, yellow and so on. The first two colour loops, corresponding to films thinner than about 150 layers, are sufficiently different to be distinguishable by eye with experience.

The thickness of smectic films does not vary continuously, but in steps of one molecular layer. A step in film thickness of a single molecular layer corresponds to a discontinuous change in film colour, which is easily visible for films between 20 and 150 layers. With some practice, the thickness of films

in the range between 45 and 65 molecular layers thick can be determined to an accuracy of ±2 layers simply from their colour.

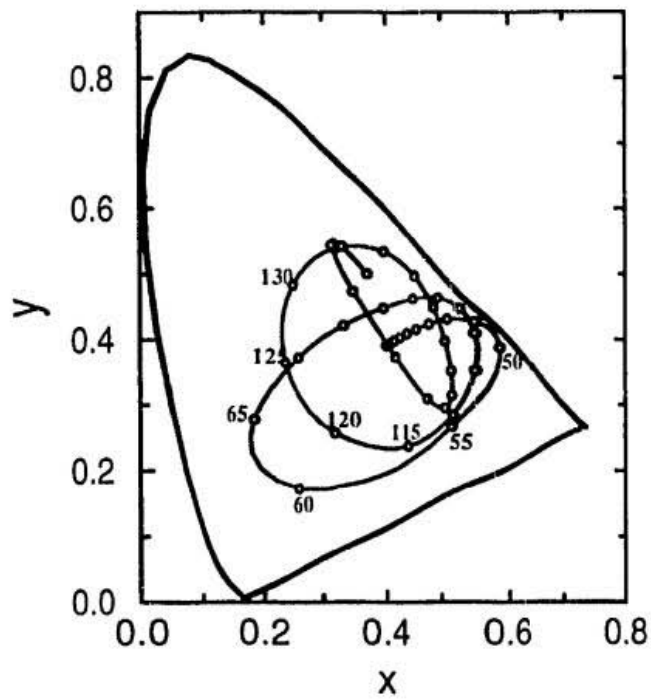

Figure 3.6: Chromaticity of an 8CB film illuminated by a CIE standard source A at normal incidence. The complicated curve shows how the chromaticity changes with film thickness, with the numbers indicating the thickness in molecular layers.

As described in last section, the thickness is also determined by directly measuring the reflected intensity of a polarized monochromatic laser beam. The intensity measurement and the colour measurement are used concurrently in all experiments. Together these two techniques permit exact de-

termination of film thickness for films thinner than 15 molecular layers. For films between 16 and 30 layers the uncertainty is ±1 layer, and for films between 31 and 75 layers the uncertainty is ±2 layers. In the experiments reported in this thesis, the film thickness is between 2 and 75 molecular layers. The calculated reflectivity as a function of film thickness and the calculated chromaticity coordinates for films with thickness smaller than 75 molecular layers are plotted in Figures 3.7 and 3.8 respectively. These two plots are used for direct comparison with the reflectivity and colour measurements.

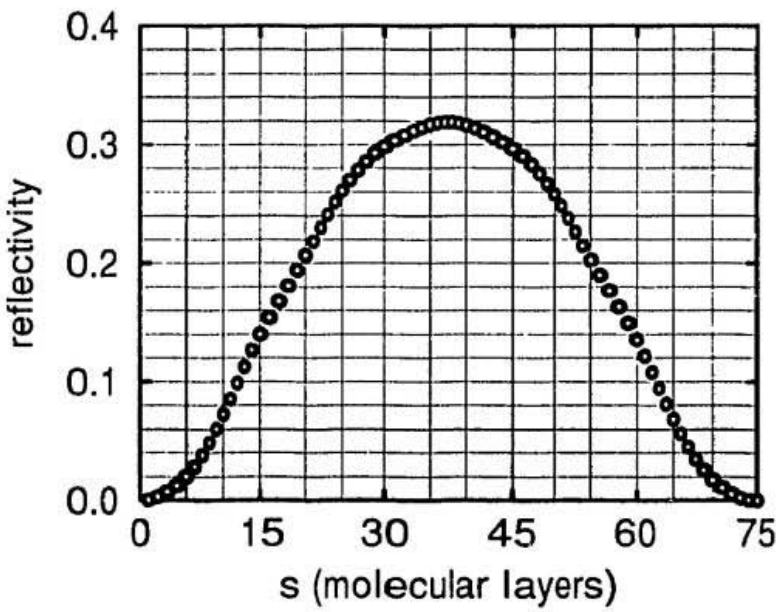

Figure 3.7: Calculated reflectivity for 8CB films up to 75 molecular layers in thickness.

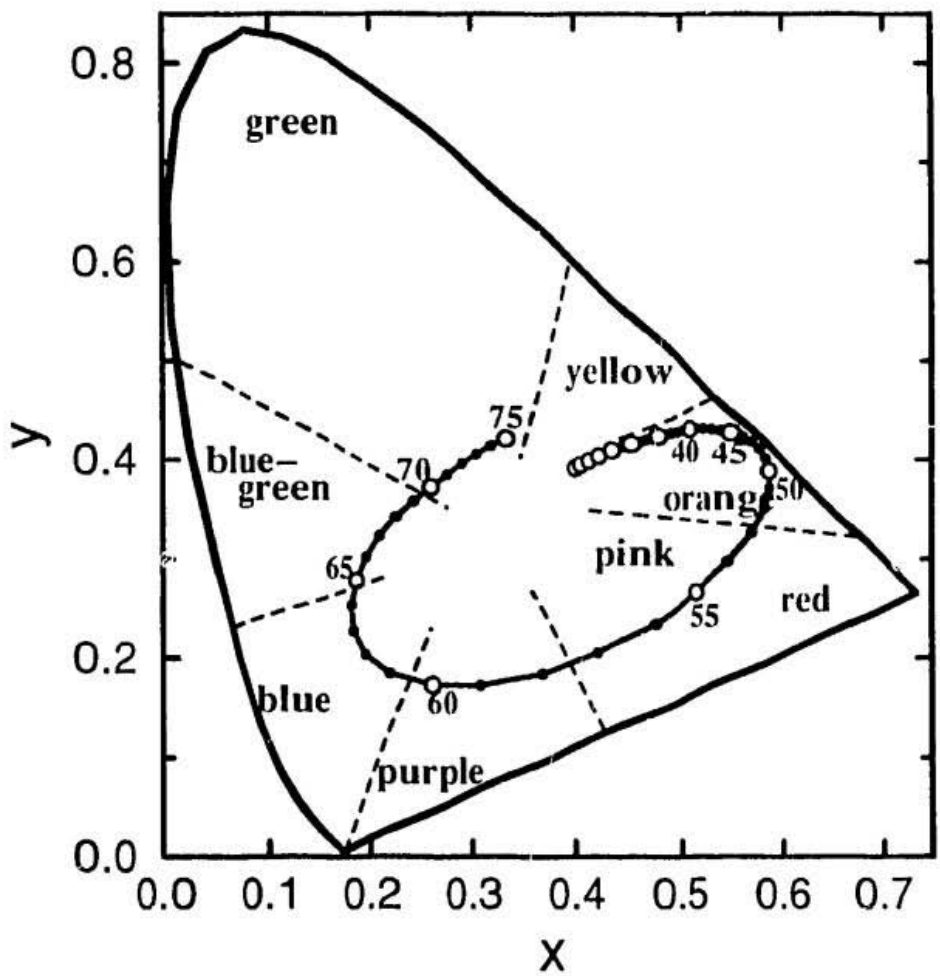

Figure 3.8: Chromaticity of 8CB up to 75 molecular layers thick, illuminated by a CIE standard source A at normal incidence. The numbers indicate the film thickness in molecular layers.

3.3 Flow Visualization

Colour variations across a nonuniform film allow a simple method of flow visualization. Convection in such a film causes a spectacular swirling of colours as the regions of different thickness are advected with flow. However, observations of advected colour variations provide only qualitative information about the convection since, as mentioned before, the flow phenomena depend on thickness. All quantitative measurements are performed using films of uniform thickness. For a completely uniform film viewed in reflected white light, the appearance of the film alone gives no indication of any flow. However, the flow can be visualized by the motion of small particles suspended on the film and advected by the flow [128].

Of the several different flow visualization particles tested, incense smoke particles were found to give the best results. A small amount of smoke is admitted into the experimental housing, and some of the smoke particles settle on the film and are advected by the flow. Flow is visualized by shining a collimated beam of white light onto the film from below. To avoid very strong background illumination, the beam is directed at a small angle away from the vertical. The light scattered by the small smoke particles is readily visible with the microscope described before. In some of the flow velocity measurements, a HMS Model 230 light beam chopper, synchronized with the video camera, is used.

The illuminated particles moving with the flow were imaged by the video camera at a rate of 30 video frames per second. Particle trajectories can be extracted from the video by projecting the recorded images frame by frame onto the screen of a computer terminal. The particle coordinates are determined by finding the pixel position of the particle on the screen, which were then entered into a data file on which analysis is performed.

The velocity of the flow at a given position is assumed to be equal to

the instantaneous velocity of the particle at that position. It is determined approximately by subtracting the position coordinates of a given particle in consecutive video frames, and dividing by appropriate time interval. The flow field at a certain instant can then be obtained from the velocities of many particles scattered over the film.

Continuous play of the video record of a run allows direct visualization of the streamlines of the flow. For a time-independent convection state, the separatrices between neighbouring vortices could be readily located on the screen, allowing the vortex size and the wavelength of the pattern to be determined.

Chapter 4

Experimental Results

Overview

In this chapter, we present measurements of two-dimensional electroconvection and discuss our results in terms of the Ginzburg-Landau model. In section 4.1, measurements of the onset voltage as a function of film thickness, and of the pattern wavelength and flow velocity near the convective onset, are presented. In section 4.2, we present measurements of the wavelength and amplitude of the convection pattern above onset, and discuss the evolution of the pattern towards a stable convection state. The characteristic length scale ξ_0 is obtained from measurements of the pattern amplitude along the length of the film, and the characteristic time scale τ_0 is determined by monitoring the time evolution of the convection amplitude after the applied voltage is raised from below to above threshold. In section 4.3, we present the results of experiments on wavelength selection, and the range of stable wave numbers for the one-dimensional convection pattern is determined. In section 4.4, the results presented above are discussed in terms of the Ginzburg-Landau model. We first summarize those results that are in agreement with the predictions of the Ginzburg-Landau amplitude equation, then discuss the wavelength selection mechanisms possible in a one-dimensional pattern forming system. Our results are consistent with a boundary-induced wavelength selection mechanism proposed by Cross et al. [55].

4.1 Onset of Convection

4.1.1 The Onset Voltage

Observation reveals that a critical applied voltage must be exceeded before convection begins. This onset voltage V_c is determined by observing the motion of flow visualization particles as the magnitude of the applied field is slowly increased or decreased. V_c is taken to be the voltage at which the flow organizes itself into a pattern of vortices throughout the entire length of the film. A voltage of $\pm V$ is maintained on each of the two electrode wires so the voltage V_c is half of the potential difference between the two electrodes at the onset of convection. Within the measurement uncertainties, the threshold voltage is the same when the voltage is slowly increased or slowly decreased.

Figure 4.1 shows how V_c varies with the film thicknesses, given as the number of molecular layers. The data points represent an average over several measurements in films of the same dimension and thickness. Data from films with length 20.0 mm and width 2.0 mm are given in Figure 4.1. For small thickness the data look linear, but beyond about 25 layers the thickness measurements fall below the extrapolation of the thin film data. Figure 4.2 shows three sets of data for thin films of different aspect ratio. They extend to very small s and overlap well within experimental errors. A linear fit to all three sets yields

$$V_c = (0.54 \pm 0.02)s - (0.06 \pm 0.08). \tag{4.1}$$

The intercept at the vanishing film thickness is equal to zero within experimental uncertainties. The data in Figure 4.2 do not show any dependence on film width.

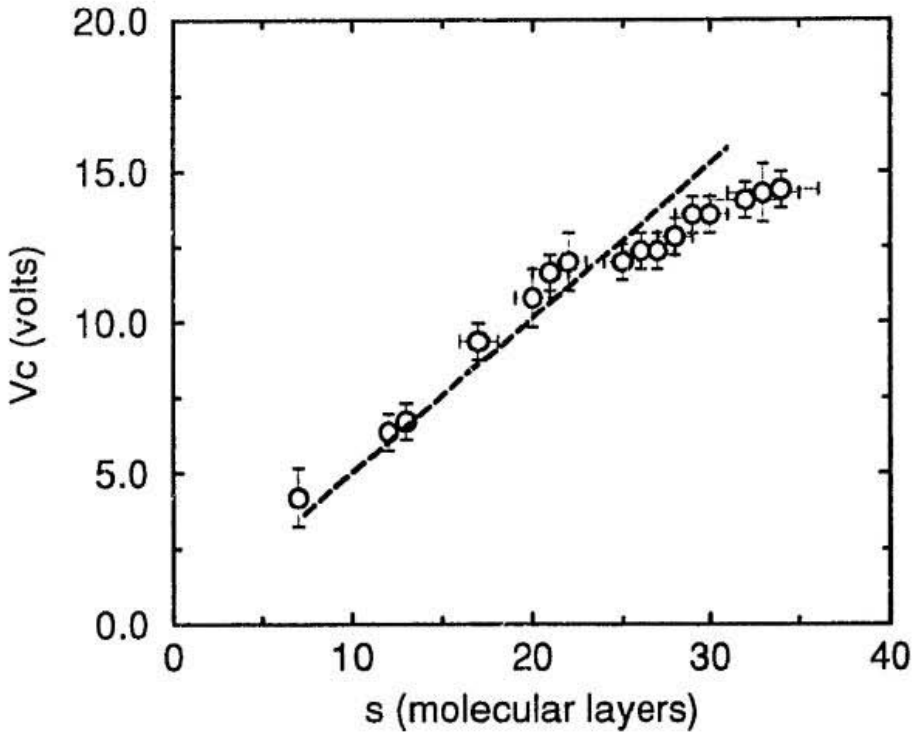

Figure 4.1: Thickness dependence of the onset voltage for electroconvection in films with length 20.0 mm and width 2.0 mm.

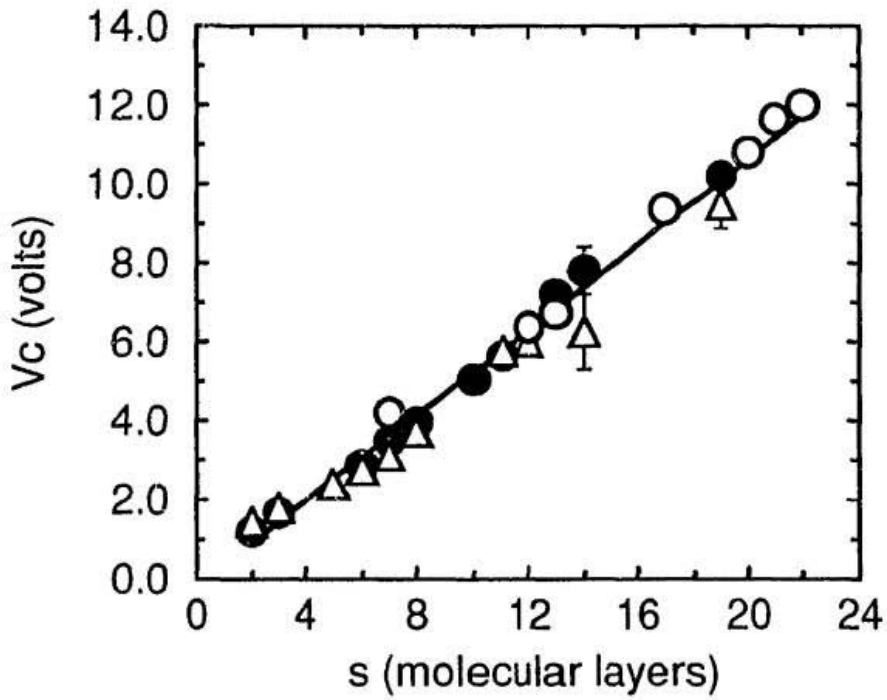

Figure 4.2: Onset voltage as a function of film thickness for very thin films. The data are from experiments on films of three different sizes: 10.0 mm × 0.7 mm (solid circles), 20.0 mm × 2.0 mm (open circles), and 15.0 mm × 1.0 mm (open triangles). The solid line is a linear fit to all of the data.

4.1.2 The Onset Wavelength

The wavelength λ of the pattern can be determined simply by counting the number of vortex pairs along the film. Due to the finite length of the film, λ is quantized, since there must be an integer number of vortices along the length of the film.

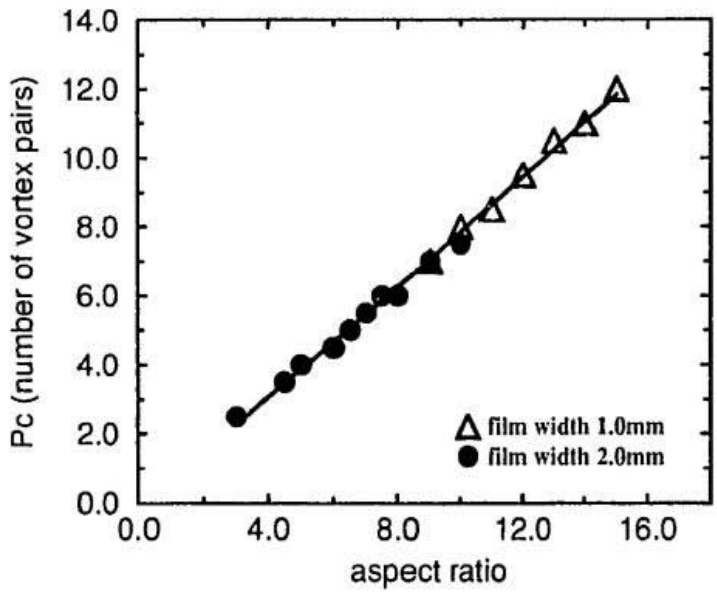

Figure 4.3: Number of vortex pairs as a function of aspect ratio at the convective onset. The open triangles are from experiments on films of width 1.0 mm, and the solid circles on films of width 2.0 mm. The solid line is a linear fit to both sets of data.

For a regular pattern containing N vortices, or P pairs where $P = N/2$, the average dimensional wavelength is the length of the film divided by the

number of vortex pairs, $\lambda = l/P$. Because of the quantization condition, the uncertainty in the number of vortices N is roughly 1/4, and the uncertainty in λ is therefore $\pm\lambda/4N$.

Figure 4.3 shows the number of vortex pairs in the pattern at onset, P_c, as a function of aspect ratio $\Gamma = l/d$. The thickness of the films in Figure 4.3 varies from 2 to 75 molecular layers. A linear fit gives

$$P_c = (0.773 \pm 0.009)\Gamma, \tag{4.2}$$

which describes the data well. The small scatter in the data points originates from the fact that only an integer number of vortices is allowed. Since $\lambda_c = l/P_c$, the reciprocal slope of the linear fit in Figure 4.3 yields the ratio of the onset wavelength λ_c to the film width d, $\lambda_c/d = 1.294 \pm 0.015$. This result is found to be independent of the film thickness and agrees with earlier measurements by Morris et al. [134].

4.1.3 The Amplitude close to Onset

Much detailed information on convective patterns can be obtained from measurements of the flow velocity. In our experimental geometry (see Figure 1.4), the x axis is directed along the long dimension of the liquid film, and the y axis is directed across the width of the film. The origin is set at one horizontal film boundary, so that the two electrodes are at $y = 0$ and $y = d$ respectively.

Velocity Profile

Detailed measurements of the two-dimensional velocity field were carried out by Morris et al. in a setup slightly different from ours [134]. We have measured the horizontal component of the flow velocity, v_x, as a function of x and y close to onset, and our results are consistent with those of Morris et al. [134]. v_x is plotted as a function of position over a pair of vortices in

Figure 4.4. v_x is measured at scattered locations in the interior of the film, at $y \simeq d/5$ or $y \simeq 4d/5$, where v_x has its maximum value (see Figure 4.5). The data resemble a simple sinusoidal function, with little harmonic distortion. The solid line in Figure 4.4 is a least squares fit of the experimental data to $a_0 \sin(2\pi x)$, with $a_0 = 3.0$ mm/s. Here x has been normalized by the pattern wavelength. The good agreement with the experimental data indicates that for convection close to onset, the one-dimensional vortex pattern along the length of the film is dominated by a single sinusoidal mode.

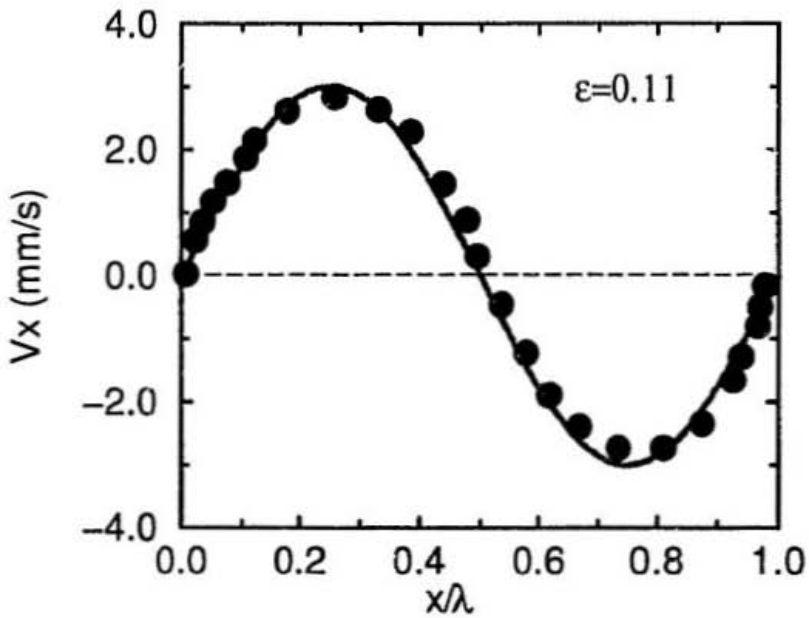

Figure 4.4: The horizontal component of flow velocity as a function of x-position normalized by the pattern wavelength. The range of x covered by the data is far from the lateral sidewalls. The solid curve is a fit of the experimental data to a sine curve.

Generally, a velocity field may be expanded in eigenfunctions which are consistent with the symmetries and the boundary conditions imposed on the flow. Assuming a single Fourier mode for the x-dependence of v_x, as determined from Figure 4.4, the horizontal velocity component can be expressed as

$$v_x(x, y) = v_x^0(y)\sin(2\pi x), \tag{4.3}$$

where $v_x^0(y)$ describes the y-dependence of v_x.

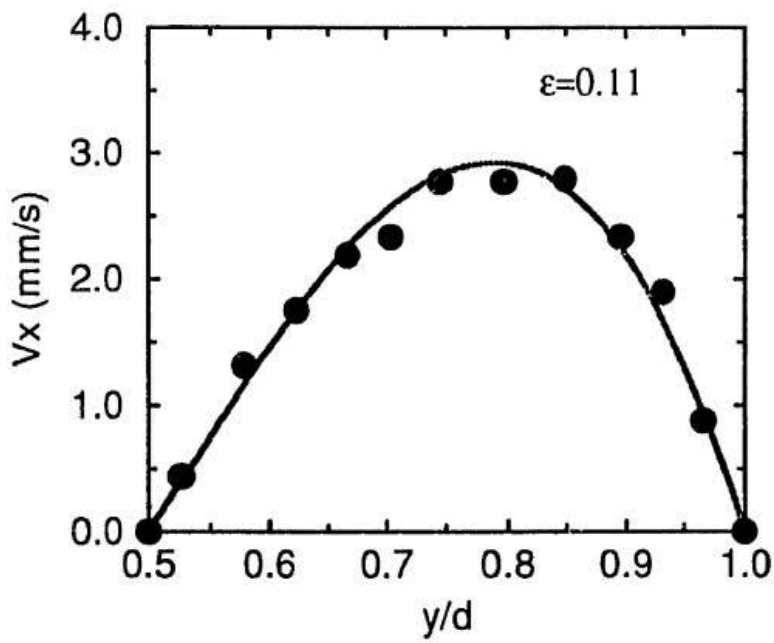

Figure 4.5: The horizontal component of flow velocity as a function of y-position normalized by film width d. The data are taken along a line passing the center of a convection vortex in the interior of the film. The solid curve is a fit of the experimental data to the lowest order Chandrasekhar function S_1.

The y-dependence of the horizontal velocity component has also been determined experimentally along a line passing through the center of a convection vortex and is plotted in Figure 4.5. These data show that v_x vanishes both at the electrodes and at the center of the vortex. This result is consistent with the so-called rigid boundary condition, $v_x = v_y = 0$ for $y = 0$ or $y = d$. From the incompressibility of the two-dimensional liquid,

$$\frac{\partial v_x}{\partial x} + \frac{\partial v_y}{\partial y} = 0, \tag{4.4}$$

one has an additional boundary condition on the velocity derivative at the electrodes, that is, $\partial v_x/\partial x = \partial v_y/\partial y = 0$ for $y = 0$ or $y = d$. These boundary conditions are satisfied by the set of orthogonal functions known as Chandrasekhar functions [48, 134],

$$\begin{aligned} C_m(z) &= \frac{\cosh(\lambda_m z)}{\cosh(\lambda_m/2)} - \frac{\cos(\lambda_m z)}{\cos(\lambda_m/2)}, \\ S_m(z) &= \frac{\sinh(\mu_m z)}{\sinh(\mu_m/2)} - \frac{\sin(\mu_m z)}{\sin(\mu_m/2)}. \end{aligned} \tag{4.5}$$

C_m and S_m vanish at $z = \pm 1/2$, and their derivatives will vanish at these points if λ_m and μ_m are the roots of characteristic equations

$$\begin{aligned} \tanh(\lambda/2) + \tan(\lambda/2) &= 0, \\ \coth(\mu/2) - \cot(\mu/2) &= 0. \end{aligned} \tag{4.6}$$

Provided the spatial distribution of the horizontal velocity component $v_x(x, y)$ is strictly sinusoidal in the x-direction, v_x can then be written [134] as

$$v_x(x, y) = \sum_k B_k S_k(y - \frac{1}{2}) \sin(2\pi x), \tag{4.7}$$

where the position x is normalized by the pattern wavelength and y by the film width d. In Figure 4.5, the full line represents a fit of v_x to the lowest order term in the above expansion in S_k. The fit describes the experimental data well. This suggests that for convection slightly above the threshold, only a single Chandrasekhar mode S_1 is necessary to describe the y-dependence of the flow velocity.

Supercritical Transition

The y component of the flow velocity was measured as a function of applied voltage V in a film of 20.0 mm × 2.0 mm size. The number of vortices or equivalently the wavelength of the pattern does not change over the range of V studied. Figure 4.6 shows the maximum amplitude of v_y, measured at $y \simeq 1/2$ and far from the sidewalls, as a function of ε, where ε is the reduced control parameter given by

$$\varepsilon = \frac{V^2}{V_c^2} - 1. \tag{4.8}$$

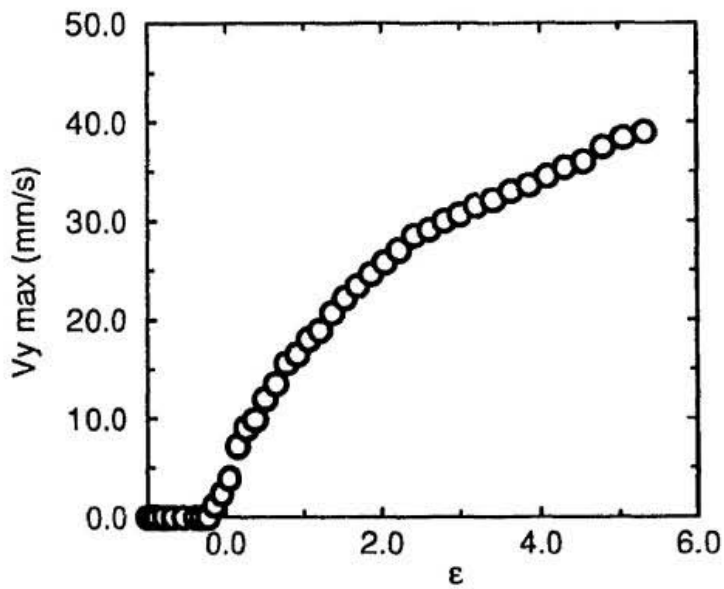

Figure 4.6: The maximum v_y as a function of the dimensionless control parameter ε. $s = 45$ molecular layers.

The data plotted in Figure 4.6 show a transition at which the motionless steady state loses stability to the convecting state. The onset voltage is de-

termined from the film thickness s according to equation (4.1). Figure 4.6 indicates that the amplitude grows continuously from zero. The data above onset are plotted on logarithmic scales in Figure 4.7. The data fall on a straight line with slope 0.50 ± 0.01. The data in Figures 4.6 and 4.7 suggest that the velocity amplitude follows a simple 1/2-power law, $v_y^{max} \sim \varepsilon^{1/2}$, up to $\varepsilon \simeq 5$.

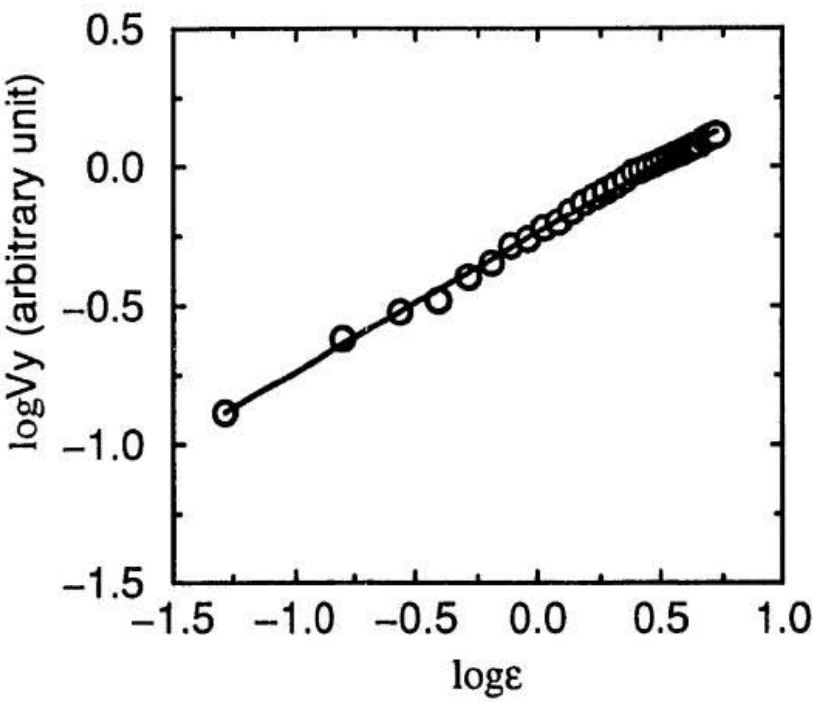

Figure 4.7: The amplitude of v_y as a function of the dimensionless control parameter ε on logarithmic scales. The solid line is a linear fit to the experimental data.

The continuous transition, the 1/2 power law, and the lack of hysteresis are important signatures of a so-called *supercritical* or *forward* bifurcation, analogous to a second order thermodynamic phase transition. These results suggest that the third order Ginzburg-Landau equation (Eq. (1.4)) should give a correct description of the electroconvection pattern close to onset, as in the case of Rayleigh-Bénard convection [22, 23, 63].

4.2 Convection above Onset

4.2.1 Measurements of Convection Wavelength

The electroconvection pattern at onset consists of an array of regular two-dimensional vortices. This pattern persists at slightly supercritical ε. A large number of observations indicates that the pattern wavelength will change as the onset voltage is exceeded. Figure 4.8 shows the pattern wavelength as a function of position at three different values of ε. The length and width of the film are fixed. For each vortex, the wavelength is twice the width of the vortex, normalized by the width of the film d. The position of each vortex is the x-coordinate of the vortex center, normalized by the film length l. The solid circles in Figure 4.8 are data from runs in which the final state is obtained from the motionless state by increasing the voltage from zero. The open circles are from runs in which the final state is obtained by decreasing the voltage from the unsteady convection state.

The mean pattern wavelength for the whole film is shown by the solid lines (for solid circles) or the dashed lines (for open circles). Figure 4.8 illustrates the existence of nonunique wavelengths above the onset of convection. This is particularly apparent from Figure 4.8(b) and (c). The number of vortices in Figure 4.8(b) and (c) is also different for the states reached by the different routes. The wavelength above onset can be either larger or smaller than the onset value λ_c.

Direct observation indicates that vortices adjacent to the sidewalls are usually larger and have slower flow velocities, compared to those far from the sidewalls. The local pattern wavelength has been measured for different lengths l of the film. l is varied by moving one of the sidewalls while the film is convecting at fixed ε. In Figure 4.9, wavelength measurements at two different values of l, with $\varepsilon = 0.3$, are shown. The solid curve in each graph is a fourth order polynomial fit to the experimental data. In the middle of the film, the pattern wavelength is relatively uniform compared with that near

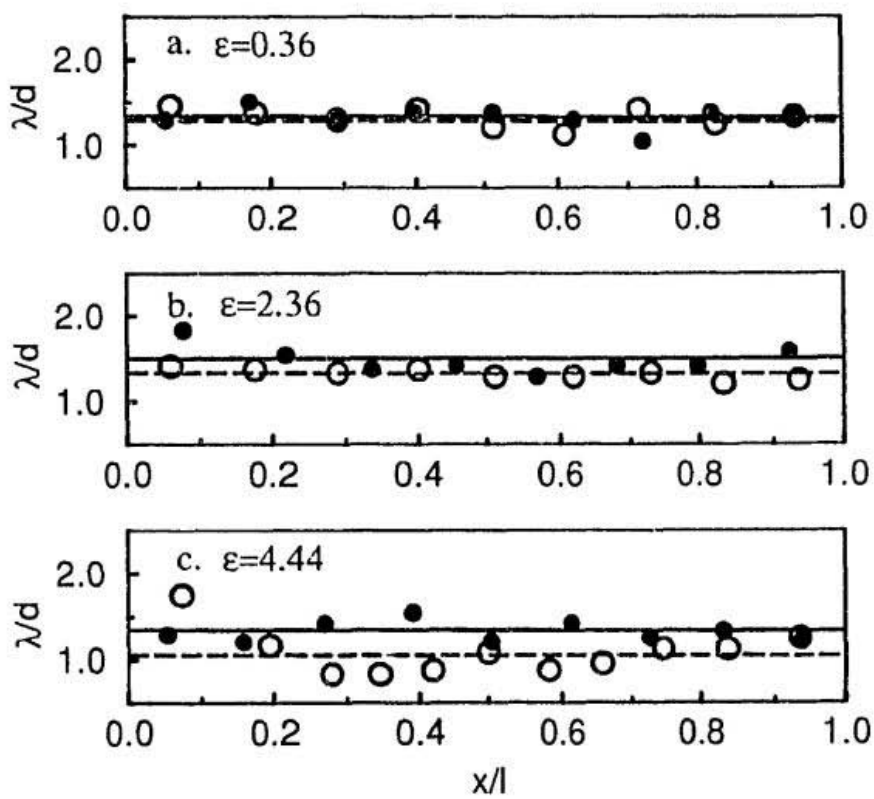

Figure 4.8: Measurements of pattern wavelength at three different supercritical ε as a function of normalized x-position. At each ε, the solid and open circles are data from final convection states reached by increasing the voltage from motionless steady state, and by decreasing the voltage from the unsteady convection state, respectively. The mean pattern wavelengths are shown as either solid lines (corresponding to the solid circles) or the dashed lines (corresponding to the open circles).

the two sidewalls. The vortex adjacent to a sidewall could have a wavelength as large as twice that of a vortex in the center of the film.

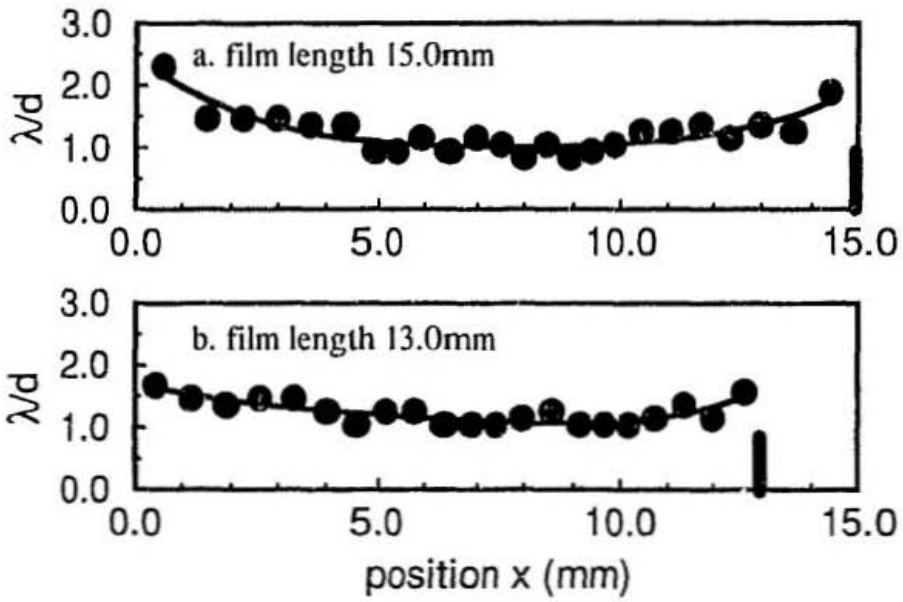

Figure 4.9: Pattern wavelength versus position along the x-axis for films of different length. The solid curves are fits of the experimental data to a fourth order polynomial.

Figure 4.10 gives the combined results of wavelength measurements for eleven films of length 10.0 mm to 15.0 mm. The right sidewall is moved leftward to decrease l from its initial value of 15.0 mm, and the sizes of the vortices are determined after each 0.5 mm change of l. The vortex position has been normalized by the actual film length at each measurement. From Figure 4.10, we see the range of size for vortices adjacent to the sidewall is larger than that in the middle of the film. The sidewalls seem to affect only

the boundary vortices, and do not have a significant influence on the rest of the film.

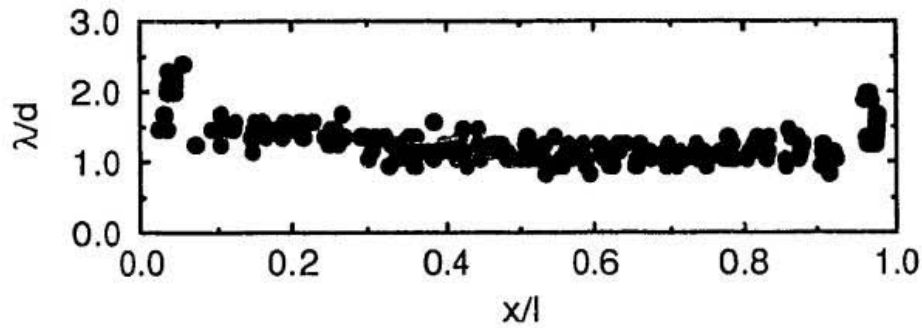

Figure 4.10: Pattern wavelength versus position along the x-axis for eleven films of length 10.0 mm to 15.0 mm. The position has been normalized by the actual film length at each run.

4.2.2 Measurements of Convection Amplitude

In general, viscous friction at the sidewalls damps the flow, resulting in a reduced flow amplitude near the sidewalls. Measurements of flow velocity along the whole length of the film shown in Figure 4.11 and 4.12 indicate that the flow amplitude vanishes at the sidewalls, consistent with the no-slip boundary condition expected to apply at a rigid wall.

Figure 4.11 shows the results of velocity measurements made by tracing the motion of visualization particles at scattered positions throughout the film. The film has dimensions 16.0 mm by 2.0 mm, and the absolute value of the horizontal velocity component $|v_x|$ is measured at $y \simeq d/5$ and $y \simeq 4d/5$. For a lower value of ε (Figure 4.11(a)), the effect of the boundary penetrates well into the center of the film, while for high ε (Figure 4.11(b)), only vortices

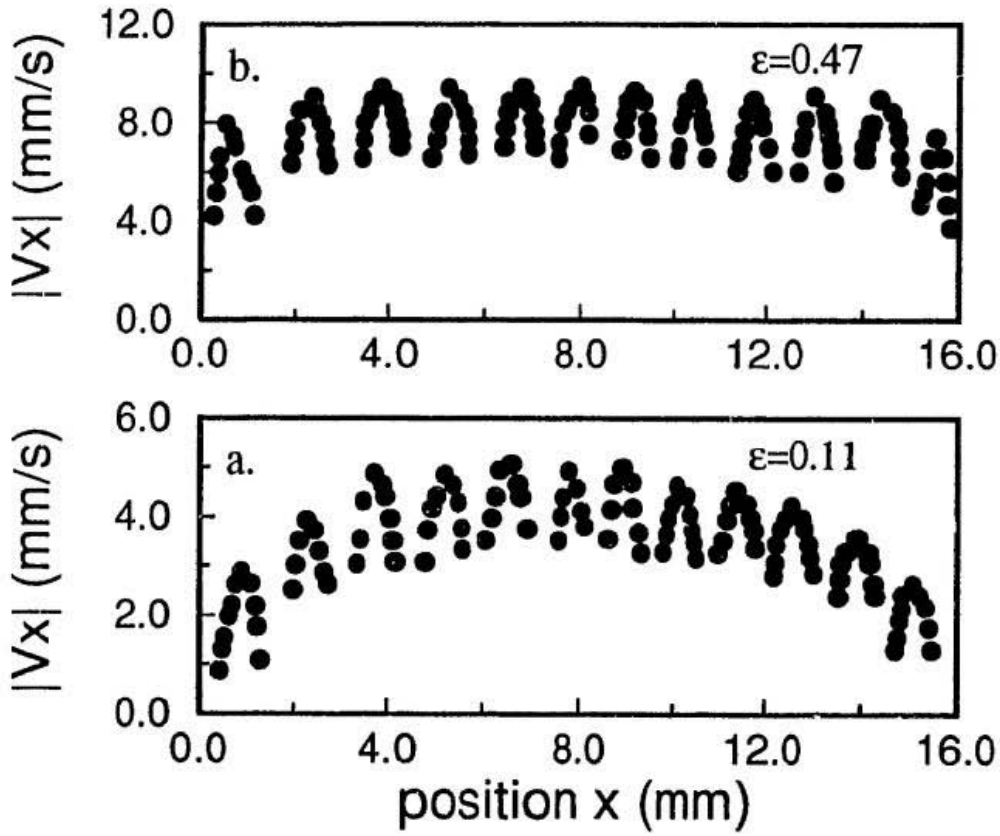

Figure 4.11: Suppression of convection near sidewalls. The solid points show velocity measurements along the length of the film for two different supercritical ε.

adjacent to the lateral boundaries appear to be influenced by the sidewalls.

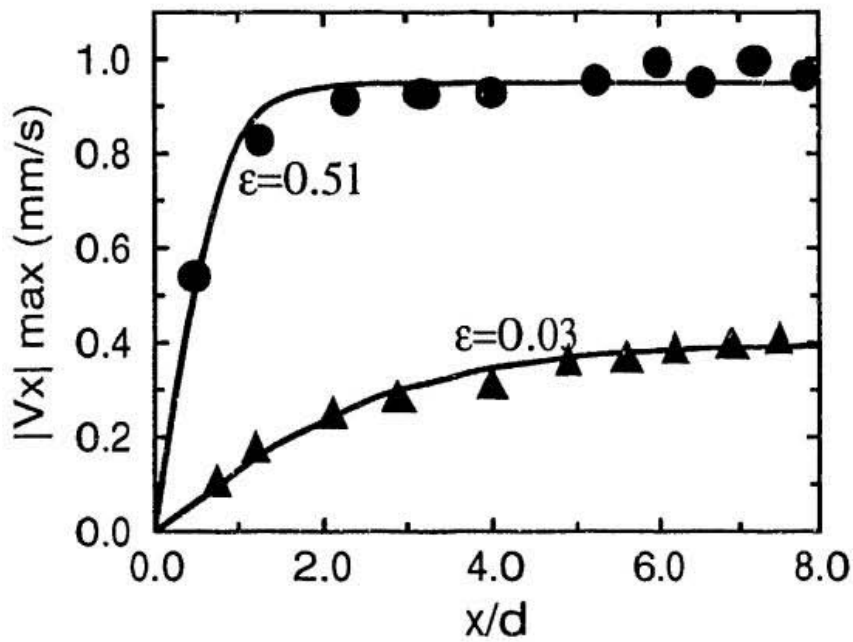

Figure 4.12: The amplitude of electroconvection versus horizontal distance from the sidewall for two values of supercritical ε. Solid curves are fits of the solutions of one-dimensional Ginzburg-Landau equation to experimental data. $s = 3$ molecular layers.

Figure 4.12 gives the envelopes of $|v_x|$ for two different ε as a function of the distance from the sidewall. The film here is 10.0 mm in length and 0.66 mm in width, and the envelope is found from the maximum value of $|v_x|$ for each individual vortex in the film. As before, $|v_x|$ is measured at $y \simeq d/5$ and $y \simeq 4d/5$. The solid curves in Figure 4.12 are fits to the function $C \tanh(x/\sqrt{2}\xi)$ (Eq. (1.12)), with ξ and C adjustable parameters. Here x

is normalized by the film width d, as is the correlation length ξ. The fitting function is the solution of the Ginzburg-Landau amplitude equation when $v_x = 0$ at $x = 0$ is imposed as a boundary condition. Figure 4.12 indicates a good agreement between the experimental data and the prediction based on the amplitude equation.

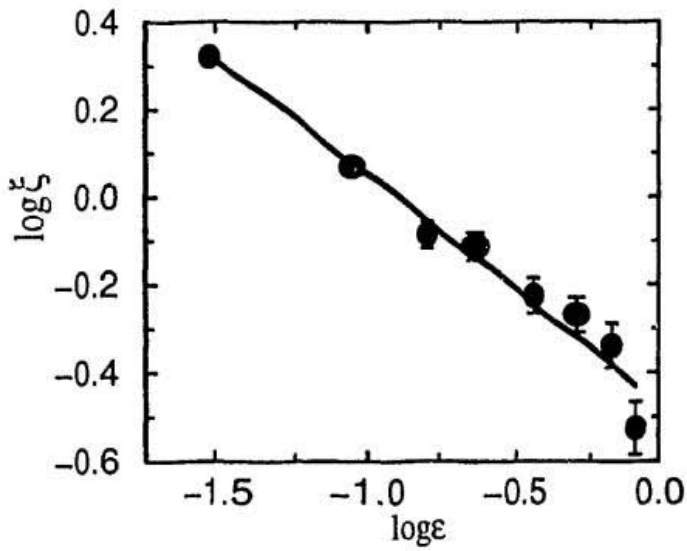

Figure 4.13: Correlation length ξ as a function of ε on logarithmic scales. Each data point is derived by fitting the experimental amplitude at a particular ε to Eq. (1.12). The solid line is a fit of the experimental data to a power law. $s = 3$ molecular layers.

Fits of experimental data at many values of ε to the hyperbolic tangent function given above yield the results for the correlation length ξ given in

Figure 4.13. These data are well described by a power law of the form

$$\xi = (0.34 \pm 0.03)\varepsilon^{-0.52\pm0.04}. \tag{4.9}$$

This is consistent with the prediction from the amplitude equation that $\xi = \xi_0\varepsilon^{-1/2}$, and gives an experimental value for the characteristic length scale for variations in the electroconvection pattern: $\xi_0 = 0.34 \pm 0.03$.

4.2.3 Evolution Towards a Stable State

The amplitude measurements presented in section 4.2 were made on a time-independent steady state pattern. It is also interesting to consider the dynamics of the pattern amplitude as the system evolves towards a steady state.

Measurements of the velocity amplitude as a function of time are shown in Figure 4.14. The film is 20 molecular layers thick. The two curves in Figure 4.14 show the growth of the amplitude after a change of ε from zero to $\varepsilon = 0.36$ and to $\varepsilon = 1.78$ respectively. For the larger value of ε, the duration of transient is much less, but the general shape of the growth curve is qualitatively similar. As before, the maximum value of $|v_x|$ is measured in the middle of the film at $y \simeq d/5$ or $y \simeq 4d/5$.

The full lines shown in Figure 4.14 are fits of the solution of the Landau equation, Eq. (1.10), to the experimental data. The amplitude has the form

$$A_0(t) = \left(\frac{C_1 e^{(\frac{2t}{\tau})}}{1 + C_2 e^{(\frac{2t}{\tau})}}\right)^{\frac{1}{2}}, \tag{4.10}$$

where τ, C_1 and C_2 are used as fitting parameters. It can be seen from Figure 4.14 that the amplitude equation describes the experimentally determined time evolution very well. It is interesting to notice that the amplitude in Figure 4.14 cannot be extrapolated exactly to zero at $t = 0$. The non-zero intercept may reflect the fact that the amplitude grows from small

pre-existing fluctuations [87].

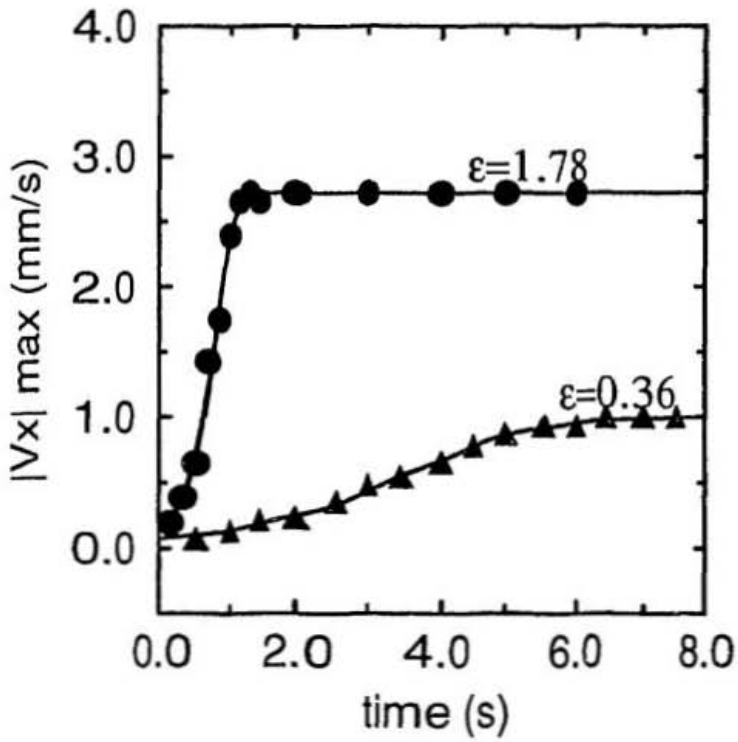

Figure 4.14: Time dependence of the velocity amplitude after a sudden change of applied voltage from zero to a supercritical value. The solid curves are fits of the solutions of the one-dimensional Landau equation to the experimental data. $s = 20$ molecular layers.

The values of τ obtained from a number of curves like those in Figure 4.14 are plotted as a function of the final value of ε in Figure 4.15. A least squares fit to these points yields the relation

$$\tau^{-1} = (1.95 \pm 0.14)\varepsilon^{1.00\pm0.06}, \tag{4.11}$$

where τ is in seconds. This result is consistent with the theoretical prediction that $\tau \propto \varepsilon^{-1}$, and gives the characteristic time scale for the variation of electroconvective pattern: $\tau_0 = (0.51 \pm 0.04)$ s.

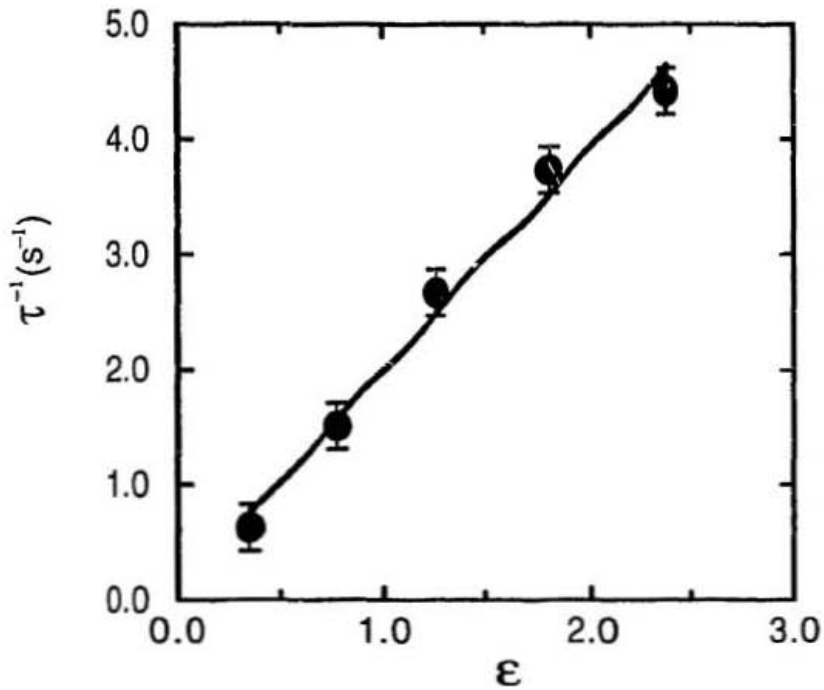

Figure 4.15: The growth rate $1/\tau$ as a function of the final value of ε. The values of τ are obtained from fits such as those shown in Figure 4.14. The solid line is a linear fit to the experimental data. $s = 20$ molecular layers.

4.3 Selection of Pattern Wavelength

4.3.1 Experiments with Varying ε

An important issue in the study of pattern formation is the selection of pattern wave number or wavelength. Typically, the range of wave numbers over which the pattern is stable will be limited to a band of selected wave numbers by various instabilities [56]. For our electroconvection system, observations indicate that convective vortices are always created or destroyed at the sidewalls as the voltage applied across the film is varied to keep the wave number of the pattern within a stable range.

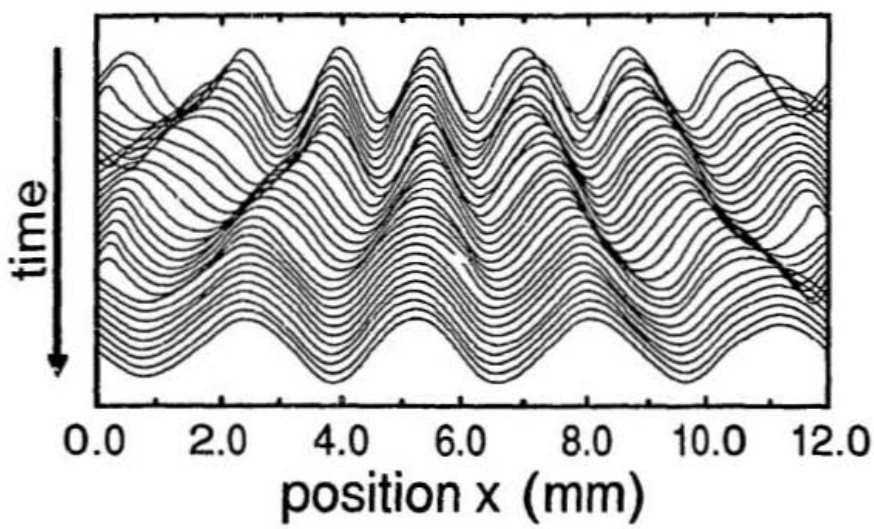

Figure 4.16: Evolution of the pattern in a 12.0 mm × 2.0 mm film following a sudden change in the applied voltage. The lines show v_x along the whole length of the film at thirty equally spaced times immediately after the voltage is reduced.

Figure 4.16 illustrates the evolution of the convection pattern from one stable convection state to another after a change in the applied voltage. The experiment was performed on a film 12.0 mm in length and 2.0 mm in width. The horizontal velocity v_x was measured over the entire length of the film every three seconds from the moment when the applied voltage is suddenly reduced from $\varepsilon = 5.25$ to $\varepsilon = 1.78$. As before, the horizontal velocity is determined at $y \simeq d/5$ or $y \simeq 4d/5$. For each vortex in the pattern, the measured values of v_x are fitted to a sinusoidal function. In Figure 4.16 the fitted curves are plotted for the whole film for each time during the evolution process.

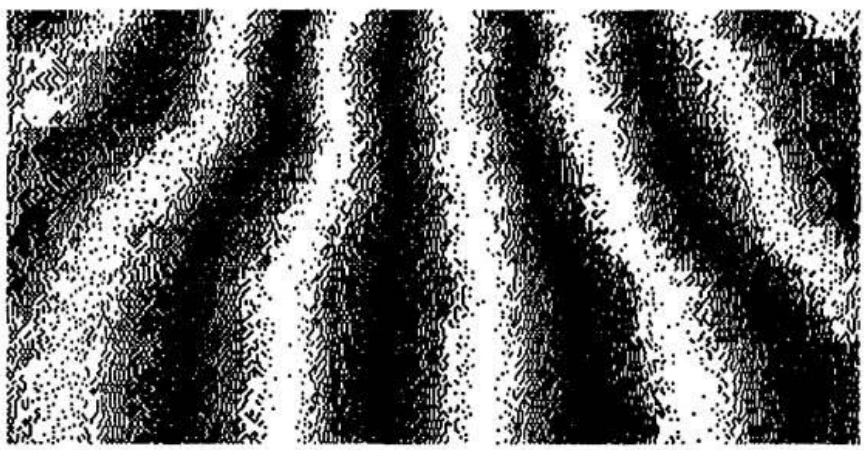

Figure 4.17: A dithered black and white plot of the same process as shown in Figure 4.16. The horizontal coordinate represents position in the film and the vertical axis represents elapsed time. Black corresponds to positive v_x and white to negative v_x.

Figure 4.16 shows the pattern changing from a stable 14-vortex state to an 8-vortex state, after the applied voltage is suddenly reduced. Wavelength adjustment takes place through the creation or loss of vortices at the ends

of the film, not in its interior. A dithered black and white plot of the pattern evolution is given in Figure 4.17, in which the horizontal coordinate represents position in the film and the vertical axis represents elapsed time. The darkness level gives the horizontal velocity. The adjustment of the pattern at the lateral boundaries is shown clearly in this spatial-temporal graph.

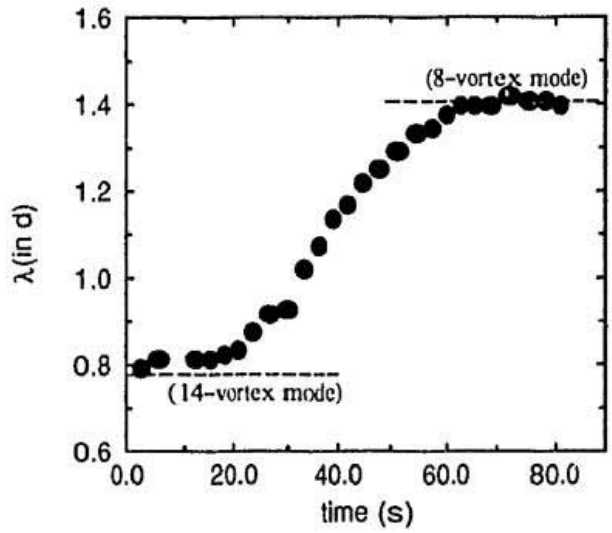

Figure 4.18: Variation of mean pattern wavelength with time at fixed aspect ratio following a sudden reduction in applied voltage. The pattern changes from a 14-vortex mode to an 8-vortex mode final state.

The average wavelength of the pattern as it evolves from the 14-vortex state to 8-vortex state is plotted in Figure 4.18. In making such measurements, the vortices nearest the rigid sidewalls are excluded to minimize the effects due to the adjustment at the lateral boundary. Similar curves were found for all cases studied, independent of the initial and final convection states.

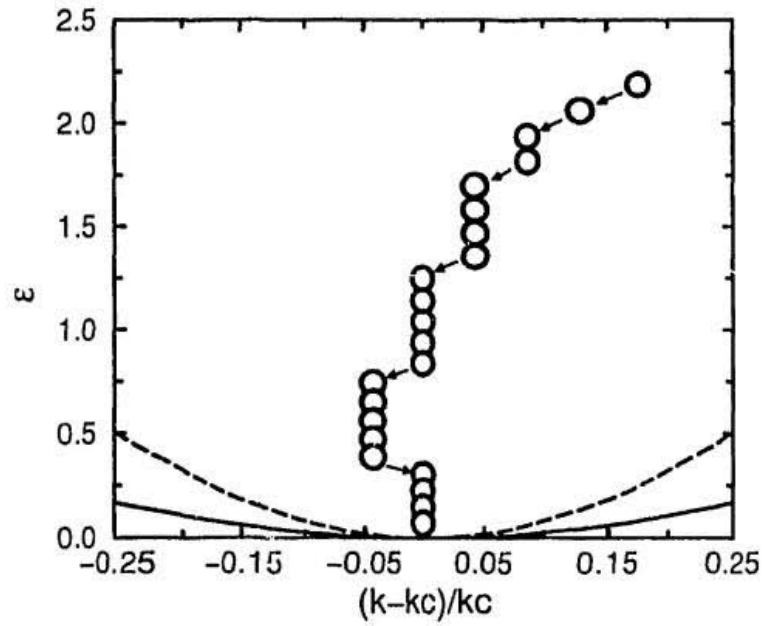

Figure 4.19: The pattern wave number measured as the voltage is decreased step by step from a state above onset. The wave number has been normalized by its onset value. The solid and dashed curves are the marginal and Eckhaus stability boundaries calculated from the experimentally determined value of ξ_0.

By varying the voltage applied across a film of fixed length, the range of stable wave numbers for the steady convective state can be determined. A stable convection pattern is first prepared by increasing the applied voltage from zero to a chosen value above the onset of convection. Patterns with wave numbers k close to $k_c = 2\pi/\lambda_c$ are easily obtained by increasing V slowly through the onset. A sudden jump of voltage from zero to substan-

tially above threshold usually results in a pattern with k different from k_c. Then the voltage is increased or decreased in small steps and the flow pattern monitored. Figure 4.19 shows how k changes as the voltage is decreased step by step from a particular initial state. In this graph, and in those following, the solid and dashed curves are the marginal and the Eckhaus stability boundaries calculated from the amplitude equation with $\xi_0/d = 0.34$ and $\lambda_c/d = 1.294$, as determined experimentally.

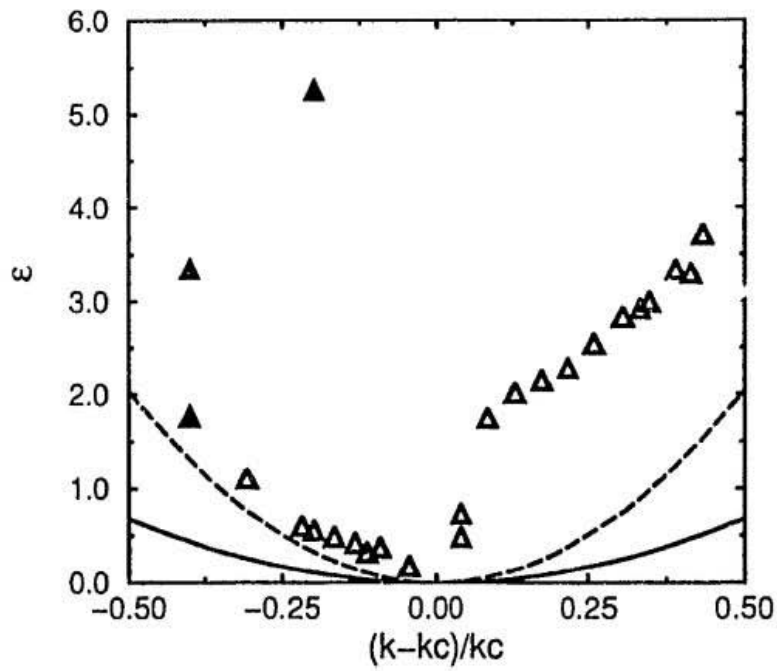

Figure 4.20: Stability range of steady electroconvection patterns measured by increasing (solid triangles) or decreasing (open triangles) the applied voltage. The solid and dashed curves are as in Figure 4.19.

The step size in ε is roughly 0.05 to 0.1, which thus represents the experimental resolution of the stability boundary with respect to ε. Typically, varying the voltage eventually leads to a wave number adjustment through either the creation or the loss of a vortex, which always occurs at the ends of the film, as shown in Figure 4.16. About 50 too 100 vortex turnover times are required for the system to equilibrate after a change in V.

Figure 4.20 shows the stability range of the steady vortex pattern measured by varying the voltage across the film at fixed length. Data from thirty-six runs, using films with thickness between 2 and 45 layers, and with aspect ratios Γ in the range $3 < \Gamma < 15$, have been combined to produce the stability boundary in Figure 4.20. The data shown represent the maximum and minimum values of ε at which a given wave number state is observed. For some films, wave number changes occur inside the plotted boundary. This may be due to differences in end conditions in different runs. No systematic variation in the position of the boundary with either film thickness or aspect ratio is detected.

4.3.2 Experiments with Varying Γ

Measurements of the range of stable wave numbers for steady convective states have also been performed by varying the length of the film at constant applied voltage. After a stable pattern is prepared, the film length is changed by slowly moving the motorized wiper at a speed of about 20μm/s. The thickness of the two-dimensional liquid film does not change throughout the experiment. When the film length l is increased or decreased, a stretching (for increasing l) or a compression (for decreasing l) of the vortex pattern results, followed by the creation or loss of one or more vortices when the wave number k reaches the stability boundary. As before, the creation or loss of vortices usually occurs at the ends of the film.

Figure 4.21 shows the wavelength λ of the pattern in two experiments in

which the film length was varied by moving the end wiper.

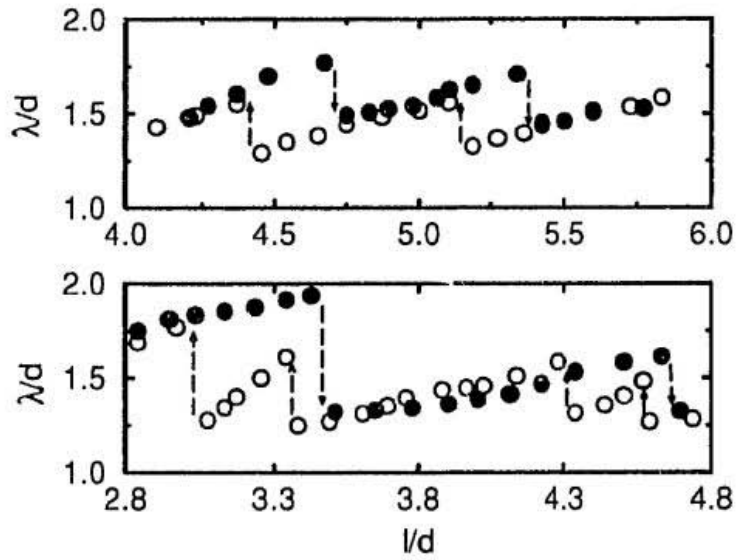

Figure 4.21: Pattern wavelength as a function of film length l, as l is varied. The wavelength plotted is the mean over the pattern, excluding vortices at the ends of the film. The solid and open circles are obtained by increasing and decreasing l, respectively. Arrows indicate wavelength changes caused by the creation or loss of vortices. Upper plot: $s = 50$ layers, $\varepsilon = 1.0$. Single vortices are gained or lost at the arrows. Lower plot: $s = 25$ layers, $\varepsilon = 3.0$. Two vortices are gained simultaneously at the downward arrows; they are lost one-at-a-time at the upward arrows.

As l is increased (solid circles), λ increases to accommodate the change in length at fixed number of vortices. Eventually λ reaches a value above which the pattern is unstable. At this point one or more new vortices form at the end of the film, and the mean wavelength of the pattern decreases back to a stable value. When the film length is decreased (open circles) the opposite

process occurs, with a vortex disappearing at the end of the film when Λ decreases below a stability boundary. The appearance and disappearance of vortices is always hysteretic so that it is possible to observe two or more different states for the same value of l. In Figure 4.21 the downward arrows indicate abrupt transitions from one wavelength to a smaller one which occur with increasing l, and the upward arrows show transitions which occur with decreasing l.

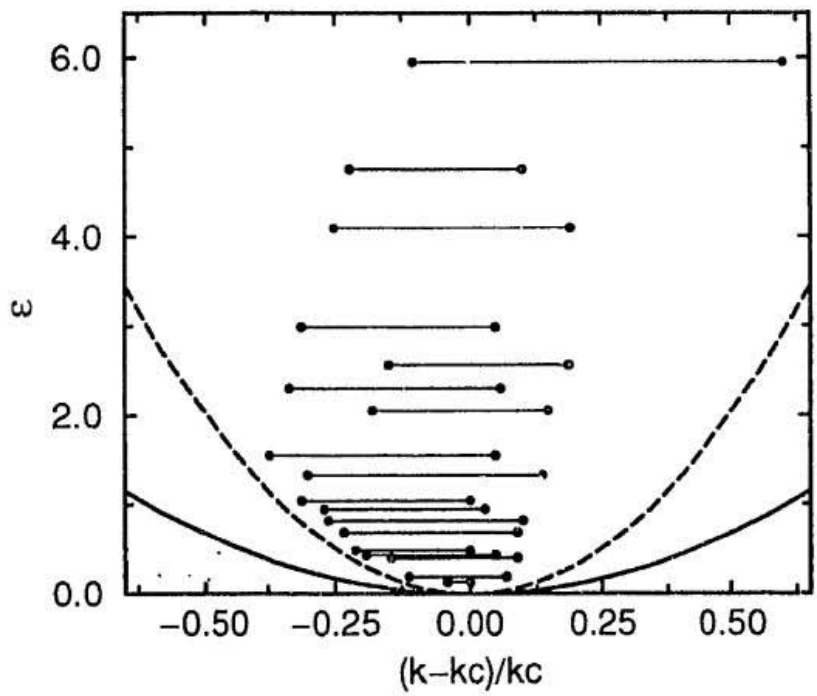

Figure 4.22: Stability boundary determined by varying the film length at constant applied voltage. The experimentally determined stability range for a given ε is represented by two solid circles connected by a horizontal line. The solid and dashed curves are as in Figure 4.19.

The range of stable wave numbers obtained from data such as that in Figure 4.21 is summarized in Figure 4.22 in the form of solid circles connected by horizontal lines. The onset wavelength $\lambda_c = 1.294d$ is used to determine k_c in this figure. Data from films having s between 3 and 65 layers and $3 < \Gamma < 15$ are shown. Again there are no systematic variations in the boundary with either film thickness or aspect ratio.

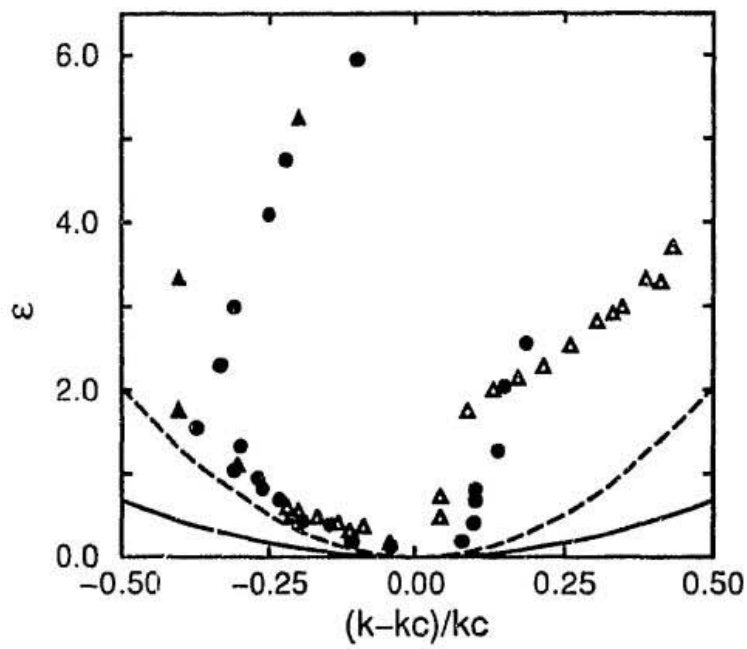

Figure 4.23: Superimposed plot of the stability boundaries measured by varying ε at fixed l and by varying l at fixed ε. The triangles and circles are as in Figure 4.20 and 4.22 respectively, the solid and dashed curves are as in Figure 4.19.

The stability boundaries measured with the two techniques[1] described above are shown superimposed in Figure 4.23. They are consistent in their general shape over the whole range of measurements and appear to lie inside the boundary for the bulk Eckhaus instability, shown by the dashed curve.

[1]Techniques analogous to ours were used [42, 62] to measure the stability boundary of Taylor-Couette flow [60]; they observed the creation or loss of Taylor vortex pairs in the interior of the system, and their measured stability boundary was in quantitative agreement with the calculated Eckhaus stability boundary [164].

4.4 Discussions

4.4.1 Critical Behaviour

The Ginzburg-Landau amplitude equation, Eq. (1.4), predicts characteristic mean-field critical effects for length and time scales [56] of a convective system. Our measurements of the velocity profile and convection amplitude close to onset are in agreement with these predictions. Within our experimental uncertainty, the amplitude of the velocity field grows as $\sqrt{\epsilon}$ for $\epsilon > 0$. Figure 4.7 indicates that this 1/2–power law remains valid up to $\epsilon \simeq 5$, even though the amplitude equation is expected to be valid only for small ϵ. Although a similar result was found for Rayleigh-Bénard convection [63], this must be regarded as "a numerical accident" valid only for particular systems [4], and not a general phenomenon.

Our measurements of the suppression of convection near a rigid sidewall at supercritical ϵ showed that the correlation length ξ varies as $\xi = \xi_0 \epsilon^{-1/2}$, also in agreement with the predicted behaviour. According to the Ginzburg-Landau equation, the relaxation time τ of the pattern behaves as $\tau = \tau_0 \epsilon^{-1}$. Measurements of time evolution of the convection amplitude after the applied voltage is raised from below to above threshold confirm this prediction. The divergence of the relaxation time at vanishing ϵ corresponds to the critical slowing down which occurs at a second order thermodynamic phase transition. The excellent agreement between these results and the theoretical predictions indicate that the Ginzburg-Landau amplitude equation can be used to describe the behaviour of the system near the onset of convection, although a derivation of the Ginzburg-Landau equation from the equations of motion for this electroconvection system does not exist at present.

The form of the one-dimensional Ginzburg-Landau equation (Eq. (1.4)) is quite general, and the detailed properties of the individual systems are contained in the real constants ξ_0 and τ_0, which set the characteristic length and time scales of the pattern [56]. These constants can be determined di-

rectly from the prefactors of the above mentioned power law dependences. We find ξ_0 to be equal to $(0.34 \pm 0.03)d$, and the experimental value of τ_0 is 0.51 ± 0.04 second[2], somewhat smaller than the value of $\tau_0 = (20 \pm 4)$ s in thermal convection experiment [201].

4.4.2 Wavelength Selection

There are basically two mechanisms [56, 62] that could play a role in wavelength selection in one-dimensional patterns. The first is the Eckhaus instability, which is a long-wavelength instability of the basic pattern. The second is a boundary-induced instability which is due to the fact that the pattern's amplitude goes to zero at the lateral sidewalls.

For an ideal convective system without lateral boundaries, the band of stable wave numbers is limited by process s which necessarily occur in the interior of the system. The one-dimensional Ginzburg-Landau equation has stable solutions only over the range bounded by the Eckhaus stability boundary. For $\varepsilon > 0$, the Eckhaus stability boundary $k_E(\varepsilon)$ is given by $k_E(\varepsilon) - k_c = (k_m(\varepsilon) - k_c)/\sqrt{3}$ (Eq. (1.3)), where $k_m(\varepsilon)$ is the marginal stability boundary. Both the marginal and Eckhaus stability boundaries are parabolic. According to Eq. (1.14), the correlation length ξ_0 gives the curvature of the marginal stability boundary, and therefore of the Eckhaus boundary (Eq. (1.15)). Using our experimental result for ξ_0, we obtain the Eckhaus stability boundary plotted in Figure 4.24.

For a finite system of fixed length l, solutions of the Ginzburg-Landau equation must satisfy specific lateral boundary conditions. For rigid boundaries, the amplitude of convection is suppressed through viscous effects near the sidewalls, and the appropriate boundary condition is $A(x) = 0$ for $x = 0, l$ [6, 55]. Our measurements of the flow velocity along the entire length of a

[2]since the material parameters of 8CB are not accurately known, we do not attempt to write τ_0 in dimensionless form.

convecting film shown in Figure 4.12 indicate that this boundary condition is consistent with experimental observations in this system.

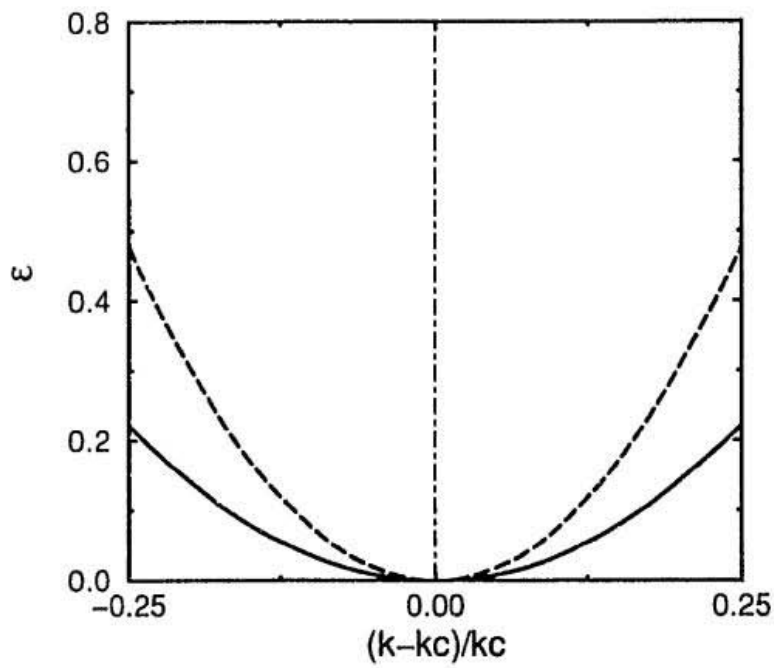

Figure 4.24: The marginal stability boundary (solid curve) and the Eckhaus boundary (dashed curve) for two-dimensional electroconvection.

Cross et al. [54, 55] have shown theoretically that the rigid sidewalls provide a means whereby the wave number in the bulk of the system can adjust its value by the creation or destruction of vortices near the walls, where the amplitude of the pattern is suppressed. In contrast, the Eckhaus instability

normally results in the gain or loss of a pattern unit in the interior of the system. From calculations using the Ginzburg-Landau equation, Cross et al. showed the boundary-induced wavelength selection mechanism gives rise to a range of stable wave numbers much narrower than that allowed by the Eckhaus instability. For the former case [54, 55], they found the width of the band of allowed states to be proportional to ε, while the Eckhaus stable band has a width proportional to $\varepsilon^{1/2}$. The slopes of the boundaries of the stable band depend on the fluid properties as well as the exact nature of the boundary conditions at the sidewalls.

Qualitatively, a restricted band of stable wave numbers due to rigid boundaries has been observed in numerical simulations of the hydrodynamic equations for Rayleigh-Bénard convection [8, 129]. Some hints of this behavior have also been observed in experiments [125]. However, in most experiments, three-dimensional effects are important, and there has been no unambiguous experimental observation of wavelength selection by boundary effects.

The stability boundary obtained from the experiments in which ε is varied is shown in Figure 4.25 for $\varepsilon \leq 2$. The short-dashed lines in this figure are linear fits to the experimental data for $k < k_c$ and $k > k_c$. Both branches of the stability boundary appear linear, that is, $\varepsilon \propto |(k - k_c)/k_c|$. Furthermore, vortices always form or vanish at the ends of the system in our experiments, not in the interior. These results are consistent with what would be expected from the boundary-induced wavelength selection mechanism. The long-dashed curve in Figure 4.25 is the Eckhaus stability boundary calculated using the experimentally determined value of ξ_0. The solid curve is the marginal boundary. As Figure 4.25 shows, the stability range of the convection patterns is restricted to a region well inside the Eckhaus stability boundary.

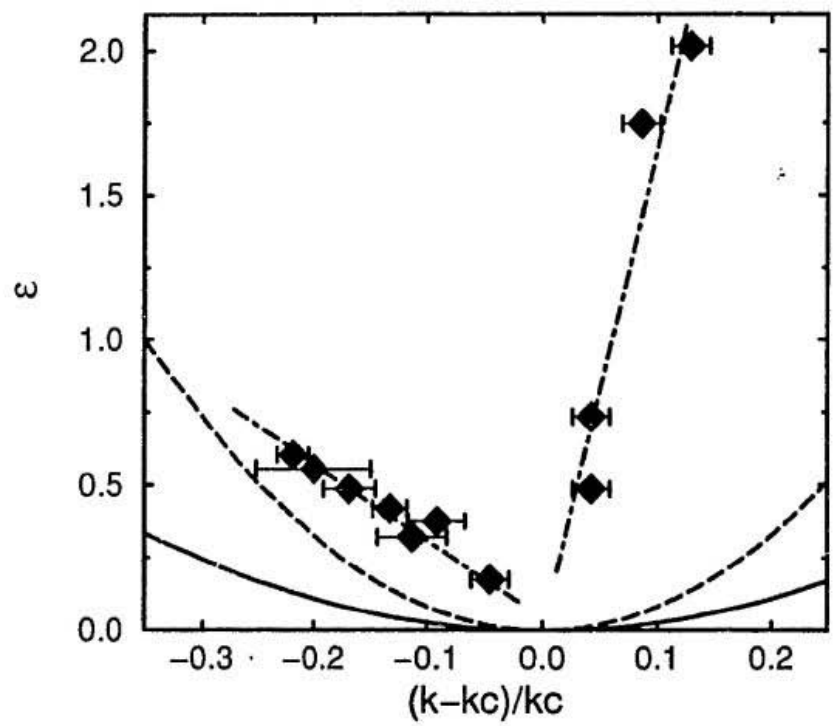

Figure 4.25: Stability boundary for two-dimensional electroconvection close to onset. The two dot-dashed lines are linear fits to the experimental data on each branch, and the solid and dashed curves are the marginal and Eckhaus boundaries respectively.

Chapter 5

Conclusion

Overview

In this chapter, we summarize the results of our experimental study, as well as theoretical development, of one-dimensional pattern formation in a two dimensional electrically driven convective system. A brief discussion of the possible extensions of the current work is also presented.

5.1 Conclusion

In this work, we have presented measurements of one-dimensional electroconvective patterns in a two-dimensional hydrodynamic system composed of freely-suspended smectic-A liquid crystal films. The smectic-A mesophase has a layered structure, and a uniform smectic-A film behaves like a two-dimensional isotropic liquid. In our experiments, films have been made as thin as only two molecular layers thick. As far as we know, this is the first time that hydrodynamic flow has been studied in a substrate-free system [172] so two-dimensional that it has only two molecular layers in the third dimension. We apply a d.c. voltage in the plane of the film, and a one-dimensional convective pattern in the form of an array of counter-rotating vortices develops when the applied voltage exceeds a certain critical value.

Direct observations indicate that a vortex adjacent to each of the lateral sidewalls may form below the onset of electroconvection. With increasing applied voltage, the stable one-dimensional vortex pattern persists up to a certain value, beyond which the flow becomes unsteady. Vortices are created or annihilated far from the lateral boundaries in the unsteady convection regime, but always appear or disappear at the sidewalls close to onset.

We have experimentally determined the dependence on film thickness s of the onset voltage V_c of two-dimensional electroconvection. V_c is linear in thickness for very thin films and we see no apparent dependence of V_c on film width. A linear fit to the data gives $V_c = (0.54 \pm 0.02)s - (0.06 \pm 0.08)$, indicating that V_c goes to zero for zero thickness within experimental uncertainties. The pattern wavelength at the convective onset has also been measured. We find $\lambda_c/d = 1.294 \pm 0.015$, independent of the film thickness. This is consistent with the results of Morris et al. [134].

For convection slightly above threshold, we have determined the spatial dependence of the horizontal velocity component of the convective patterns.

Experimental results suggest that the spatial dependence of $v_x(x,y)$ of the one-dimensional vortex pattern along the length of the film (the x-direction) is dominated by a single sinusoidal mode, whereas the lowest order Chandrasekhar mode S_1 describes the y-dependence of $v_x(x,y)$ well. These results are also consistent with those of Morris et al. [134].

Measurements of the pattern amplitude indicate a supercritical bifurcation at the onset of convection. The amplitude grows as $\sqrt{\varepsilon}$ for $\varepsilon > 0$. Close to onset, our experiments have shown that the correlation length of the pattern varies as $\xi = \xi_0 \varepsilon^{-0.52 \pm 0.04}$. In addition, the relaxation time of the pattern is found to behave as $\tau = \tau_0 \varepsilon^{-1.00 \pm 0.06}$. The experimental values of the exponents are in good agreement with the values of 1/2 and 1 for ξ and τ respectively predicted by the Ginzburg-Landau equation. The constant ξ_0 in one-dimensional Ginzburg-Landau equation is found to be 0.34 ± 0.03, in units of the film width d, and the constant τ_0 for a convecting film 20 molecular layers thick is determined to be 0.51 ± 0.04 s. These results show that the Ginzburg-Landau equation describes the behaviour of our system near onset very well, although it has not yet been shown that the Ginzburg-Landau equation can be derived from the electrohydrodynamic equations of motion for our system.

Above onset, the convection pattern exists over a range of stable wavelengths. Wave number adjustments occur by the creation or destruction of vortices near the sidewalls, and our experiments show that the amplitude of the pattern is suppressed there. Close to threshold, the width of the band of stable wave numbers is found to be proportional to ε, in contrast to what is the case for the Eckhaus instability, for which the width of the band goes as $\varepsilon^{1/2}$. Our experimentally determined stability boundary appears to be narrower than the Eckhaus band determined from the experimental value of ξ. These results suggest that we have observed the one-dimensional boundary-induced wavelength selection process, rather than the long-wavelength Eckhaus instability.

Apart from convection experiments, a set of electrohydrodynamic equations has been presented for the understanding of two-dimensional electroconvection. Without solving the equations, theoretical analysis indicates the normalized control parameter to be $\varepsilon = V^2/V_c^2 - 1$, in agreement with the experimental observations.

In Appendix A, a hydrodynamic model is proposed to describe the flow observed near the sidewalls below the onset of electroconvection. The flow in this model is caused by the electrohydrodynamic shear-stress interaction, which originates from an interfacial charge density distribution at the lateral boundary, rather than by an electric body force. The solution of the hydrodynamic equations in this model gives results in qualitative agreement with the flow observed in experiments.

5.2 Future Work

Because of the extreme two-dimensionality of a freely suspended smectic A film, effects due to three-dimensional flow are inhibited. Therefore this system would be favorable for experiments aimed at making contact with some two-dimensional hydrodynamic theories.

A natural extension of current experiments is the study of convection in unsteady regime. Many aspects of flow evolution observed in other hydrodynamic systems are expected in two-dimensional electroconvection. We give in Figure 5.1 examples of time series [1, 5] of the horizontal velocity component $v_x(t)$ and the corresponding Fourier spectra as ϵ is varied. The measurements were by tracking the motion of passive tracer particles moving with the flow over long periods of time. Detailed experiments would be necessary to identify the transition from steady convection to unsteady flow.

Our system would also be attractive for the study of the transport of passive impurities [44, 159, 160, 175, 181, 213]. In general, the trajectories of individual passive particle are very complex [126], and chaotic trajectories [7, 144] may arise even though the flow field is laminar. Examples of the individual particle trajectories and the corresponding horizontal displacements as a function of time for our system are given in Figure 5.2. In Figure 5.3, an example of the variance[1] $\sigma^2(t)$ of the horizontal particle displacements for flow near the unsteady convection state is shown. A large number of experiments of such kind sould be expected in order to get insight into the nature

[1]The transport of passive impurities can be analyzed as a one-dimensional process in the horizontal direction. The variance (the second moment) of the horizontal particle displacements $\sigma^2(t)$ is calculated by the relation

$$\sigma^2(t) = < (\Delta x(t,\tau) - < \Delta x(t,\tau) >)^2 >, \tag{5.1}$$

with

$$\Delta x(t,\tau) = x(t+\tau) - x(t), \tag{5.2}$$

where $< ... >$ denotes a time average (over τ) over the record.

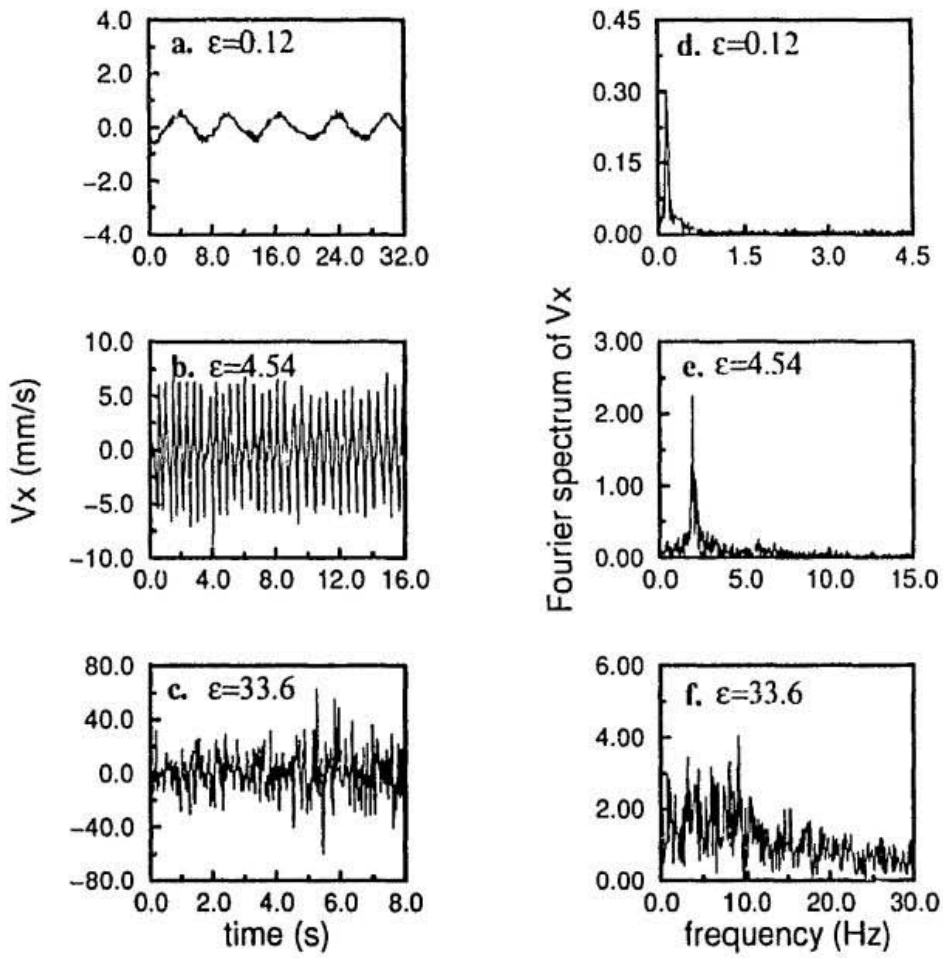

Figure 5.1: Velocity time series (a-c) and Fourier spectra (d-f) obtained from measurements of the horizontal velocity component $v_x(t)$. (a) and (d): $\varepsilon = 0.12$; (b) and (e): $\varepsilon = 4.54$; (c) and (f): $\varepsilon = 33.6$.

of the transport due to the combination of convection and molecular diffusion.

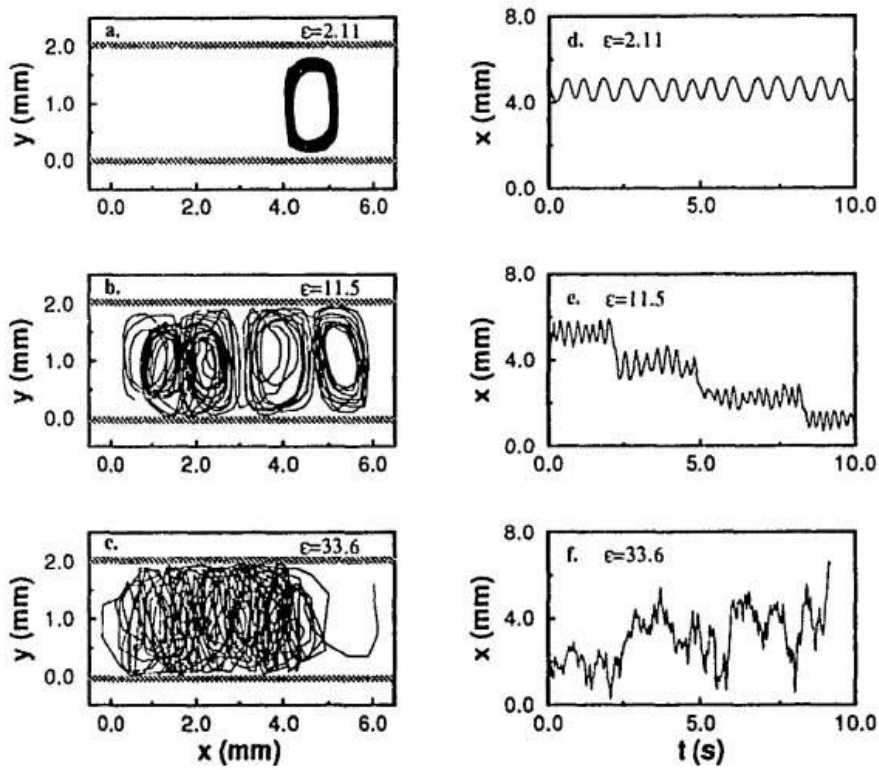

Figure 5.2: Particle trajectories (a-c) and the corresponding horizontal displacements as a function of time (d-f) for various values of ε. $d = 2.0$ mm for all films.

It would be of interest to continue the study on the flow velocity field at very high values of ε. Improved measurement techniques [2, 189, 202, 209] such as a computerized system for particle image velocimetry would be necessary. A comparison of such measurements with established results from three-dimensional Rayleigh-Bénard convection experiments, among others,

would be interesting.

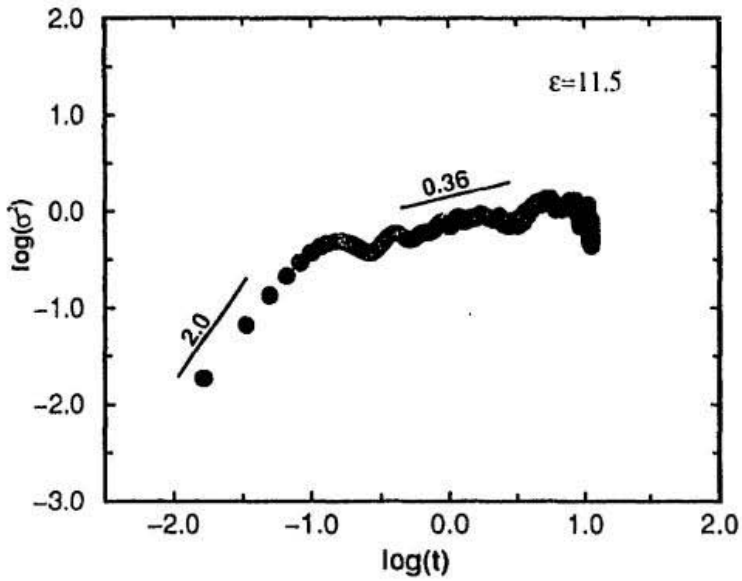

Figure 5.3: The variance of the horizontal particle displacements for the data of Figure 5.2(b).

Another direction for future experiments is a study of the effect of doping level on the onset behaviour of convection. Systematic experiments of this kind could be helpful in testing various models and in elucidating the underlying mechanism for electroconvection in thin system.

The two-dimensionality of the velocity field in a thin film makes computational work on this system attractive. Numerical simulations of two-dimensional electroconvection would be highly valuable.

This type of electroconvection experiment could also be performed on ultrathin films of certain kinds of polymers or bilayers. These experiments might be useful in understanding electric-field-induced transport as well as the significance of surface effects in macromolecular membranes, and which may find applications in biological and materials sciences.

Appendix A

Boundary Vortex Problem

In this appendix, a hydrodynamic model is proposed which describes the flow observed near the lateral sidewalls below the convection onset. The flow in this model originates only from an interfacial charge density distribution at the lateral boundary.

A.1 The Electrohydrodynamic Shear-Stress Interaction

Experimental observations indicate that slow vortices adjacent to each of the two sidewalls may form below the convection onset (Figure A.1(a)), even though there is no flow in the central region of the film. These boundary vortices differ from the flow pattern observed above onset (Figure A.1(b)), which consists of an array of vortices along the entire length of the film. The boundary vortices are also present when ε is reduced from above to below onset.

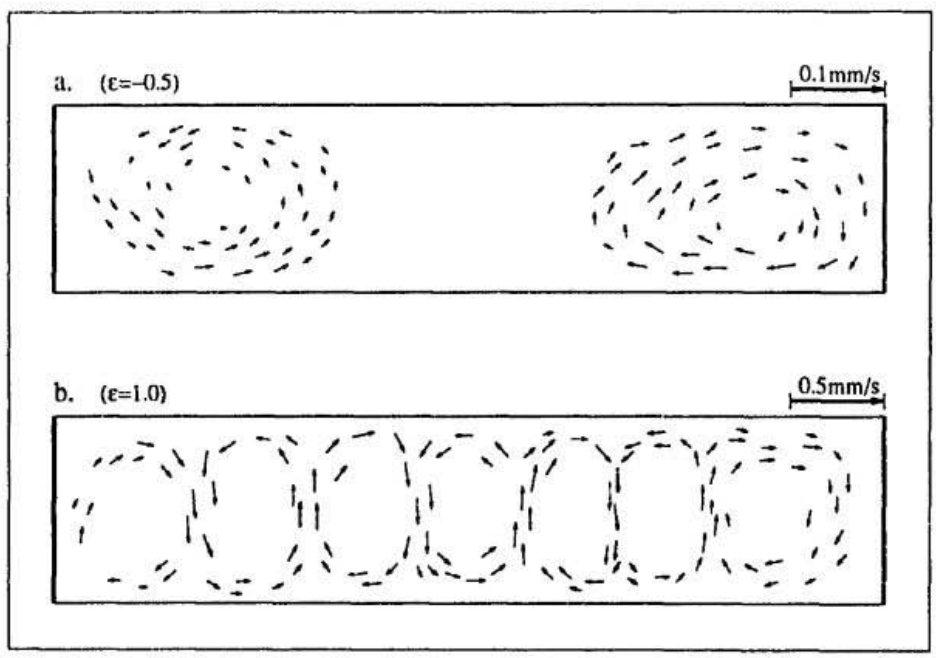

Figure A.1: Vector plots of the flow field measured below (a) and above (b) the convection threshold. $l = 9.0$ mm, $d = 2.0$ mm.

In general, viscous friction at lateral sidewall increases damping and therefore inhibits flow. However, discontinuities in electrical properties at the sidewalls can result in a charge density which could induce a fluid motion. In the following, the boundary vortex observed below the convection onset is explained using a model which shows that the presence of an interfacial charge density at the lateral boundaries can drive vortex flow in a viscous liquid film, even in the absence of space charge in the bulk of the film.

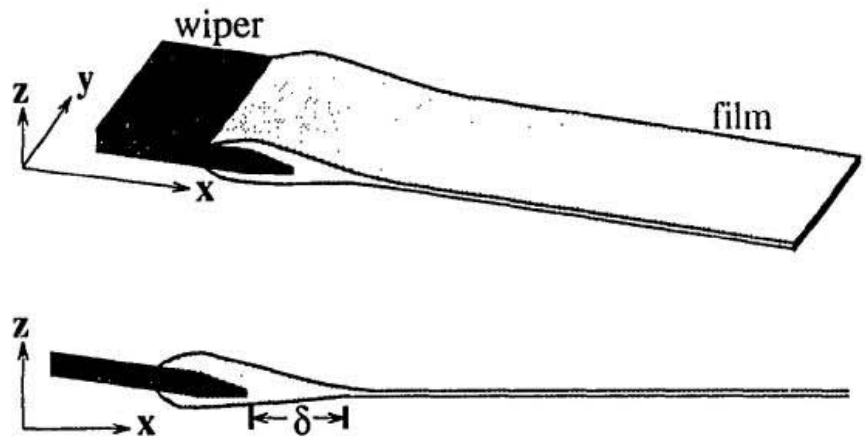

Figure A.2: Schematic illustration of the lateral boundary of a freely suspended film. δ represents the width of a boundary layer.

In real electroconvection experiments, the smectic films are of finite extent in the x-direction. Wetting effects result in a boundary layer at the sidewalls as shown in Figure A.2. The boundary layers will have a finite (but small compared to the width of the film) thickness along x-direction, shown as δ in Figure A.2, and a curved profile in the z-direction. Electric properties such as the dielectric permittivity are necessarily discontinuous at the interface between the film and the rigid sidewall, as well as at the two free surfaces

of the film. These discontinuities break the translational symmetry of the electric field which exists when the film is infinitely long. An interfacial charge density distribution along the smectic-sidewall interface and at the smectic-air interface will be produced by the non-zero x and z components of the field, given by [95, 187]

$$\mathbf{n} \cdot (\epsilon_2 \mathbf{E}_2 - \epsilon_1 \mathbf{E}_1) = \varrho, \tag{A.1}$$

where $\mathbf{n}$ is the unit normal to the interface, ϱ is the surface charge density at the interface, and the subscripts 1 and 2 refer to the different media on the two sides of the interface.

To simplify the analysis, the film is regarded perfectly two-dimensional (Figure A.3), with a large aspect ratio $\Gamma = l/d$. An electric field E_0 is applied in the plane of the film in the negative y-direction. E_0 is treated as a constant, even at the lateral boundary. The electrodes are assumed not responsible for the initiation of the flow. We assume that no free charge is present in the bulk of the film, so the film is not subject to an electric body force. However, we assume that there is a constant interfacial charge density distribution ϱ ($\varrho > 0$) along the boundary surface normal to negative x-direction at $x = 0$. In the case of a two-dimensional film, such a boundary surface is actually a boundary line with vanishing area. However, in the following analysis, we still use the words "boundary surface" and "interfacial charge density" to describe the lateral boundaries of a two-dimensional film.

The interfacial charge density distribution ϱ is a simplified approximation to the actual situation, which would involve contributions from the non-symmetric components of the electric field on the smectic-sidewall and the smectic-air interfaces, as discussed above. We only consider the effect of one lateral boundary ($x = 0$), and will ignore any change in E_0 and ϱ due to the influence of fluid flow.

Without external forces acting on the bulk of the incompressible fluid

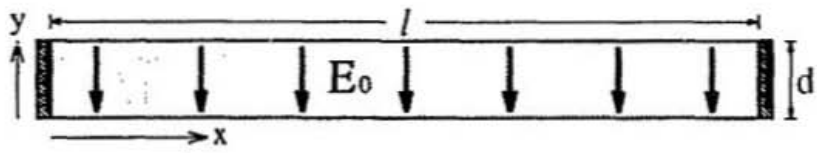

Figure A.3: Schematic plot of a two-dimensional film with length l, width d.

film, the momentum equation takes the form

$$\frac{\partial \mathbf{v}}{\partial t} + \mathbf{v} \cdot \nabla \mathbf{v} = -\frac{1}{\rho_m} \nabla p + \frac{\mu}{\rho_m} \nabla^2 \mathbf{v}, \tag{A.2}$$

where, as in Chapter 2, ∇ and the flow velocity $\mathbf{v}$ are two-dimensional, and the mass density ρ_m is assumed constant. In equation (A.2), p denotes the pressure and μ is the viscosity of the fluid.

Consistent with experimental observations below the onset of convection, we are interested in two-dimensional fluid flow with small characteristic velocity U, small characteristic length d, large kinematic viscosity ν ($\nu = \mu/\rho_m$), so the Reynolds number $Re = Ud/\nu$ is small. Here the characteristic length is chosen as the film width. The equation of motion for steady flow in a fluid with small Reynolds number can be reduced to the Stokes equation,

$$-\nabla p + \mu \nabla^2 \mathbf{v} = 0. \tag{A.3}$$

Together with the incompressibility condition

$$\nabla \cdot \mathbf{v} = 0, \tag{A.4}$$

Eq. (A.3) completely determines the motion of the fluid when boundary conditions are specified. By defining the vorticity $\omega(x, y)$ for flow in two dimensions (here ω is actually the z-component of the vorticity vector, we

use it as a scalar),

$$\omega = \frac{\partial v_y}{\partial x} - \frac{\partial v_x}{\partial y}, \tag{A.5}$$

Eq. (A.3) can be written as

$$\nabla^2 \omega = 0. \tag{A.6}$$

Boundary conditions at the two electrodes at $y = 0$ and $y = d$ are chosen to be $v_x = v_y = 0$ and $\omega = 0$, as required for a rigid boundary. Since the length of the film l is large compared to its width d, we ignore the influence of the boundary layer at $x = l$ and set $\omega = 0$ there.

At $x = 0$, we assume $v_x = 0$ and $\partial v_x/\partial y = 0$. However, we allow v_y to be nonzero at $x = 0$ because of the finite thickness δ of the boundary layer, and we place the rigid sidewall at $x = -\delta$. Due to the presence of the interfacial charge density ϱ, however, there will be an interfacial force acting on the boundary layer, tangential to the boundary surface at $x = 0$. It is given by

$$\mathbf{p}_{-x} = -\varrho E_0 \hat{\mathbf{y}}, \tag{A.7}$$

and acts in the direction of the electric field. Here $\mathbf{p}_{-x}$ represents the interfacial force acting on a unit area of the surface that is normal to negative x-direction. This force can be determined from the viscous stress tensor σ_{ij} for an incompressible fluid,

$$\sigma_{ij} = -p\delta_{ij} + \mu\left(\frac{\partial v_i}{\partial x_j} + \frac{\partial v_j}{\partial x_i}\right), \tag{A.8}$$

where p is the isotropic pressure. The expression for $\mathbf{p}_{-x}$ can therefore be written as

$$\mathbf{p}_{-x} = \left(-2\mu\frac{\partial v_x}{\partial x} + p\right)\hat{\mathbf{x}} - \mu\left(\frac{\partial v_y}{\partial x} + \frac{\partial v_x}{\partial y}\right)\hat{\mathbf{y}}, \tag{A.9}$$

and since $\partial v_x/\partial y = 0$ at $x = 0$, we obtain the additional boundary condition

$$\frac{\partial v_y}{\partial x} = \frac{\varrho}{\mu} E_0 \tag{A.10}$$

at $x = 0$, or equivalently, $\omega = \varrho E_0/\mu$ at $x = 0$.

Therefore, the original problem of vortex generation due to the interaction of the viscous stress and the electric shear force at one lateral boundary is reduced to seeking solutions of

$$\nabla^2\omega = 0, \tag{A.11}$$

with the boundary conditions

$$\begin{aligned} \omega|_{x=0} &= \varrho E_0/\mu, \\ \omega|_{x=l} &= 0, \\ \omega|_{y=0} &= 0, \\ \omega|_{y=d} &= 0. \end{aligned} \tag{A.12}$$

A.2 Solution of the Boundary Vortex Model

The solution of the equation (Eq. (A.12)) for vortex generation at boundary can be obtained by the method of separation of variable. We assume that the solution can be written in the form

$$\omega(x,y) = X(x)Y(y). \tag{A.13}$$

Substitution of Eq. (A.13) into Eq. (A.12) yields

$$X''(x)Y(y) + X(x)Y''(y) = 0, \tag{A.14}$$

where the primes denote differentiation with respect to the associated independent variable. Rewriting Eq. (A.14) gives

$$\frac{X''(x)}{X(x)} = -\frac{Y''(y)}{Y(y)}. \tag{A.15}$$

The left side of this equation is a function of x only and the right side is a function of y only, so both sides must equal the same constant value Λ. Equation (A.15) may then be written as two equations:

$$Y''(y) = -\Lambda Y(y), \tag{A.16}$$

$$X''(x) = \Lambda X(x). \tag{A.17}$$

Considering first the function $Y(y)$, we have

$$Y''(y) + \Lambda Y(y) = 0, \tag{A.18}$$

with the boundary conditions

$$\begin{aligned} Y(0) &= 0, \\ Y(d) &= 0. \end{aligned} \tag{A.19}$$

The corresponding solution is

$$Y(y) = C \sin\left(\frac{n\pi y}{d}\right), \tag{A.20}$$

with eigenvalues

$$\Lambda = \frac{n^2\pi^2}{d^2}. \qquad (n = 1, 2, 3\cdots) \tag{A.21}$$

From Eq. (A.17), the solution for $X(x)$ corresponding to the same eigenvalue Λ is

$$X(x) = Ae^{\frac{n\pi x}{d}} + Be^{-\frac{n\pi x}{d}}. \tag{A.22}$$

We thus obtain the general solution for $\omega(x, y)$,

$$\omega(x, y) = \sum_{n=1}^{\infty} \left(A_n e^{\frac{n\pi x}{d}} + B_n e^{-\frac{n\pi x}{d}}\right) \sin\left(\frac{n\pi y}{d}\right). \tag{A.23}$$

The boundary conditions at $x = 0$ and $x = l$ lead to

$$\sum_{n=1}^{\infty} (A_n + B_n) \sin\left(\frac{n\pi y}{d}\right) = \varrho E_0/\mu, \tag{A.24}$$

and

$$\sum_{n=1}^{\infty} \left(A_n e^{\frac{n\pi l}{d}} + B_n e^{-\frac{n\pi l}{d}}\right) \sin\left(\frac{n\pi y}{d}\right) = 0. \tag{A.25}$$

These two equations can be reduced to

$$A_n + B_n = \frac{4}{n\pi}(\varrho E_0/\mu), \qquad n = (2m + 1) \tag{A.26}$$

$$A_n + B_n = 0, \qquad (n = 2m) \tag{A.27}$$

and

$$\left(A_n e^{\frac{n\pi l}{d}} + B_n e^{-\frac{n\pi l}{d}}\right) = 0. \qquad (n = 1, 2, 3\cdots) \tag{A.28}$$

In writing the above expressions, we have used the Fourier series

$$1 = \frac{4}{\pi}\left(\sin\frac{\pi y}{d} + \frac{1}{3}\sin\frac{3\pi y}{d} + \frac{1}{5}\sin\frac{5\pi y}{d} + \cdots\right). \qquad (0 < y < d) \tag{A.29}$$

A_n and B_n can now be easily obtained. The results are

$$A_n = \frac{4}{n\pi}(\varrho E_0/\mu)\frac{1}{1-e^{\frac{2n\pi l}{d}}}, \tag{A.30}$$

$$B_n = \frac{4}{n\pi}(\varrho E_0/\mu)\frac{1}{1-e^{-\frac{2n\pi l}{d}}}, \tag{A.31}$$

for n odd; and

$$A_n = 0, \tag{A.32}$$

$$B_n = 0, \tag{A.33}$$

for n even. The general solution for $\omega(x,y)$ can therefore be written as

$$\omega(x,y) = \left(\frac{\varrho E_0}{\mu}\right)\sum_{n=1,3,5\ldots}\frac{4}{n\pi}\left(\frac{e^{\frac{n\pi x}{d}}}{1-e^{\frac{2n\pi l}{d}}}+\frac{e^{-\frac{n\pi x}{d}}}{1-e^{-\frac{2n\pi l}{d}}}\right)\sin\left(\frac{n\pi y}{d}\right). \tag{A.34}$$

If $l \gg d$, $\omega(x,y)$ can be reduced to

$$\omega(x,y) = \left(\frac{\varrho E_0}{\mu}\right)\sum_{n=1,3,5\ldots}\frac{4}{n\pi}e^{-\frac{n\pi x}{d}}\sin\left(\frac{n\pi y}{d}\right). \tag{A.35}$$

In our experiments we always observe the $n = 1$ mode. Keeping only the $n = 1$ term in Eq. (A.35) gives

$$\omega(x,y) = \frac{4}{\pi}\left(\frac{\varrho E_0}{\mu}\right)e^{-\frac{\pi x}{d}}\sin\left(\frac{\pi y}{d}\right). \tag{A.36}$$

The resulting vorticity field is plotted in Figure A.4.

The corresponding stream function $\psi(x,y)$ can be determined from the relation

$$\nabla^2\psi = \omega(x,y) \tag{A.37}$$

for two-dimensional fluid flow. The values of ψ are obtained by numerical integration of Eq. (A.37), where $\omega(x,y)$ is given by Eq. (A.36). The Green's

APPENDIX A

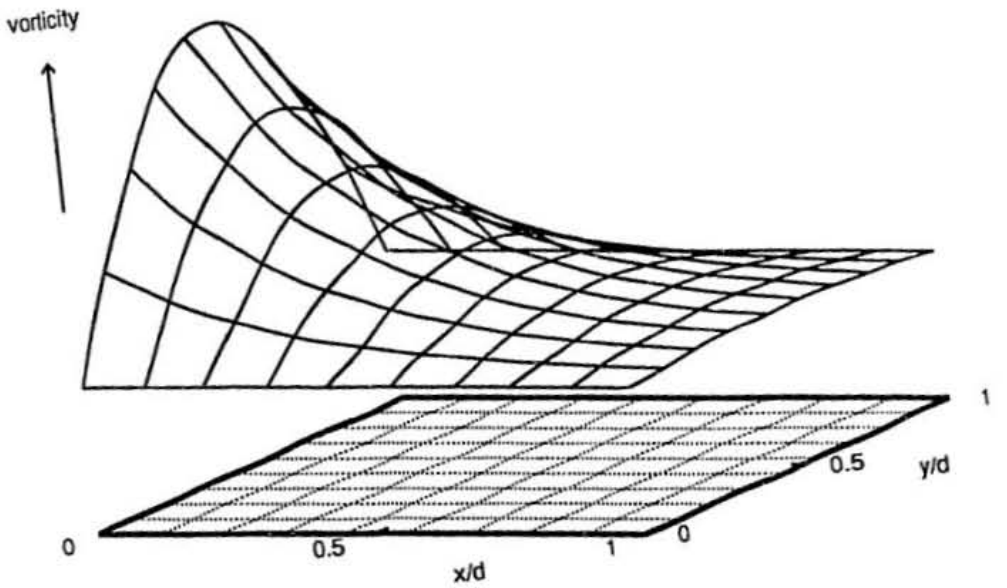

Figure A.4: Calculated vorticity field near the lateral boundary $x = 0$ below the onset of convection.

function for the Laplace operator ∇^2 in two-dimensional space,

$$G(x,y;\xi,\eta) = -\frac{1}{2\pi}\ln\frac{1}{\sqrt{(x-\xi)^2+(y-\eta)^2}}, \tag{A.38}$$

is used in the calculation. The results for stream function are given in Figure A.5, in which contours of constant $\psi(x,y)$ are shown and the vortical flow are indicated by the closed streamlines.

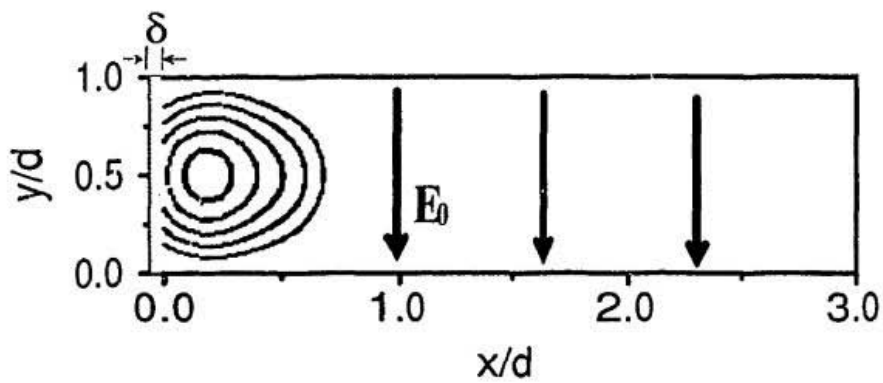

Figure A.5: Calculated streamlines near the lateral boundary $x = 0$ below the onset of convection. The electric field in the plane of the film and the boundary layer adjacent to sidewall are also indicated.

So far we have considered the effect of only one lateral boundary. When the interactions of the viscous stress and the electric shear force at both lateral boundaries are considered, assuming the same charge distribution ϱ at either sidewall, the boundary conditions for $\omega(x,y)$ at $x = l$ are $\omega|_{x=l} = -\omega|_{x=0} = -\varrho E_0/\mu$. Solving for A_n and B_n as above gives

$$A_n = -\frac{4}{n\pi}(\varrho E_0/\mu)\frac{1+e^{-\frac{n\pi l}{d}}}{e^{\frac{n\pi l}{d}}-e^{-\frac{n\pi l}{d}}}, \tag{A.39}$$

$$B_n = \frac{4}{n\pi}(\varrho E_0/\mu)\frac{1+e^{\frac{n\pi l}{d}}}{e^{\frac{n\pi l}{d}}-e^{-\frac{n\pi l}{d}}}, \tag{A.40}$$

for n odd; and

$$A_n = 0, \tag{A.41}$$

$$B_n = 0, \tag{A.42}$$

for n even. When $l \gg d$, the general solution for $\omega(x,y)$ can be written as

$$\omega(x,y) = \left(\frac{\varrho E_0}{\mu}\right) \sum_{n=1,3,5\ldots} \frac{4}{n\pi} e^{-\frac{n\pi x}{d}} \sin\left(\frac{n\pi y}{d}\right), \tag{A.43}$$

which is the same as when only one lateral boundary is considered.

It is worth emphasizing that the model presented above contains no bulk electric body force. The only source of the vortical flow in this model is the electrohydrodynamic shear-stress interaction [127], which originates from an interfacial charge density distribution at one lateral boundary. The streamlines given by this model are in qualitative agreement with the flow observed in experiments below the onset of convection.

Appendix B

Measuring Colour

B.1 Colorimetry

Colour[1] is a human perception. The first step in determining the visual perception that a particular light source or colored sample will produce is a measurement of the spectral intensity distribution of the light coming from the source or sample. The question that colorimetry addresses is, once the spectral intensity distribution is known, how can the colour be measured quantitatively? We desire an objective system of colorimetry in which, from the spectral intensity distribution, one can derive one quantity called *luminance*, that determines the brightness, and two quantities which together are called chromaticity, that determine the *hue* and *saturation*.

Experiments show that virtually all colours can be produced from a set of three lights whose colours are in widely separated regions of the spectrum. These three are called *primary colours* if they can also be added together to produce white. We denote by $\mathbf{e}_B$, $\mathbf{e}_G$, and $\mathbf{e}_R$ the unit amounts of the primaries, and for convenience the relative intensities of these unit amounts may be chosen in such a way that they give white (achromatic colour) when added together[2].

We designate as B, G, and R the quantities of each primaries needed to match the colour S of the sample, that is,

$$\mathbf{S} = B\mathbf{e}_B + G\mathbf{e}_G + R\mathbf{e}_R. \tag{B.1}$$

B, G, and R are called the tristimulus values of the colour with respect to the specific set of primaries. By definition, the tristimulus values for white are all equal, and increasing or decreasing B, G, and R by the same factor will change the overall brightness but not the hue and saturation. Therefore,

[1]This section is primarily based on reference [51, 204]

[2]Experiments show that a useful set of primaries is monochromatic blue at 436 nm, green at 546 nm, and red at 700 nm. To match white the power from these three must be in the proportion 14:19:1000. Consequently, the unit amounts of $\mathbf{e}_B$, $\mathbf{e}_G$, $\mathbf{e}_R$ could be chosen as, say, 0.014 Watt at 436 nm, 0.019 Watt at 546 nm, and 1.0 Watt at 700 nm.

we can describe a colour by its chromaticity, which depends on the relative magnitudes of B, G, and R, but not their absolute numerical values.

If we could measure the spectral intensity distribution of an unknown light source or a colored sample illuminated by white light and convert it into equivalent tristimulus values, then the colour would be specified. Any two colours with the same values of B, G, and R must look alike, no matter how different their spectral intensity distributions.

The key to this conversion lies in the use of colour matching functions $\bar{b}_\lambda$, $\bar{g}_\lambda$, and $\bar{r}_\lambda$, which determine how many units of each of the three primaries are needed to match one unit of monochromatic light at any wavelength λ. The tristimulus value B (or G or R) for a given spectral intensity distribution is thus obtained by the summation of $\bar{b}_\lambda$ (or $\bar{g}_\lambda$ or $\bar{r}_\lambda$) over all wavelengths, weighted by the actual intensity I_λ at that wavelength:

$$B = \int_0^\infty I_\lambda \bar{b}_\lambda d\lambda, \tag{B.2}$$

$$G = \int_0^\infty I_\lambda \bar{g}_\lambda d\lambda, \tag{B.3}$$

$$R = \int_0^\infty I_\lambda \bar{r}_\lambda d\lambda. \tag{B.4}$$

By defining new variables,

$$b = \frac{B}{B+G+R}, \tag{B.5}$$

$$g = \frac{G}{B+G+R}, \tag{B.6}$$

$$r = \frac{R}{B+G+R}, \tag{B.7}$$

we observe that b, g, and r have an important feature: they are unchanged if samples differ in luminance but not chromaticity. As noted before, to specify

chromaticity we need quote only two of these numbers.

For computational convenience and to ensure the tristimulus values are always positive, the Commission Internationale de l'Eclairage (CIE) recommended a set of primaries $\mathbf{e}_X$, $\mathbf{e}_Y$, and $\mathbf{e}_Z$ as a standard. They were defined as linear combinations of the monochromatic primaries $\mathbf{e}_B$, $\mathbf{e}_G$, and $\mathbf{e}_R$. These primaries were chosen so that a match to white occurs for equal tristimulus values of X, Y, and Z, as was the case for B, G, and R above. In addition, the combinations were arranged so that the value of Y determines the luminance of the sample colour.

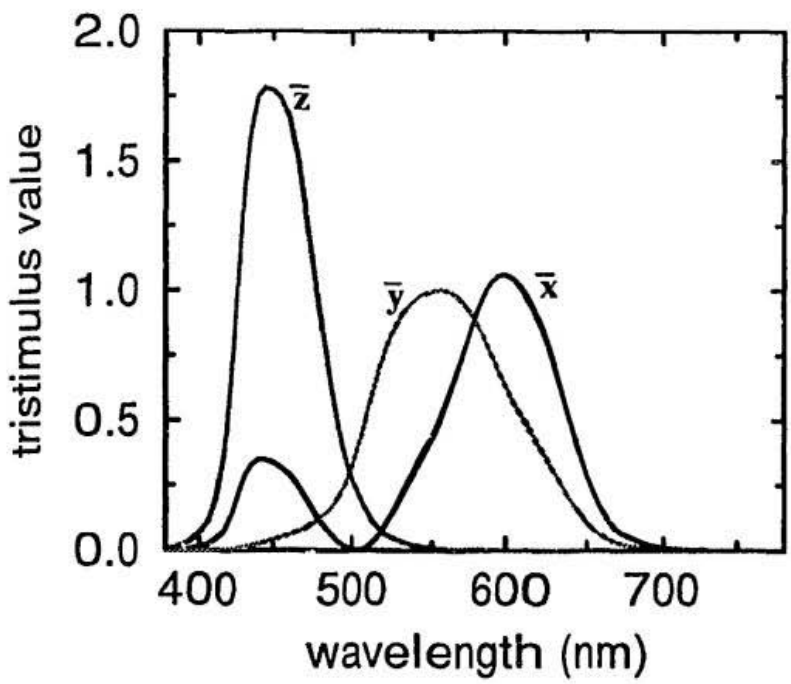

Figure B.1: The standard CIE colour matching functions.

The tristimulus values X, Y, and Z can be calculated by using a new set of colour matching functions $\bar{x}_\lambda$, $\bar{y}_\lambda$, $\bar{z}_\lambda$, given in Table B.1 and plotted in Figure B.1. The tristimulus value for a colour sample of interest is calculated by the same procedure described for B, G, and R, that is,

$$X = \int_0^\infty I_\lambda \bar{x}_\lambda d\lambda, \tag{B.8}$$

$$Y = \int_0^\infty I_\lambda \bar{y}_\lambda d\lambda, \tag{B.9}$$

$$Z = \int_0^\infty I_\lambda \bar{z}_\lambda d\lambda. \tag{B.10}$$

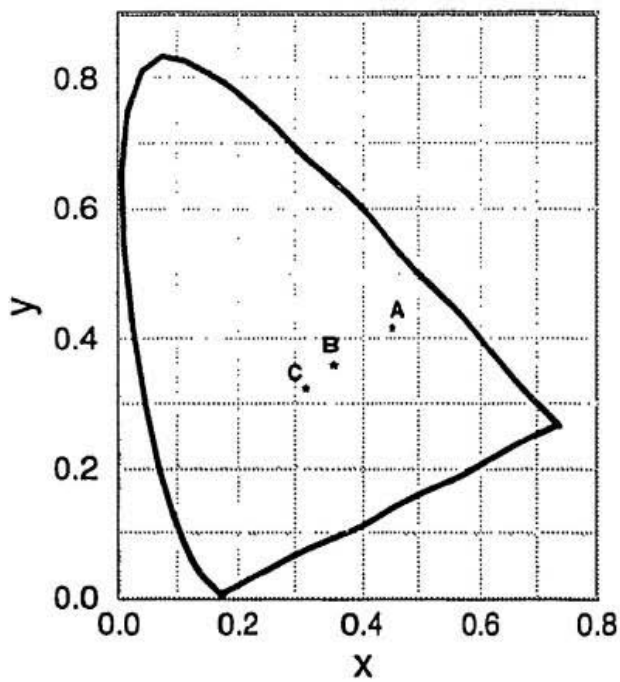

Figure B.2: The CIE chromaticity diagram. The chromaticities of the CIE standard light sources A, B, and C are indicated.

As before, we introduce new variables that have the overall strength of the primaries divided out:

$$x = \frac{X}{X+Y+Z}, \tag{B.11}$$

$$y = \frac{Y}{X+Y+Z}, \tag{B.12}$$

$$z = \frac{Z}{X+Y+Z}. \tag{B.13}$$

x, y, and z are called the CIE chromaticity coordinates, which are independent of the luminance according the definition. Together they comprise what is termed the CIE chromaticity of a colour.

The chromaticity diagram recommended by the CIE is shown in Figure B.2, in which the horizontal coordinate is x and the vertical coordinate is y. Since only two of the three quantities are needed to specify a colour, any colour can be specified in terms of these two coordinates, supplemented by the tristimulus value Y expressed in an appropriate photometric unit. All possible colours on the CIE chromaticity diagram fall within an area of the diagram bounded by a horseshoe-shaped curve called the *spectrum locus*, on which the monochromatic hues are found (see Table B.2). Achromatic colours which differ only in luminance have equal values for X, Y, and Z, with coordinates $(1/3, 1/3)$.

In summary, the CIE procedure converts the spectral intensity distribution into three quantities, x, y, and Y by the use of standardized tables based on the perceptions of the "average" human observers. In addition, the CIE has tabulated several standard illuminant spectral intensity distributions (called standard sources A, B, and C) to approximate common light sources [51]. These are given in Table B.3 and Figure B.3. The spectral intensity distribution I_λ in our experiments was calculated by assuming that our illuminator produced the spectrum $I_{0\lambda}$ of the CIE standard source A (a gas-filled lamp of colour temperature 2848K).

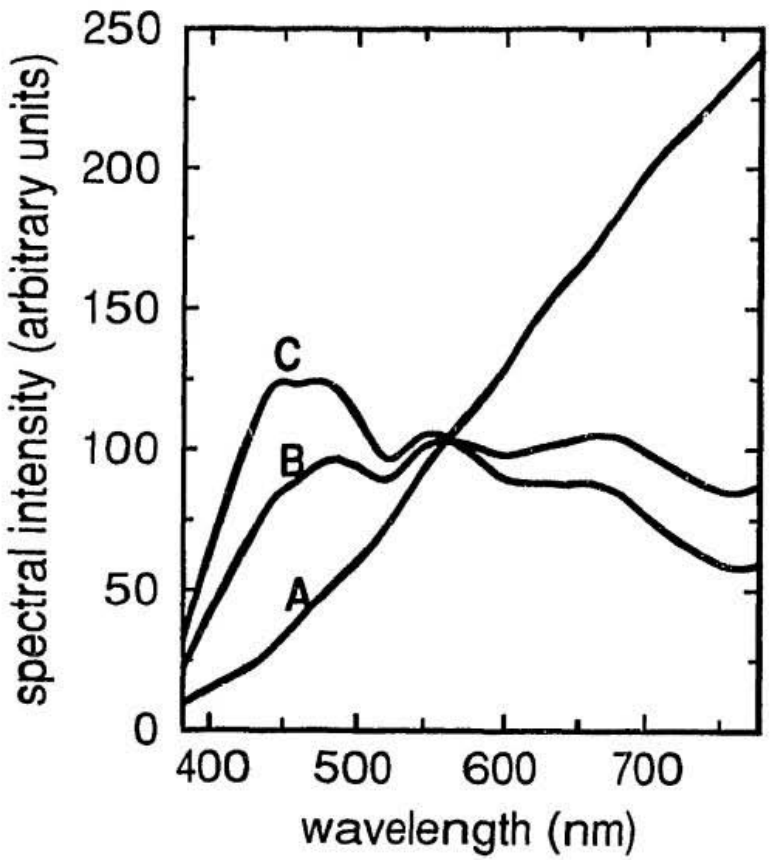

Figure B.3: Spectral distribution of the CIE standard light sources.

B.2 Computer Program for Colorimetry

```
**********************************************************************
***** colorimetry: interference of s-polarized light from smectic film *****
**********************************************************************
***** SOURCE: data of standard light sources A,B,C
***** TRISTI: data of standard tristimulus for colorimetry
***** SLOCUS: data of standard coordinates of spectrum colours
***** PA,PB,PC: spectral intensity distributions of standard sources
***** XX,YY,ZZ: standard tristimulus values of the spectrum: x,y,z
***** XL,YL,ZL: coordinate of the locus of spectrum colors
***** XR,YR,ZR: tristimulus values of reflected light
***** X,Y: coordinates of colour in chromaticity diagram
***** R, PHI: reflectivity of s-polarized light and the phase deference
***** RLMD: wavelength of light (nm)
***** THETA: incident angle
***** ON: refractive index of uniaxial liquid crystal 8CB
***** TM: film thickness in molecular layers
***** D: thickness of one molecular layer for 8CB (nm)
**********************************************************************
DIMENSION RLMD(81)
DIMENSION PA(81),PB(81),PC(81)
DIMENSION XX(81),YY(81),ZZ(81)
DIMENSION XL(81),YL(81),ZL(81)
DIMENSION R(81),PHI(81)
DIMENSION SOURCE(81,4),TRISTI(81,4),SLOCUS(81,4)
OPEN(02,FILE='CIE-source.dat',STATUS='OLD')
OPEN(03,FILE='CIE-tristimulus.dat',STATUS='OLD')
OPEN(04,FILE='CIE-locus.dat',STATUS='OLD')
DO 10 I=1,81
READ(02,5) SOURCE(I,1),SOURCE(I,2),SOURCE(I,3),SOURCE(I,4)
READ(03,8) TRISTI(I,1),TRISTI(I,2),TRISTI(I,3),TRISTI(I,4)
```

```
READ(04,9) SLOCUS(I,1),SLOCUS(I,2),SLOCUS(I,3),SLOCUS(I,4)
5 FORMAT(F5.1,2X,F6.2,2X,F6.2,2X,F6.2)
8 FORMAT(F5.1,2X,F6.4,2X,F6.4,2X,F6.4)
9 FORMAT(F5.1,2X,F6.4,2X,F6.4,2X,F6.4)
10 CONTINUE
CLOSE(02)
CLOSE(03)
CLOSE(04)
DO 20 I=1,81
RLMD(I)=SOURCE(I,1)
PA(I)=SOURCE(I,2)
PB(I)=SOURCE(I,3)
PC(I)=SOURCE(I,4)
XX(I)=TRISTI(I,2)
YY(I)=TRISTI(I,3)
ZZ(I)=TRISTI(I,4)
XL(I)=SLOCUS(I,2)
YL(I)=SLOCUS(I,3)
ZL(I)=SLOCUS(I,4)
20 CONTINUE
OPEN(05,FILE='colour.dat',STATUS='NEW')
TM=0.0
25 TM=TM+1.0
D=3.16
ON=1.516
THETA=0.0
DO 30 I=1,81
RRU=ABS(COS(THETA)-SQRT(ON*ON-SIN(THETA)*SIN(THETA)))
RRL=ABS(COS(THETA)+SQRT(ON*ON-SIN(THETA)*SIN(THETA)))
RR=(RRU/RRL)*(RRU/RRL)
PHI(I)=(2.0*3.1416/RLMD(I))*TM*D*SQRT(ON*ON-SIN(THETA)*SIN(THETA))
F=4.0*RR/((1.0-RR)*(1.0-RR))
```

```
R(I)=F*SIN(PHI(I))*SIN(PHI(I))/(1.0+F*SIN(PHI(I))*SIN(PHI(I)))
30 CONTINUE
XR=0.0
YR=0.0
ZR=0.0
YYY=0.0
DO 50 I=1,81
YYY=YYY+YY(I)*PA(I)*5.0
50 CONTINUE
DO 60 I=1,81
XR=XR+XX(I)*PA(I)*R(I)*5.0/YYY
YR=YR+YY(I)*PA(I)*R(I)*5.0/YYY
ZR=ZR+ZZ(I)*PA(I)*R(I)*5.0/YYY
60 CONTINUE
X=XR/(XR+YR+ZR)
Y=YR/(XR+YR+ZR)
WRITE(05,65)X,Y
65 FORMAT(1X,2F10.6)
WRITE(*,*)TM
IF(TM.LT.200.0) GOTO 25
CLOSE(05)
STOP
END
```

Table B.1: The CIE Standard Colour Matching Functions

$\lambda(nm)$	$\bar{x}_\lambda$	$\bar{y}_\lambda$	$\bar{z}_\lambda$	$\lambda(nm)$	$\bar{x}_\lambda$	$\bar{y}_\lambda$	$\bar{z}_\lambda$
380.0	0.0014	0.0000	0.0065	585.0	0.9786	0.8163	0.0014
385.0	0.0022	0.0001	0.0105	590.0	1.0263	0.7570	0.0011
390.0	0.0042	0.0001	0.0201	595.0	1.0567	0.6949	0.0010
395.0	0.0076	0.0002	0.0362	600.0	1.0622	0.6310	0.0008
400.0	0.0143	0.0004	0.0679	605.0	1.0456	0.5668	0.0006
405.0	0.0232	0.0006	0.1102	610.0	1.0026	0.5030	0.0003
410.0	0.0435	0.0012	0.2074	615.0	0.9384	0.4421	0.0002
415.0	0.0776	0.0022	0.3713	620.0	0.8544	0.3810	0.0002
420.0	0.1344	0.0040	0.6456	625.0	0.7514	0.3210	0.0001
425.0	0.2148	0.0073	1.0391	630.0	0.6424	0.2650	0.0000
430.0	0.2839	0.0116	1.3856	635.0	0.5419	0.2170	0.0000
435.0	0.3285	0.0168	1.6230	640.0	0.4479	0.1750	0.0000
440.0	0.3484	0.0230	1.7471	645.0	0.3608	0.1382	0.0000
445.0	0.3481	0.0298	1.7826	650.0	0.2835	0.1070	0.0000
450.0	0.3362	0.0380	1.7721	655.0	0.2187	0.0816	0.0000
455.0	0.3187	0.0480	1.7441	660.0	0.1649	0.0610	0.0000
460.0	0.2908	0.0600	1.6692	665.0	0.1212	0.0446	0.0000
465.0	0.2511	0.0739	1.5281	670.0	0.0874	0.0320	0.0000
470.0	0.1954	0.0910	1.2876	675.0	0.0636	0.0232	0.0000
475.0	0.1421	0.1126	1.0419	680.0	0.0468	0.0170	0.0000
480.0	0.0956	0.1390	0.8130	685.0	0.0329	0.0119	0.0000
485.0	0.0580	0.1693	0.6162	690.0	0.0227	0.0082	0.0000
490.0	0.0320	0.2080	0.4652	695.0	0.0158	0.0057	0.0000
495.0	0.0147	0.2586	0.3533	700.0	0.0114	0.0041	0.0000
500.0	0.0049	0.3230	0.2720	705.0	0.0081	0.0029	0.0000
505.0	0.0024	0.4073	0.2123	710.0	0.0058	0.0021	0.0000
510.0	0.0093	0.5030	0.1582	715.0	0.0041	0.0015	0.0000
515.0	0.0291	0.6082	0.1117	720.0	0.0029	0.0010	0.0000
520.0	0.0633	0.7100	0.0782	725.0	0.0020	0.0007	0.0000
525.0	0.1096	0.7932	0.0573	730.0	0.0014	0.0005	0.0000
530.0	0.1655	0.8620	0.0422	735.0	0.0010	0.0004	0.0000
535.0	0.2257	0.9149	0.0298	740.0	0.0007	0.0003	0.0000
540.0	0.2904	0.9540	0.0203	745.0	0.0005	0.0002	0.0000
545.0	0.3597	0.9803	0.0134	750.0	0.0003	0.0001	0.0000
550.0	0.4334	0.9950	0.0087	755.0	0.0002	0.0001	0.0000
555.0	0.5121	1.0002	0.0057	760.0	0.0002	0.0001	0.0000
560.0	0.5945	0.9950	0.0039	765.0	0.0001	0.0000	0.0000
565.0	0.6784	0.9786	0.0027	770.0	0.0001	0.0000	0.0000
570.0	0.7621	0.9520	0.0021	775.0	0.0000	0.0000	0.0000
575.0	0.8425	0.9154	0.0018	780.0	0.0000	0.0000	0.0000
580.0	0.9163	0.8700	0.0017				

Table B.2: Chromaticity Coordinates of Spectrum Locus

$\lambda(nm)$	x_λ	y_λ	z_λ	$\lambda(nm)$	x_λ	y_λ	z_λ
380.0	0.1741	0.0050	0.8209	585.0	0.5448	0.4544	0.0008
385.0	0.1740	0.0050	0.8210	590.0	0.5752	0.4242	0.0006
390.0	0.1738	0.0049	0.8213	595.0	0.6029	0.3965	0.0006
395.0	0.1736	0.0049	0.8215	600.0	0.6270	0.3725	0.0005
400.0	0.1733	0.0048	0.8219	605.0	0.6482	0.3514	0.0004
405.0	0.1730	0.0048	0.8222	610.0	0.6658	0.3340	0.0002
410.0	0.1726	0.0048	0.8226	615.0	0.6801	0.3197	0.0002
415.0	0.1721	0.0048	0.8231	620.0	0.6915	0.3083	0.0002
420.0	0.1714	0.0051	0.8235	625.0	0.7006	0.2993	0.0001
425.0	0.1703	0.0058	0.8239	630.0	0.7079	0.2920	0.0001
430.0	0.1689	0.0069	0.8242	635.0	0.7140	0.2859	0.0001
435.0	0.1669	0.0086	0.8245	640.0	0.7190	0.2809	0.0001
440.0	0.1644	0.0109	0.8247	645.0	0.7230	0.2770	0.0000
445.0	0.1611	0.0138	0.8251	650.0	0.7260	0.2740	0.0000
450.0	0.1566	0.0177	0.8257	655.0	0.7283	0.2717	0.0000
455.0	0.1510	0.0227	0.8263	660.0	0.7300	0.2700	0.0000
460.0	0.1440	0.0297	0.8263	665.0	0.7311	0.2689	0.0000
465.0	0.1355	0.0399	0.8246	670.0	0.7320	0.2680	0.0000
470.0	0.1241	0.0578	0.8181	675.0	0.7327	0.2673	0.0000
475.0	0.1096	0.0868	0.8036	680.0	0.7334	0.2666	0.0000
480.8	0.0913	0.1327	0.7760	685.0	0.7340	0.2660	0.0000
485.0	0.0687	0.2007	0.7306	690.0	0.7344	0.2656	0.0000
490.0	0.0454	0.2950	0.6596	695.0	0.7346	0.2654	0.0000
495.0	0.0235	0.4127	0.5638	700.0	0.7347	0.2653	0.0000
500.0	0.0082	0.5384	0.4534	705.0	0.7347	0.2653	0.0000
505.0	0.0039	0.6548	0.3413	710.0	0.7347	0.2653	0.0000
510.0	0.0139	0.7502	0.2359	715.0	0.7347	0.2653	0.0000
515.0	0.0389	0.8120	0.1491	720.0	0.7347	0.2653	0.0000
520.0	0.0743	0.8338	0.0919	725.0	0.7347	0.2653	0.0000
525.0	0.1142	0.8262	0.0596	730.0	0.7347	0.2653	0.0000
530.0	0.1547	0.8059	0.0394	735.0	0.7347	0.2653	0.0000
535.0	0.1929	0.7816	0.0255	740.0	0.7347	0.2653	0.0000
540.0	0.2296	0.7543	0.0161	745.0	0.7347	0.2653	0.0000
545.0	0.2658	0.7243	0.0099	750.0	0.7347	0.2653	0.0000
550.0	0.3016	0.6923	0.0061	755.0	0.7347	0.2653	0.0000
555.0	0.3373	0.6589	0.0038	760.0	0.7347	0.2653	0.0000
560.0	0.3731	0.6245	0.0024	765.0	0.7347	0.2653	0.0000
565.0	0.4087	0.5896	0.0017	770.0	0.7347	0.2653	0.0000
570.0	0.4441	0.5547	0.0012	775.0	0.7347	0.2653	0.0000
575.0	0.4788	0.5202	0.0010	780.0	0.7347	0.2653	0.0000
580.0	0.5125	0.4866	0.0009				

Table B.3: Spectral Intensity Distribution of Standard Sources

$\lambda(nm)$	$I^A_{0\lambda}$	$I^B_{0\lambda}$	$I^C_{0\lambda}$	$\lambda(nm)$	$I^A_{0\lambda}$	$I^B_{0\lambda}$	$I^C_{0\lambda}$
380.0	9.79	22.40	33.00	585.0	118.08	100.07	95.43
385.0	10.90	26.85	39.92	590.0	121.73	99.20	93.20
390.0	12.09	31.30	47.40	595.0	125.39	98.44	91.22
395.0	13.36	36.18	55.17	600.0	129.04	98.00	89.70
400.0	14.71	41.30	63.30	605.0	132.70	98.08	88.83
405.0	16.15	46.62	71.81	610.0	136.34	98.50	88.40
410.0	17.68	52.10	80.60	615.0	139.99	99.06	88.19
415.0	19.29	57.70	89.53	620.0	143.62	99.70	88.10
420.0	21.00	63.20	98.10	625.0	147.23	100.36	88.06
425.0	22.79	68.37	105.80	630.0	150.83	101.00	88.00
430.0	24.67	73.10	112.40	635.0	154.42	101.56	87.86
435.0	26.64	77.31	117.75	640.0	157.98	102.20	87.80
440.0	28.70	80.80	121.50	645.0	161.51	103.05	87.99
445.0	30.85	83.44	123.45	650.0	165.03	103.90	88.20
450.0	33.09	85.40	124.00	655.0	168.51	104.59	88.20
455.0	35.41	86.88	123.60	660.0	171.96	105.00	87.90
460.0	37.82	88.30	123.10	665.0	175.38	105.08	87.22
465.0	40.30	90.08	123.30	670.0	178.77	104.90	86.30
470.0	42.87	92.00	123.80	675.0	182.12	104.55	85.30
475.0	45.52	93.75	124.09	680.0	185.43	103.90	84.00
480.0	48.25	95.20	123.90	685.0	188.70	102.84	82.21
485.0	51.04	96.23	122.92	690.0	191.93	101.60	80.20
490.0	53.91	96.50	120.70	695.0	195.12	100.38	78.24
495.0	56.85	95.17	116.90	700.0	198.25	99.10	76.30
500.0	59.86	94.20	112.10	705.0	201.36	97.70	74.36
505.0	62.93	92.37	106.98	710.0	204.41	96.20	72.40
510.0	66.06	90.70	102.30	715.0	207.41	94.60	70.40
515.0	69.25	89.65	98.81	720.0	210.36	92.90	68.30
520.0	72.50	89.50	96.90	725.0	213.26	91.10	66.30
525.0	75.79	90.43	96.78	730.0	216.12	89.40	64.40
530.0	79.13	92.20	98.00	735.0	218.92	88.00	62.80
535.0	82.52	94.46	99.94	740.0	221.66	86.90	61.50
540.0	85.95	96.90	102.10	745.0	224.36	85.90	60.20
545.0	89.41	99.16	103.95	750.0	227.00	85.20	59.20
550.0	92.91	101.00	105.20	755.0	229.58	84.80	58.50
555.0	96.44	102.20	105.67	760.0	232.11	84.70	58.10
560.0	100.00	102.80	105.30	765.0	234.59	84.90	58.00
565.0	103.58	102.92	104.11	770.0	237.01	85.40	58.20
570.0	107.18	102.60	102.30	775.0	239.37	86.10	58.50
575.0	110.80	101.90	100.15	780.0	241.67	87.00	59.10
580.0	114.44	101.00	97.80				

Bibliography

[1] H. D. Abarbanel, R. Brown, J. J. Sidorowich, and L. S. Tsimring, Rev. Mod. Phys. **65**, 1331 (1993).

[2] R. J. Adrian, Int. J. Heat Fluid Flow **7**, 127 (1986).

[3] G. Ahlers, Phys. Rev. Lett. **33**, 1185 (1974).

[4] G. Ahlers, in *Lectures in the Sciences of Complexity*, edited by D. Stein (Addison-Wesley, Reading, 1989).

[5] G. Ahlers and R. P. Behringer, Prog. Theo. Phys. Suppl. **64**, 186 (1978).

[6] G. Ahlers, M. C. Cross, P. C. Hohenberg, and S. Safran, J. Fluid Mech. **110**, 297 (1981).

[7] H. Aref, J. Fluid Mech. **143**, 1 (1984).

[8] W. Arter, A. Bernoff, and A. C. Newell, Phys. Fluids **30**, 3840 (1987).

[9] P. Atten and J. C. Lacroix, J. de Mech. **18**, 469 (1979).

[10] D. Avsec and M. Luntz, C. R. Acad. Sci. Paris **203**, 1104 (1936).

[11] B. Bahadur, *Liquid Crystals: Applications and Uses* (World Scientific, Singapore, 1990).

[12] Ch. Bahr and D. Fliegner, Phys. Rev. A **46**, 7657 (1992).

[13] Ch. Bahr and D. Fliegner, Phys. Rev. Lett. **70**, 1842 (1993).

[14] G. I. Barenblatt, *Dimensional Analysis* (Gordon and Breach, New York, 1987).

[15] G. K. Batchelor, *Introduction to Fluid Mechanics* (Cambridge University Press, Cambridge, 1967).

[16] J. Bechhoefer, A. Simon, A. Libchaber, and P. Oswald, Phys. Rev. A **40**, 2042 (1989).

[17] O. Belorgey, and J. J. Benattar, Phys. Rev. Lett. **66**, 313 (1991).

[18] E. Ben-Jacob, H. Shmueli, O. Shochet, and A. Tenenbaum, Physica A **187**, 378 (1992).

[19] E. Ben-Jacob, O. Shochet, A. Tenenbaum, I. Cohen, A. Czirók, and T. Vicsek, Phys. Rev. E. **53**, 1835 (1996).

[20] H. Bénard, Rev. Gen. Sci. **11**, 1261 (1900).

[21] D. Bensimon, L. P. Kadanoff, S. Lian, B. I. Shraiman, and C. Tang, Rev. Mod. Phys. **58**, 977 (1986).

[22] P. Berge, J. de Phys. C1 **37**, 23 (1976).

[23] P. Berge and M. Dubois, Contemp. Phys. **25**, 535 (1984).

[24] P. Berge, Y. Pomeau, and C. Vidal, *Order within Chaos* (Wiley, New York, 1984).

[25] L. M. Blinov, *Electro-optical and Magneto-optical Properties of Liquid Crystals* (Wiley, New York, 1983).

[26] E. Bodenschatz, J. R. de Bruyn, G. Ahlers, and D. S. Cannell, Phys. Rev. Lett. **67**, 3078 (1991).

[27] E. Bodenschatz, W. Zimmermann, and L. Kramer, J. de Phys. **49**, 1875 (1988).

[28] M. Born and E. Wolf, *Principles of Optics* (Pergamon, Oxford, 1975).

[29] C. J. F. Böttcher and P. Bordewijk *Theory of Electric Polarization*, vol. II. 2nd ed. (Elsevier, Amsterdam, 1978).

[30] D. Braithwaite, E. Beaugnon, and R. Tournier, Nature **354**, 134 (1991).

[31] F. Brochard, P. G. deGennes, and P. Pfeuty, J. de Phys. **37**, 1099 (1976).

[32] J. D. Brock, R. J. Birgeneau, J. D. Lister, and A. Aharony, Phys. Today **42** 7, 52, (1989).

[33] E. O. Budrene and H. C. Berg, Nature **349**, 630 (1991).

[34] E. O. Budrene and H. C. Berg, Nature **376**, 49 (1995).

[35] A. Buka, T. T. Katona, and L. Kramer, Phys. Rev. E **49**, 5271 (1994).

[36] A. Buka, P. Palffy-Muhoray, and Z. Racz, Phys. Rev. A **36**, 3984 (1987).

[37] F. H. Busse, J. Fluid Mech. **30**, 625 (1967).

[38] F. H. Busse, Rep. Prog. Phys. **41**, 1929 (1978).

[39] F. H. Busse, in *Hydrodynamic Instabilities and the Transition to Turbulence*, edited by H. L. Swinney and J. P. Gollub (Springer, New York, 1981), p.97.

[40] F. H. Busse and R. M. Clever, J. Fluid Mech. **91**, 319 (1979).

[41] A. B. Cambel, *Applied Chaos Theory: A Paradigm for Complexity* (Academic, Boston, 1993).

[42] D.S. Cannell, M.A. Dominguez-Lerma, and G. Ahlers, Phys. Rev. Lett. **50**, 1365 (1983).

[43] C. Canuto, M. Y. Hussaini, A. Quarteroni, and T. A. Zang, *Spectral Methods in Fluid Dynamics* (Springer, New York, 1988).

[44] O. Cardoso and P. Tabeling, Eur. J. Mech. B. **8**, 459 (1989).

[45] E. F. Carr, Mol. Cryst. Liq. Cryst. **7**, 253 (1969).

[46] B. Castaing, G. Gunaratne, F. Heslot, L. Kadanoff, A. Libchaber, S. Thomae, X. Z. Wu, S. Zaleski, and G. Zanetti, J. Fluid Mech. **204**, 1 (1989).

[47] R. Chacon, A. T. Perez, and A. Castellanos, Phys. Rev. E **49**, 1756 (1994).

[48] S. Chandrasekhar, *Hydrodynamic and Hydromagnetic Stability* (Oxford University Press, Oxford, 1961).

[49] S. Chandrasekhar, *Liquid Crystals* (Cambridge University Press, Cambridge, 1992).

[50] P. E. Cladis, P. L. Finn, and H. R. Brand, Phys. Rev. Lett. **75**, 1518 (1995).

[51] Committee on Colorimetry, Optical Society of America, *The Science of Color* (Crowell, New York, 1963).

[52] Y. Couder, J. M. Chomaz, and M. Rabaud, Physica D. **37**, 384 (1989).

[53] J. D. Crawford and E. Knobloch, Annu. Rev. Fluid Mech. **23**, 341 (1991).

[54] M. C. Cross, P. G. Daniels, P. C. Hohenberg, and E. D. Siggia, Phys. Rev. Lett. **45**, 898 (1980).

[55] M. C. Cross, P. G. Daniels, P. C. Hohenberg, and E. D. Siggia, J. Fluid Mech. **127**, 155 (1983).

[56] M. C. Cross and P. C. Hohenberg, Rev. Mod. Phys. **65**, 851 (1993).

[57] S. H. Davis, J. Fluid Mech. **30**, 465 (1967).

[58] Z. Daya and S. W. Morris, private communications.

[59] P. G. de Gennes, *The Physics of Liquid Crystals* (Clarendon, Oxford, 1974).

[60] R. C. DiPrima and H. L. Swinney, in *Hydrodynamic Instabilities and the Transition to Turbulence*, edited by H. L. Swinney and J. P. Gollub (Springer-Verlag, New York, 1981), p.139.

[61] M. A. Dominguez-Lerma, G. Ahlers, and D. S. Cannell, Phys. Rev. E **52**, 6159 (1995).

[62] M. A. Dominguez-Lerma, D. S. Cannell, and G. Ahlers, Phys. Rev. A **34**, 4956 (1986).

[63] M. Dubois and P. Berge, J. Fluid Mech. **85**, 641 (1978).

[64] E. Dubois-Violette, G. Durand, E. Guyon, P. Manneville, and P. Pieranski, in *Liquid Crystals*, edited by L. Liebert (Academic, New York, 1978), p.147.

[65] D. A. Dunmur, M. R. Manterfield, W. H. Miller, and J. K. Dunleavy, Mol. Cryst. Liq. Cryst. **45**, 127 (1978).

[66] V. Eckhaus, *Studies in Nonlinear Stability Theory*, Springer Tracts in Natural Philosophy, vol. 6 (Springer-Verlag, Berlin, 1965).

[67] J. P. Eckmann and D. Ruelle, Rev. Mod. Phys. **57**, 617 (1985).

[68] L. E. Ericksen, Adv. Liquid Cryst. **2**, 233 (1976).

[69] A. C. Eringen and G. A. Maugin, *Electrodynamics of Continua*, vol. I and II (Springer, New York, 1990).

[70] D. Exerowa, B. Balinov, A. Nikolova, and D. Kashchiev, J. Colloid Interface Sci. **95**, 289 (1983).

[71] S. Faetti, L. Fronzoni, and P. A. Rolla, J. Chem. Phys. **79**, 1427 (1983).

[72] S. Faetti, L. Fronzoni, and P. A. Rolla, J. Chem. Phys. **79**, 5054 (1983).

[73] N. J. Felici, Rev. Gen. Electr. **78**, 717 (1969).

[74] R. J. Field and M. Burger, Eds., *Oscillations and Travelling Waves in Chemical Systems* (Wiley, New York, 1985).

[75] P. C. Fife, *Mathematical Aspects of Reacting and Diffusing Systems* (Springer-Verlag, New York, 1979).

[76] J. M. Flesselles, A. J. Simon, and A. Libchaber, Adv. Phys. **40**, 1 (1991).

[77] G. Friedel, Ann. Phys. (Paris) **18**, 273 (1922).

[78] M. Gharib and P. Derango, Physcia D. **37**, 406 (1989).

[79] S. Gierlotka, P. Lambooy, and W. H. De Jeu, Europhys. Lett. **12**, 341 (1990).

[80] V. L. Ginzburg, and L. D. Landau, in *Collected Papers of L.D.Landau* (Gordon and Breach, New York, 1965), p.546 .

[81] N. Goldenfeld, *Lectures on Phase Transition and the Renormalization Group* (Addison-Wesley, New York, 1992).

[82] L. P. Gor'kov, Sov. Phys. JETP **6**, 311 (1957).

[83] D. Gottlieb and S. A. Orszag, *Numerical Analysis of Spectral Methods* (SIAM, Philadelphia, 1977).

[84] G. W. Gray and J. W. Goodby, *Smectic Liquid Crystals* (Leonard Hill, Glasgow, 1984).

[85] J. Guckenheimer and P. Holmes, *Nonlinear Oscillations, Dynamical Systems, and Bifurcations of Vector Fields.* (Springer, New York, 1986) .

[86] F. Guenoun, A. Schlachli, D. Sentenac, J. W. Mays, and J. J. Benattar, Phys. Rev. Lett. **74**, 3628 (1995).

[87] J. P. Gullub and M. H. Frelich, in *Fluctuations, Instabilities, and Phase Transitions*, edited by T. Riste (Plenum, New York, 1975), p.195.

[88] W. Helfrich, J. Chem. Phys. **51**, 4092 (1969).

[89] E. J. Hopfinger, F. K. Browand, and Y. Gange, J. Fluid Mech. **125**, 505 (1982).

[90] L. Howle, R. Behringer, and J. Georgiadis, Nature **362**, 230 (1993).

[91] C. C. Huang and T. Stoebe, Adv. Phys. **42**, 343 (1993).

[92] S. C. Huang and M. E. Glickman, Acta Metall. **29**, 717 (1981).

[93] H. E. Huppert, Nature **300**, 427 (1982).

[94] D. T. Hurle and E. Jakeman, J. Fluid Mech. **47**, 667 (1971).

[95] J. D. Jackson, *Classical Electrodynamics* (Wiley. New York, 1962).

[96] K. A. Jackson and J. D. Hunt, Acta Metall. **13**, 1212 (1965).

[97] D. D. Joseph, *Stability of Fluid Motions*, vol. I and II (Springer, New York, 1971).

[98] M. Kaiser and W. Pesch, Phys. Rev. E **48**, 4510 (1993).

[99] M. Kaiser, W. Pesch, and E. Bodenschatz, Physica D **59**, 320 (1992).

[100] A. P. Kapustin and L. S. Larinova, Krystallografiya **9**, 297 (1964).

[101] E. I. Katz and V. V. Lebedev, Sov. Phys. Crystallogr. **33**, 404 (1988).

[102] H. Kelly, X. L. Wu, and W. I. Goldburg, Phys. Rev. Lett. **74**, 3975 (1995).

[103] D. A. Kessler, J. Koplik, and H. Levine, Adv. Phys. **37**, 255 (1988).

[104] E. L. Koschmieder, Adv. Chem. Phys. **26**, 177 (1974).

[105] E. L. Koschmieder, *Benard Cells and Taylor Vortices* (Cambridge University Press, New York, 1993).

[106] L. Kramer, E. Bodenschatz, W. Pesch, W. Thom, and W. Zimmermann, Liquid Cryst. **5**, 699 (1989).

[107] L. Kramer and A. Buka, Eds., *Pattern Formation in Liquid Crystals* (Springer, New York, 1995).

[108] L. Kramer and P. C. Hohenberg, Physica D **13**, 357 (1984).

[109] L. Kramer and W. Pesch, Annu. Rev. Fluid Mech. **27**, 515 (1995).

[110] I. Kraus, P. Pieranski, and E. Demikhov, J. Phys. A **6** 415 (1994).

[111] T. S. Kuhn, *The structure of Scientific Revolutions*, 2nd ed. (Univ. Chicago Press, Chicago, 1970).

[112] Y. Kuramoto and T. Tsuzuki, Prog. Theo. Phys. **55**, 356 (1976).

[113] J. C. Lacroix, P. Atten, and E. J. Hopfinger, J. Fluid Mech. **69**, 539 (1975).

[114] L. D. Landau and E. M. Lifshitz, *Fluid Mechanics*, 2nd ed. (Pergamon, Oxford, 1987).

[115] L. D. Landau, E. M. Lifshitz, and L. P. Pitaevskii, *Electrodynamics of Continuous Media*, 2nd ed. (Pergamon, Oxford, 1984).

[116] A. J. Leadbetter, J. C. Frost, J. P. Gaughan, G. W. Gray, and A. Mosly, J. de Phys. **40**, 375 (1979).

[117] L. Léger and A. Martinet, J. de Phys. C3 **37**, 89 (1976).

[118] F. M. Leslie, Adv. Liquid Cryst. **4**, 1 (1979).

[119] J. C. Lewis, Phys. Lett. A. **44**, 245 (1973).

[120] J. Liu, and J. P. Gollub, Phys. Fluids **6**, 1702 (1994).

[121] M. Lowe and J. P. Gollub, Phys. Rev. Lett. **55**, 2575 (1985).

[122] W. V. M. Malkus and G. Veronis, J. Fluid Mech. **4**, 225 (1958).

[123] B. Malraison and P. Atten, Phys. Rev. Lett. **49**, 723 (1982).

[124] P. Manneville, *Dissipative Structures and Weak Turbulence* (Academic, New York, 1990).

[125] B. Martinet, P. Haldenwang, G. Labrosse, J. C. Payan, and R. Payan, in *Cellular Structures in Instabilities*, edited by J. E. Wesfreid and S. Zaleski (Springer-Verlag, Berlin, 1984), p.33.

[126] M. R. Maxey and J. J. Riley, Phys. Fluids **26**, 883 (1983).

[127] J. R. Melcher and G. I. Taylor, Annu. Rev. Fluid Mech. 1, 111 (1969).

[128] W. Merzkirch, *Flow Visulization* (Academic, New York, 1974).

[129] J. C. Mitais, P. Haldenwang, and G. Labrosse, in *Proceedings of the VIIIth International Heat Transfer Conference*, edited by C. L. Tien, V. P. Carey, and J. K. Ferell (Harper and Row, New York, 1986).

[130] A. S. Monin and A. M. Yaglom, *Statistical Fluid Mechanics: Mechanics of Turbulence*, vol. I and II (MIT Press, Cambridge, 1975).

[131] S. W. Morris, Ph.D. thesis, University of Toronto, Toronto, Canada (1991).

[132] S. W. Morris, E. Bodenschatz, D. S. Cannell, and G. Ahlers, Phys. Rev. Lett. **71**, 2026 (1993).

[133] S. W. Morris, J. R. de Bruyn, and A. D. May, Phys. Rev. Lett. **65**, 2378 (1990).

[134] S. W. Morris, J. R. de Bruyn, and A. D. May, Phys. Rev. A **44**, 8146 (1991).

[135] J. D. Murray, *Nonlinear Differential Equation Models in Biology* (Clarendon, Oxford, 1977).

[136] K. J. Mysels, K. Shinoda, and S. Frankel, *Soap Films: Study of Their Thinning and a Bibliography* (Pergamon, Oxford, 1959).

[137] S. Nasuno, O. Sasaki, S. Kai, and W. Zimmermann, Phys. Rev. A **46**, 4954 (1992).

[138] A. C. Newell, T. Passot, and J. Lega, Annu. Rev. Fluid Mech. **25**, 399 (1993).

[139] A. C. Newell and J. A. Whitehead, J. Fluid Mech. **38**, 279 (1969).

[140] I. Newton, *Optics*, Book I and II (Smith and Watford, London, 1704).

[141] G. Nicolis and I. Prigogine, *Self-Organization in Nonequilibrium Systems, from Dissipative Structures to Order through Fluctuations* (Wiley, New York, 1977).

[142] G. Nicolis and I. Prigogine, *Exploring Complexity* (Freeman, New York, 1989).

[143] C. Normand, Y. Pomeau, and M. G. Velarde, Rev. Mod. Phys. **49**, 581 (1977).

[144] J. M. Ottino, *The Kinematics of Mixing: Stretching, Chaos, and Transport* (Cambridge University Press, Lodon, 1989).

[145] Q. Ouyang and J. M. Flesselles, Nature, **379**, 143 (1996).

[146] Q. Ouyang and H. L. Swinney, Nature, **352**, 610 (1991).

[147] P. A. Penz and G. W. Ford, Phys. Rev. A **6**, 414 (1972).

[148] A. T. Pérez and A. Castellanos, Phys. Rev. A **40**, 5844 (1989).

[149] A. T. Pérez and A. Castellanos, Phys. Rev. A **44**, 6659 (1991).

[150] P. S. Pershan, *Structure of Liquid Crystal Phases* (World Scientific, Singapore, 1988).

[151] P. Pieranski, L. Beliard, J. Tournellec, X. Leoncini, C. Furtlehner, H. Dumoulin, E. Riou, B. Jouvin, J. Fenerol, P. Palaric, J. Heuving, B. Catier, and I. Kraus, Physica A **194**, 364 (1993).

[152] T. Pitchford, C. C. Huang, R. Pindak, and J. W. Goodby, Phys. Rev. Lett. **57**, 1239 (1986).

[153] Y. Pomeau and P. Manneville, Phys. Lett. **75A**, 296 (1980).

[154] Y. Pomeau and S. Zaleski, J. de Phys. **42** 515 (1981).

[155] E. B. Priestley, P. J. Wojtowicz, and P. Sheng, Eds., *Introduction to Liquid Crystals* (Plenum, New York, 1975).

[156] V. Privman, P. C. Hohenberg, and A. Aharony, in *Phase Transitions and Critical Phenomena*, edited by C. Domb and J. L. Lebowitz (Academic, London, 1991), vol.14.

[157] M. R. E. Proctor and N. O. Weiss, Rep. Prog. Phys. **45**, 1317 (1982).

[158] J. Prost, Adv. Phys. **33**, 1 (1984).

[159] R. Ramshankar, D. Berlin, and J. P. Gollub, Phys. Fluids A **2** 1955 (1990).

[160] R. Ramshankar and J. P. Gollub, Phys. Fluids A **3**, 1344 (1991).

[161] S. Rasenat, E. Braun, and V. Steinberg, Phys. Rev. A **43**, 5728 (1991).

[162] S. Rasenat, V. Steinberg, and I. Rehberg, Phys. Rev. A **42**, 5998 (1990).

[163] Lord Rayleigh, Phil. Mag. **32**, 529 (1916).

[164] H. Riecke and H.G. Paap, Phys. Rev. A **33**, 547 (1986).

[165] C. Rosenblatt and N. M. Amer, Appl. Phys. Lett. **36**, 432 (1980).

[166] J. Ross, S. C. Muller, and C. Vidal, Science **240**, 460 (1988).

[167] D. Ruelle and F. Takens, Comm. Math. Phys. **20**, 167 (1971) .

[168] S. D. Savkar, Phys. Fluids **14**, 2670 (1971).

[169] M. F. Schatz, S. J. Van Hook, W. D. McCormick, J. B. Swift, and H. L. Swinney, Phys. Rev. Lett.,**75**, 1938 (1995).

[170] A. Scheludko, Adv. Colloid Interface Sci. **1**, 391 (1967).

[171] A. Schlüter, D. Lortz, and F. H. Busse, J. Fluid Mech. **23**, 129 (1965).

[172] D. Schwartz, C. M. Knobler, and R. Bruinsma, Phys. Rev. Lett. **73**, 2841 (1994).

[173] L. A. Segel, J. Fluid Mech. **38**, 203 (1969).

[174] M. D. Shattuck, R. P. Behringer, G. A. Johnson, and J. G. Georgiadis, Phys. Rev. Lett. **75**, 1934 (1995).

[175] M. F. Shlesinger, G. M. Zaslavsky, and J. Klafter, Nature **363**, 31 (1993).

[176] E. D. Siggia, Annu. Rev. Fluid Mech. **26**, 137 (1994).

[177] A. Simon, J. Bechhoefer, and A. Libchaber, Phys. Rev. Lett. **61**, 2574 (1988).

[178] E. B. Sirota, P. S. Pershan, L. B. Sorensen, and J. Collett, Phys. Rev. A **36**, 2890 (1987).

[179] L. Sirovich, Ed., *New Perspectives in Turbulence* (Springer-Verlag, New York, 1991).

[180] G. I. Sivashinsky, Annu. Rev. Fluid Mech. **15**, 179 (1983).

[181] T. H. Solomon, E. R. Weeks, and H. L. Swinney, Phys. Rev. Lett. **71**, 3975 (1993).

[182] J. Sommeria and R. Moreau, J. Fluid Mech. **118**, 507 (1982).

[183] S. Sprunt, M. S. Spector, and J. D. Litster, Phys. Rev. A **45**, 7355 (1992).

[184] K. R. Sreenivasan and C. Meneveau, J. Fluid Mech. **173**, 357 (1986).

[185] T. Stoebe, R. Geer, C. C. Huang, and J. W. Goodby, Phys. Rev. Lett. **69**, 2090 (1992).

[186] T. Stoebe, P. Mach, S. Grantz, and C. C. Huang, Phys. Rev. E **53**, 1662 (1996).

[187] J. Stratton, *Electromagnetic Theory* (McGraw-Hill, New York, 1941).

[188] J. B. Swift and P. C. Hohenberg, Phys. Rev. A. **15** 319 (1977).

[189] P. T. Tokumaru and P. E. Dimotakis, Exp. Fluids. **19**, 1 (1995).

[190] M. Trau, S. Sankaran, D. A. Saville, and I. A. Aksay, Nature **374**, 437 (1995).

[191] M. Treiber and L. Kramer. Mol. Cryst. Liq. Cryst. **261**, 311 (1995).

[192] R. Trivedi and W. Kurz, Int. Mate. Rev. **39**, 49 (1994).

[193] L. S. Tuckerman, and D. Barkley, Physica D **46**, 57 (1990).

[194] R. J. Turnbull, Phys. Fluids **11**, 2588 (1968).

[195] R. J. Turnbull, Phys. Fluids **11**, 2597 (1968).

[196] R. J. Turnbull, Phys. Fluids, **12**, 1809 (1969).

[197] R. J. Turnbull and J. R. Melcher, Phys. Fluids **12**, 1160 (1969).

[198] S. M. Troian, X. L. Wu, and S. A. Safran, Phys. Rev. Lett. **62**, 1496 (1989).

[199] W. van Saarloos and P. C. Hohenberg, Physica D **56**, 303 (1992).

[200] H. Wang, Y. Zhu, C. Boyd, W. Luo, A. Cebers, and R. E. Rosensweig, Phys. Rev. Lett. **72**, 1929 (1994).

[201] J. Wesfreid, Y. Pomeau, M. Dubois, C. Normand, and P. Berge, J. de Phys. **39**, 725 (1978).

[202] C. E. Willert and M. Gharib, Exp. Fluids **10**, 181 (1991).

[203] R. Williams, J. Chem. Phys. **39**, 384 (1963).

[204] S. J. Williams and H. Z. Cummins, *Light and Color in Nature and Art* (Wiley, New York, 1983).

[205] D. Wirtz and M. Fermigier, Phys. Rev. Lett. **72**, 2294 (1994).

[206] D. Wirtz and M. Fermigier, Langmuir **11**, 398 (1995).

[207] X. L. Wu, B. Martin, H. Kelly, and W. I. Goldburg, Phys. Rev. Lett. **75**, 236 (1995).

[208] X. Z. Wu, L. Kadanoff, A. Libchaber, and M. Sano, Phys. Rev. Lett. **64**, 2140 (1990).

[209] W. J. Yang, Ed., *Handbook of Flow Visualization* (Hemisphere, New York, 1989).

[210] F. E. Yates, Ed., *Self-Organizing Systems* (Plenum, New York, 1987).

[211] C. S. Yih, *Stratified Flows* (Academic, New York, 1980).

[212] C. Y. Young, R. Pindak, N. A. Clark, and R. B. Meyer, Phys. Rev. Lett. **40**, 773 (1978).

[213] W. Young, A. Pumir, and Y. Pomeau, Phys. Fluids A **1** 462 (1989).

[214] A. N. Zaikin and A. M. Zhabotinskii, Nature **225**, 535 (1970).